VOYAGER OBSERVATIONS OF SATURN'S RINGS

1. THE ECCENTRIC RINGS AT 1.29, 1.45, 1.95, AND 2.27 R_s

2. THE PERIODIC VARIATION OF SPOKES

Thesis by

Carolyn C. Porco

In Partial Fulfillment of the Requirements
for the Degree of
Doctor of Philosophy

California Institute of Technology
Pasadena, California

1983

(Submitted May 16, 1983)

To the members of my family,

who have waited many years for this.

Acknowledgements

In the beginning, there was Peter Goldreich. And He created God. No less a miraculous task, he assisted me in engineering the successful completion of my graduate student career. His remarkable scientific insights have proven essential to the content and quality of this dissertation, and if it meets with the standards of excellence expected of a Caltech graduate, it is due to his criticisms. He has guided my stumbling efforts through the sometimes joyous, sometimes painful events of the past two years and for his patience and his friendship, I sincerely thank him.

I am grateful to the entire faculty of the Planetary Science Department at Caltech for the education they have given me, and for the second, and third, chances to discover that in the end it requires only persistence and faith in oneself to overcome seemingly insurmountable obstacles. I wish in particular to acknowledge Dewey Muhleman who, as my academic adviser, has graciously signed my pre-registration cards for the last 21 quarters.

To Ed Danielson, I owe my life (or so it seems). Recognizing a dejected and hopeless soul, he invited me to participate in what was to be for me the most inspiring event ever — the Voyager encounter with Saturn. Were it not for him and the opportunities he afforded me, none of this would have been possible. He has managed to stomach with courage, and sometimes even a smile, the strident impetuousness of a person with a chipped shoulder and his fortitude, enthusiasm, and generosity over the past three years are greatly appreciated. (I also credit him with irrevocably altering my views of matrices and, possibly even men.)

The motivation for studying the eccentric features in Saturn's rings I owe to Philip Nicholson who came to me seeking assistance in analyzing Voyager pictures and then, without complaint, sat back and watched me commandeer the entire project. The work presented herein has benefitted from his suggestions, and I thank him for his thoughtfulness and his patient and lucid explanations in matters ranging from data analysis to celestial mechanics.

I am unspeakably grateful to Brad Smith and the entire Voyager Imaging team for permitting those precious bits of data, which flew screaming across the solar system, to land (luckily for me) in the hands of an unproven neophyte. I also thank Jay Holberg of the UVS experiment, Lonne Lane and Amarra Graps of the PPS experiment, and Len Tyler and Howard Zebker of the RSS experiment for generously offering their data, without which the study of Saturn's eccentric rings would have been impossibly frustrating. I am equally indebted to all those persons in the many thankless jobs at JPL (among them Joel Mosher, Gary Yagi, Charlie Avis, Steve Synnott, and others) who never seemed to grow tired of my incessant proddings for information.

To Bob Deverill of the WFPC facility at Caltech, the mastermind of computer programming, I extend heart-felt thanks for many lessons in Fortran, flaky tape drives, virtual memories and general computer vagaries. May you always find some huge dark hole to stare into. I am grateful to James Westphal for allowing me to use his wonderful VAX computer on which 100% of the analysis presented here was done. And I thank Vance Haemmerle for being, though a Caltech undergraduate, so lovable and enthusiastic; and for saving me precious moments by reading at my request the entire text of Bracewell's *The Fourier Transform and Its Application* and happily regurgitating it back to me. Surely, Vance knows more about Fourier transforms now than Fourier himself.

A very special thanks goes to David Jewitt: for the inspiration, for his humour and friendship, for many interesting and eye-opening conversations on the values of a Socialist society, but most of all, for his continual encouragement of a diffident, working-class female. And I thank numerous graduate students with whom I have crossed paths in my years at Caltech for many enjoyable hours spent in relentless laughter and commiseration.

And thanks be to the unsung heroines of the first floor of South Mudd — Kay Campbell, Donna Lathrop, Bernadine Burgess, and Brenda Smith —for holding the whole damned place together. Without them, there would be no meetings, no proposals, no papers, no seminars, no classes, no graduate students, and certainly no faculty! In particular I single out Donna for her heroic efforts in seeing that this dissertation be completed on time.

To my 'extended family' I offer the greatest thanks of all . . . for their encouragement, and the love and laughter shared: Madeline, Michael, Sally, Bill, Robin, Dennis, Lizzie, Briant, Ron, Chuck, Dave, Jude, Leslie, Peter, Holly, BAZ, the Beans, the Cordovas, the Malones, and the Meertens.

And lastly . . . humbly . . . I acknowledge the beauty and the splendor of Saturn's rings.

Abstract

Part 1:

Five major eccentric features in the rings of Saturn are studied. These are the outer A and B ring edges at 1.95 and 2.27 R_s and three narrow ringlets at 1.29, 1.45, and 1.95 R_s. Data acquired by four Voyager experiments — Imaging Science (ISS), Radio Science (RSS), Ultraviolet Spectrometer (UVS), and Photopolarimeter (PPS) — were used in this investigation.

The shapes and kinematics of the A and B ring outer edges are determined by their proximity to strong low-order Lindblad resonances. The data for the A ring edge are consistent with a 7-lobed distortion rotating with the mass-weighted mean angular velocity of the co-orbital satellite system. The B ring edge has a double-lobed figure which rotates with the mean motion of Mimas.

The Saturnian ringlets are narrow (mean widths vary from ~ 10-60 km) and have eccentricities of order 10^{-4}. All have sharp edges, normal optical depths $\tau \sim$ 1-2, and are embedded in essentially empty gaps ($\tau <$ 0.05). The Titan ring at 1.29 R_s and the Huygens ring at 1.45 R_s exhibit positive linear width-radius relations; the Maxwell ring at 1.95 R_s does not. The kinematics of the Huygens ring are determined solely by Saturn's non-spherical gravity field. The kinematics of the Titan ring are apparently completely determined by its interaction with Titan. At present, the most plausible model for the Maxwell ring involves the superposition of two components: one which is freely precessing and the other which is forced by Mimas and the elliptical B ring. Masses, mean surface mass densities, and specific opacities have been calculated for the Titan and Huygens rings.

Part 2:

The discovery of a periodic variation in spoke activity in Saturn's rings from the analysis of Voyager images is reported. A Fourier power spectrum was computed using a data set generated by quantifying spoke activity observed on the morning (western) half of the rings in Voyager images spanning ∼ 12 Saturn rotations and in Voyager 2 images spanning ∼ 90 Saturn rotations. The period from Voyager 1 data is 621 ± 22 min; from Voyager 2, 640.6 ± 3.5 min. The latter result suggests that the fundamental modulation in spoke activity is due to the rotation of Saturn's magnetic field, the period of which is 639.4 min. Maximum spoke activity observed anywhere on the rings is most likely to be associated with the region of the magnetic field responsible for the most intense emission of the Saturn Kilometric Radiation (SKR). Passage of this region through Saturn's shadow may play a significant role in the creation and/or rejuvenation of spokes.

Table of Contents

Acknowledgements iii

Abstract vii

List of Figures xii

List of Tables xiv

PART 1. THE ECCENTRIC RINGS AT 1.29, 1.45, 1.95, AND 2.27 R_s 1

Preface 2

Chapter I. Voyager Observations of Eccentric Rings 4

1. Data Description 4

   1a. ISS Imaging Data 4
   1b. UVS Occultation Data 5
   1c. PPS Occultation Data 5
   1d. RSS Occultation Data 6

2. Data Reduction 7

References 12

Chapter II. Non-Axisymmetric Ring Edges 13

1. Introduction 13

2. Dynamics 14

3. Ring Edge Models 16

   3a. A Ring Edge 17
   3b. B Ring Edge 28

4. Discussion 30

5. Conclusions 35

References 38

Chapter III. Narrow Eccentric Rings 39

1. Introduction 39

2. Ring Models 40

- 2a. 1.29 R_s 44
- 2b. 1.45 R_s 45
- 2c. 1.95 R_s 50

3. Width-Radius Relations 57

4. Discussion 64

5. Conclusions 74

References 77

PART 2. THE PERIODIC VARIATION OF SPOKES 78

Preface 79

Chapter IV. A Summary of Spoke Observations 80

References 88

Chapter V. The Periodic Variation of Spokes in Saturn's Rings 89

Abstract 90

1. Introduction 90

2. Data Description 92

- 1. Voyager 1 inbound movie frames 92
- 2. Voyager 1 intermediate frames 93
- 3. Voyager 2 frames 93

3. Data Reduction and Analysis 94

- a. Intermediate Data Set 94
- b. Association of Magnetic Longitude with Spoke Activity 100
- c. Inbound Movie 103

4. Discussion 109

5. Conclusions 114

References 116

Chapter VI. Spoke Variability in Voyager 2 Images 117

1. Abstract 117

2. Fourier Analysis 117

3. Correlation of Activity with the Magnetic Field 119

4. Discussion 127

5. Conclusions 130

References 140

List of Figures

Chapter II.

1. χ^2/DOF vs. Ω_P for A ring edge 24

2. Radius-longitude model and data, A ring edge 27

3. Radius-longitude model and data, B ring edge 32

Chapter III.

1. Radius-longitude model and data, Titan ringlet 47

2. Radius-longitude model and data, Huygens ringlet 49

3. Radius-longitude model and data, Maxwell ringlet 53

4. Width-radius relation, Titan ringlet 59

5. Width-radius relation, Huygens ringlet 61

6. Width-radius relation, Maxwell ringlet 66

Chapter IV.

1. Spoke angular velocity vs. radial distance 85

Chapter V.

1. Four spoke activity categories 96

2. Fourier power spectrum ~ 12 Saturn rotations 99

3. Frequency distributions 102

4. Frequency distribution, sum of Voyager 1 and 2 results 105

5. Spoke activity vs. time, Voyager 1 inbound movie 108

6. SKR-active sector/Sun geometry 112

Chapter VI.

1. Fourier power spectrum, ~ 90 Saturn rotations 121

2. Frequency distributions, Voyager 1 and 2 results 124

3. Frequency distribution for evening-ansa activity 126

Plates

1. B ring edge/Cassini division 142

2. Huygens ringlet 144

3. Titan ringlet 146

4. A spoke observed at high phase angle 148

List of Tables

Chapter II.

IIa. A Ring Edge Data Table 18

IIb. B Ring Edge Data Table 19

IIc. Ω_P and $\beta(k)$ for the 7:6 Co-orbital Resonance Components 21

Chapter III.

IIIa. Titan Ringlet Data Table 41

IIIb. Huygens Ringlet Data Table 42

IIIc. Maxwell Ringlet Data Table 43

IIId. Model Parameters, Gap Dimensions, M_r, $\sum$, and κ for Titan and Huygens Ringlets 63

Chapter VI.

I. Voyager 2 Images 132

PART 1

THE ECCENTRIC RINGS AT 1.29, 1.45, 1.95, and 2.27 R_s

Preface

The recent interest in eccentric rings began shortly after the discovery of the Uranian rings in 1977 by Elliot et al. (1977). While observing a stellar occultation by Uranus, Elliot and his coworkers found unmistakable attenuations in the signal received from the star prior to and after the planetary occultation. These were attributed to 5 narrow rings encircling Uranus. Four more rings were subsequently discovered (Elliot et al. 1978). With the accumulation of occultation data sampling different azimuths on the rings, the shapes and kinematics of these features were determined: 6 of the 9 rings are eccentric Keplerian ellipses (Elliot et al. 1981; Nicholson et al. 1981); 6 are inclined to the Uranian equatorial plane (French et al. 1982). The apses and nodes precess under the influence of the multipole moments of Uranus.

In 1980 and 1981 the two Voyager spacecraft flew by Saturn and found narrow eccentric ringlets at 1.29, 1.45 and 1.95 R_s and the F ring at 2.32 R_s (Smith et al. 1981, 1982). The outer edge of the B ring near the 2:1 resonance with the Saturnian satellite Mimas was also found to be non-circular. As a result of the present work, the outer edge of the A ring, which lies near the 7:6 resonance with the co-orbital satellites, is added to this list of non-axisymmetric ring features. The study of the shapes and kinematics of these features, with the exception of the F ring, is the subject of the first half of this dissertation.

The same data sets were used to study all features and were analyzed in the same manner. To avoid repetition, the data and the reduction techniques are described once in Chapter I. The model results and interpretations are presented in succeeding chapters. Chapter II is devoted to the analysis of the A and B ring edges. A brief outline of the dynamics affecting these features is given in this chapter. The results of the study of the narrow Saturnian rings are given in chapter III.

The investigations presented here are predominantly the work of the author. However, others have provided data, assistance in data reduction, important calculations, and/or valuable suggestions regarding interpretation of the results. Listed in alphabetical order, they are: N. Borderies, G.E. Danielson, P. Goldreich, J.B. Holberg, A.L. Lane, P.D. Nicholson, and H.A. Zebker.

References

Elliot, J.L., Dunham, E., and Mink, D. (1977). *Nature* **267**, 328.

Elliot, J.L., Dunham, E., Wasserman, L.H., Millis, R.L., and Churms, J. (1978). *Astron. J.* **83**, 980.

Elliot, J.L., French, R.G., Frogel, J.A., Elias, J.H., Mink, D.J., and Liller, W. (1981). *Astron. J.* **86**, 444.

French, R.G., Elliot, J.L., and Allen, D.A. (1982). *Nature* **298**, 827.

Nicholson, P.D., Matthews, K., and Goldreich, P. (1981). *Astron. J.* **86**, 596.

Smith, B.A., et al. (1981). *Science* **212**, 163.

Smith, B.A., et al. (1982). *Science* **215**, 504.

Chapter I. Voyager Observations of Eccentric Rings

1. Data Description

The data sets used in this study were obtained from four Voyager experiments:

1a. ISS Imaging Data. These are two-dimensional images which were acquired with both narrow and wide angle cameras of the ISS Voyager 1 and Voyager 2 experiments. The ones used for this study were taken predominantly through the clear filter (λ_{eff} ~ 4970 Å) and cover a range of ~5 to ~60 km/pixel resolution. All frames were corrected for distortion due to the camera electronics. Voyager 1 observations occurred within ~1 day of Voyager 1 closest approach; Voyager 2 observations, within ~5 days of Voyager 2 closest approach. The Voyager encounters were separated by 286 days.

The Voyager frames taken in diffuse transmission from below the ring plane were not used in this analysis. Under this particular lighting condition, brightness is not a monotonically increasing function of optical depth. A ringlet with a very optically thick core and diffusely transmitting wings would appear indistinguishable from two ringlets separated by a narrow empty gap. Positional measurements are difficult in this case as they depend upon model profiles for the ring transmission and reflection as a function of optical depth. Images taken in reflected light (see Plates 1-3) or direct transmission (against the disk of the planet) are more easily interpreted. Therefore, only these latter types of data were used. They are identified by FDS (Flight Data Subsystem) number in the data Tables IIa,b and IIIa,b,c for each feature. Columns 1-3 list for each frame the FDS number, the spacecraft, and the camera and filter through which the image was acquired.

1b. UVS Occultation Data. These data were acquired by the Voyager ultraviolet spectrometers observing stellar occultations by the rings of Saturn (Sandel et al. 1982; Holberg et al. 1982). The first observation was an exit occultation of the star *ι* Her during Voyager 1 encounter; the second and third occurred during the Voyager 2 encounter when an entrance and an exit occultation of the star *δ* Sco were observed. The UVS instrument obtained a spectrum from 912 to 1700 Å every 0.32 sec during each occultation. For the *ι* Her occultation, this resulted in a resolution of ~ 7 km; for the *δ* Sco occultations, the resolution was ~ 4 km. These data were summed over all wavelengths and corrected for instrumental effects to yield a single intensity at an effective wavelength of 1125 Å. Normal optical depths vs. radius along the occultation path were derived from the ratio of the attenuated to the unattenuated signal and the angle of the line of sight to the ring plane, ~ 28°.7 for the *δ* Sco occultations and ~ 41°.2 for the *ι* Her occultation. The *δ* Sco exit occultation scanned the entire ring system. The other two scanned only the inner C ring; both sampled the region around 1.29 R_s. Consequently, there are three UVS occultation observations of the 1.29 R_s ringlet and only one of each of the other ring features studied here.

1c. PPS Occultation Data. The Voyager 2 exit occultation of *δ* Sco was also observed by the Photopolarimeter experiment which consisted of a photometer and a narrow band filter of central wavelength λ = 2640 Å (Lane et al. 1982). The time constant of this instrument was 10 msec yielding a resolution in the ring plane of ~ 100 m. Measurements were made on plots in which the resolution was degraded to ~ 0.5 – ~ 3.0 km to improve signal to noise.

The UVS and PPS occultation experiments occurred at the same time and with the same viewing geometry. When compared against each other, the positions of features seen by both instruments are found to be identical to within measurement errors. The differences which do exist between these two data sets, such as resolvable structure within features, are inconsequential for the present analysis which is concerned only with positional measurements. Therefore, the two data sets are treated here as one. Error estimates were made on the UVS scans. The appropriate information for the UVS data is given in the data tables in chapters II and III.

1d. RSS Occultation Data. Five hours after closest approach to Saturn, the Voyager 1 spacecraft emerged from behind Saturn as seen from the earth. For 17 minutes its transmitted signals at λ3.6 and λ13 cm were occulted by the rings. The oblique optical depth at every point along the occultation path was measured. The angle of the line of sight to the ring plane was 5°.9 (Tyler et al. 1983).

Due to diffraction effects, initial results from this experiment are limited to a resolution the size of a Fresnel zone projected onto the ring plane. Signal processing can improve the resolution by correcting for diffraction. This was done for the λ3.6 cm signal in the vicinity of 1.45 R_s yielding a resolution of ~ 1 km. RSS data for the other eccentric features have not yet been processed in this way; the resolution for these data is nominally ~ 5 km for the 1.29 R_s ring and ~ 15 km in the Cassini division. In the presence of sharp edges, however, higher resolutions may be achieved by measuring the location of the -6 dB intensity level. In theory this gives the exact location of an infinitely sharp edge from data not corrected for diffraction effects. The data tables include the RSS datum and the information relevant to this observation.

Both the UVS and RSS occultation experiments had the capability of determining an absolute distance scale for the rings. The original disagreement in this scale between the two data sets was attributed to an uncertainty in the position of Saturn's rotational pole. The currently adopted pole is obtained by simultaneously fitting both data sets and solving for the pole vector (Simpson et al. 1982). The resulting (systematic) uncertainty in the absolute radius scale is $\sim \pm 6$ km.

Throughout Chapters II and III, the RSS and UVS data points are indicated in the figures displaying the model results.

2. Data Reduction

Measurements were made in all data sets to locate the edges of rings between two fiducial features. Such measurements in the occultation data, which are already in the format of intensity vs. radius in the ring plane, were straightforward. In the case of the ISS data, scans of brightness (DN value) vs. position were made perpendicular to the ring features in the image, a direction which is generally not radial on the ring plane and is almost always diagonal to the pixel grid. Brightness values were interpolated between pixels using the sampling theorem, a result of which is that the intermediate points of a band-limited function can be fully recovered from evenly sampled data by convolution with $\sin\pi x/\pi x$ (Bracewell 1978). Each scan was an average taken over at least 3 pixels to increase the signal to noise ratio; in general two or more such scans were made per image and averaged. A half-dozen sharp-edged 'test' features common to all frames were chosen and the location of the half-power point (or, for RSS data, the -6 dB point) of each edge was measured. These measurements served the dual purpose of checking the circularity of each test feature against the others and of providing a measure of the error associated with the location of the eccentric feature in each frame. This was accomplished by the following procedure.

First, for the ISS data it was necessary to determine the resolution in the ring plane. In general this is different from the resolution in the image plane. The occultation scans are among the highest resolution ring data obtained by Voyager and have been absolutely calibrated in radial distance. The ring plane resolution was deduced by measuring the absolute radial distance in kilometers between two of the test features in the occultation scans and the difference in the number of resolution elements (pixels) between the same two features in the ISS data. The ratio is the number of kilometers per pixel in the ring plane for that frame.

The check for circularity was done by iteration. (For brevity, in what follows both ISS images and occultation data will be referred to as scans). Two 'trial' test features or benchmarks were chosen; the positions of all other test features were scaled relative to these for each scan. The averaged scaled radius of a single feature, $\bar{r}_x$, was obtained by weighting the scaled radius by the inverse square of the ring plane resolution for that scan and averaging these weighted values over all scans: i.e.,

$$\bar{r}_x = \frac{\sum_{i=1}^{N} r_{x,i}/R_i^2}{\sum_{i=1}^{N} 1/R_i^2} ,$$

where N = number of scans, R_i = ring plane resolution for scan i, and $r_{x,i}$ = scaled radius of feature x in scan i.

The resolution-weighted standard deviation of each feature, σ_x, was also calculated:

$$\sigma_x^2 = \frac{\sum_{i=1}^{N} \left[r_{x,i} - \bar{r}_x\right]^2 / R_i^2}{\sum_{i=1}^{N} 1/R_i^2} \quad .$$

Although it is reasonable to suspect some degree of systematic error in positional measurements for any data set considered here (for example, incomplete correction for camera electronics distortion in the ISS data), the largest errors are most likely to be random, Gaussian measurement errors. This type of error will be positively correlated with the size of a resolution element. Therefore, weighting a measurement by the inverse square of the resolution in the ring plane is equivalent to weighting by the inverse square of the standard deviation of that measurement, a common procedure in statistics when data are not of uniform precision.

The σ_x is a measure of the fluctuations in the scaled radius of a feature due to measurement errors, systematic differences between scans, non-circularity of the 'trial' benchmarks and non-circularity of the feature itself. The first two effects are difficult to avoid. The separation of the latter two was accomplished by performing the procedure just described on several sets of 'trial' benchmarks and comparing the resulting σ_x's from each trial. All test features chosen had standard deviations significantly less (by factors of 3 or more) than that of the eccentric feature, and when used as benchmarks, never caused the standard deviations of the other test features to become unreasonably large. From this array of circular features, two were chosen as the fiducial features from which the final scaled radii were obtained.

The value of σ_x for the eccentric feature was dominated by its non-circularity and could not be used as a measurement error. Instead, for a given scan i, the rms deviation, σ_i, of the scaled radii of the remaining test features from their weighted-average values was computed:

$$\sigma_i^2 = \frac{\sum_{x=1}^{M} \left(r_{x,i} - \bar{r}_x \right)^2}{M} \quad ,$$

where M = the number of features. This number is a measure of the average uncertainty in a scan due to both Gaussian and systematic errors and is the uncertainty assigned to the measurement of the eccentric feature. When converted back to resolution elements, the range in the σ_i's is ~ 0.4-1.0. These are values one might reasonably expect from Gaussian errors alone and indicate that any systematic problems in these measurements play only a minor role.

Columns 4-6 of the data tables list the ring plane resolution, the scaled radius, and the measured scaled uncertainty for each scan in all of the data sets. The numbers in column 5 were used as radii in the model fitting. In the final step of the data reduction, the solutions for the scaled radii were converted back to absolute radii by using the radius scale provided by Holberg et al. (1982) and Simpson et al. (1982). The data tables include the absolute radial distance, Δ, between the two fiducial features and the absolute radius of the inner one, f_1. The uncertainties assigned to these numbers were obtained from the PPS occultation data.

Longitudes were measured clockwise (opposite to rotation) in Saturn's ring plane relative to an inertial system defined by the position of the sub-solar point on the rings at the time of Voyager 1 closest approach (1980 November 12, 23h 46m UTC — spacecraft event time). This longitude system will hereafter be referred to as the Solar Longitude System, or SOL.

The SOL longitude of each occultation observation at radius r on the ring plane was computed using the spacecraft navigation information, the photon penetration event time at radius r, the direction to the sun, and a) the position of the occulted star in the case of the UVS/PPS experiment, or b) the direction to earth in the case of the RSS experiment. These longitudes are accurate to $< 0^\circ.5$.

For the ISS data the longitudes were obtained in one of two ways. In low resolution frames in which measurements were made on the left-hand (right-hand) ansa as seen from the spacecraft, 90° (270°) was added to the sub-spacecraft SOL longitude; correction was made for the non-infinite radial distance of the spacecraft from Saturn. For high resolution frames, the longitude was obtained from information regarding the direction of the optic axis. The longitudes in both cases are probably uncertain to ± 3°. Columns 7-8 of the data tables list for each observation the time from the SOL system epoch and the SOL longitude in the ring plane.

References

Bracewell, R.N. (1978). *The Fourier Transform and Its Application*, McGraw-Hill, New York.

Holberg, J.B., Forrester, W.T., and Lissauer, J.J. (1982). *Nature* **297**, 115.

Lane, A.L., et al. (1982). *Science* **215**, 537.

Sandel, B.R., et al. (1982). *Science* **215**, 548.

Simpson, R.A., Tyler, G.L., and Holberg, J.B. (1982). *BAAS* **14**, 731.

Tyler, G.L., Marouf, E.A., Simpson, R.A., Zebker, H.A., and Eshleman, V.R. (1983). *Icarus*, in press.

Chapter II. Non-Axisymmetric Ring Edges

1. Introduction

The two strongest resonances in Saturn's rings are the Mimas 2:1 Lindblad resonance at 1.948 R_s and the 7:6 co-orbital Lindblad resonance at 2.267 R_s. These resonances fall close to two major features in the ring system, the outer B and A ring edges. Cursory examination revealed the B ring edge to be a Saturn-centered ellipse rotating with a speed equal to the mean motion of Mimas; the line joining the radial minima was observed to point approximately to Mimas (Smith et al. 1982). These results suggested distortion of the particle orbits by the action of the satellite. Until now, no analysis has been made of the shape of the outer A ring edge.

In this chapter the results obtained from a detailed analysis of Voyager data to study the A and B ring edges are discussed. A brief description of the dynamics of resonances is given for background and to provide justification for the models chosen in this analysis. The gross characteristics of the B ring edge previously reported by Smith et al. (1982) are confirmed, though a Saturn-centered co-planar ellipse does not appear to provide a completely satisfactory fit to the data. An upper limit to the angle between the direction to Mimas and the minor axis of the ellipse is obtained. This allows an estimate to be made of the viscosity and vertical ring thickness in the unperturbed region of the B ring. The data for the A ring edge are consistent with a seven-lobed distortion rotating with the mean angular frequency of the co-orbital system. However, the central and sideband 7:6 resonances produced by the co-orbitals at the A ring edge are closely-spaced and make a complete interpretation of the results reported here impossible at this time.

2. Dynamics

The perturbing potential of a satellite orbiting in the plane of the rings may be decomposed into a Fourier series. The frequency of the mth component at a point fixed in inertial space is equal to $m\Omega_P$, where Ω_P is the pattern speed. The forcing frequency felt by a particle moving with orbital angular velocity Ω is $m(\Omega - \Omega_P)$. Lindblad resonances are located where the forcing frequency is equal to the natural radial frequency of the particle. In an inverse-square law force field, the particle's radial and angular frequencies are equal; the orbit is closed. In the gravitational field of an oblate planet, the apsidal line of the particle's orbit precesses at a rate $\dot{\varpi}$. The radial or 'epicyclic' frequency $\kappa = \Omega - \dot{\varpi}$. The condition satisfied at an inner Lindblad resonance, the most important kind in Saturn's rings, is:

$$m\Omega_P - (m-1)\Omega = \dot{\varpi} \quad . \tag{1}$$

In a reference frame rotating with the pattern speed, the exciting potential is a time-independent function of azimuth and radius. At the resonance location in this frame, an unperturbed eccentric orbit is closed (i.e., periodic) and traces out an m-lobed pattern. In the inertial frame, a streamline composed of many resonant particles at different phases in their orbits is also an m-lobed pattern which rotates with a pattern speed Ω_P. In general $\dot{\varpi} << \Omega$, and condition (1) yields

$$\Omega \approx m\Omega_P/(m-1) \quad ,$$

for the orbital angular velocity at resonance.

The dominant terms in the expansion of the potential are those of lowest order in the satellite's eccentricity; for $e_{sat} = 0$, there is a unique pattern speed

$\Omega_P = \Omega_s$, the satellite's mean motion.

The amplitude of the disturbance can be estimated with the aid of (1) where $\dot{\tilde{\omega}}$ is the combined precession from secular and resonant perturbations.

The dominant secular effect is due to the multipole moments of Saturn's gravity field:

$$\dot{\tilde{\omega}}_P(a) = \left[\frac{GM_p}{a^3}\right]^{1/2}\left\{\frac{3}{2}J_2\left[\frac{R_P}{a}\right]^2 - \frac{15}{4}J_4\left[\frac{R_p}{a}\right]^4 + \frac{105}{16}J_6\left[\frac{R_P}{a}\right]^6 - \cdots\right\} , \tag{2}$$

where J_2, J_4, J_6, etc. are the dimensionless coefficients in the spherical harmonic expansion of the gravity field. Using the coefficients for Saturn (Null et al. 1981), $\dot{\tilde{\omega}}_p = 2^\circ.95$ day^{-1} at the A ring edge and $5^\circ.01$ day^{-1} at the B ring edge. The secular perturbations due to the Saturnian satellites and the ring system are negligible, of order 10^{-3}-10^{-5} °/day.

The dominant resonant perturbation of the precession rate is caused by the satellite. (We consider here a test particle orbit and neglect the interactions with other resonant particles which can be significant). For an orbit of zero inclination and low eccentricity, this perturbation is given by Lagrange's equation:

$$\dot{\tilde{\omega}}_{sat} = \frac{1}{\Omega\, a^2 e}\frac{\partial R}{\partial e} , \tag{3}$$

with

$$R = \frac{-GM_s e}{2a_s}\left\{2jb_{1/2}^{(j)}(\alpha) + \frac{\alpha\, db_{1/2}^{(j)}}{d\alpha}\right\}\cdot\cos\Phi , \tag{4}$$

where R is the disturbing function of the satellite; $\alpha = a/a_s$ (for an external satellite), e is the eccentricity of the ring particle, Φ is the resonance variable, and $\{b_{1/2}^{(j)}\}$ are the Laplace coefficients which arise in the expansion of the potential between two bodies in orbit around a primary for an $m = j$ disturbance. (For $m = 1$, $b_{1/2}^{(j)} \rightarrow b_{1/2}^{(j)} - \alpha$). For conjunctions at periapse (apoapse), $\Phi = 0$ (π). The precession required to keep orbits periodic in the satellite's frame at semimajor axis a, can be calculated from a Taylor expansion of (1) around the resonance position:

$$\dot{\tilde{\omega}}(a) = -\frac{d\Omega}{da}\Big|_{a_{res}}(a - a_{res}) \ , \quad m \neq 1 \ ;$$

$$\dot{\tilde{\omega}}(a) = -\frac{d\tilde{\omega}_p}{da}\Big|_{a_{res}}(a - a_{res}) \ , \quad m = 1 \ , \tag{5}$$

Simultaneous solution of (3) and (5) yields the forced eccentricity of the periodic orbit:

$$e_{per} \propto \frac{-M_s}{M_p} \frac{\cos\Phi}{(a - a_{res})} \ . \tag{6}$$

For $(a - a_{res}) > 0$ $[< 0]$, the radial maximum [minimum] is aligned with the satellite's angular position. An estimate of the maximum amplitude of the disturbance, ae, expected just from satellite forcing at a ring edge can be obtained from (6) and the condition for intersecting streamlines, $a\,\delta e/\delta a = 1$.

3. Ring Edge Models

The eccentricities of the particle orbits at the A and B ring edges are presumably forced in the manner described above. Therefore, the measurements of the edges of the A and B rings were fitted in the least-squares sense with models describing uniformly precessing m-lobed patterns:

$$r = a\left\{1 - e\cos m\left[\vartheta - \tilde{\omega}_0 + \Omega_P(t - t_0)\right]\right\} \ , \tag{7}$$

where Ω_P is the pattern speed, m is the resonance label, a is the semimajor axis, e is the eccentricity of the periodic orbits, $\tilde{\omega}_0$ is the SOL longitude of periapse at $t = t_0$, and r and ϑ are the observed scaled radius and SOL longitude of the measurement at the time of observation, t. The scaled radii were weighted by the inverse square of their errors. Four parameters, a, e, $\tilde{\omega}_0$, and Ω_P, were adjusted to yield the least-squares solution of lowest residuals. The two sampling epochs at Voyager 1 and Voyager 2 encounters were separated by 286 days; the lengths of these intervals were ~ 1 day and ~ 5 days, respectively. In practice many solutions for Ω_P are satisfactory, each corresponding to an additional (360°/m) rotation of the m-lobed pattern between the sampling epochs. The final solution chosen was the one giving Ω_P closest to the expected pattern speed.

Note: The errors quoted for the values of e, $\tilde{\omega}_0$, and Ω_P are formal 1σ errors for these parameters. No attempt has been made to correct for the correlations among them. However, the error quoted for the semimajor axis, a, after conversion to absolute units, is the sum of the formal 1σ error plus the error in assignment of the absolute distance scale of ± 6 km.

3a. A Ring Edge

The proximity of the A ring edge to the central 7:6 resonance with the co-orbital satellites motivated a search for a 7-lobed pattern in the shape of the A ring edge. The orbits of the co-orbitals have been described by Yoder et al. (1983). At the present time these orbits are characterized by a large relative amplitude of libration; the angle of minimum separation, $\varphi_{\mathrm{min}} \sim 6°$. After closest approach the satellites' angular frequencies change in proportion to the inverse ratio of their masses. The difference in the mean motions, $0°.254\ \mathrm{day}^{-1}$,. implies a reversal period of ~ 3.9 years. Observations of the co-orbitals made on

Table IIa. A Ring Edge

Experiment* ID	Voyager S/C	Camera/ Filter	Ring Plane Resolution (km)	Radius (scaled)	Error (scaled)	Time from Epoch (days)	SOL Longitude (deg)
RSS	1	-	3	1.094	.001	0.158	140.5
43968.29	2	NA/clear	17	1.090	.004	284.914	60
43968.45	2	NA/clear	14	1.090	.003	284.922	263
43970.32	2	NA/clear	13	1.089	.003	284.982	250
43978.01	2	NA/clear	13	1.088	.003	285.231	59
43978.05	2	NA/clear	10	1.091	.002	285.233	55
43978.17	2	NA/clear	13	1.090	.003	285.240	269
43990.14	2	NA/clear	8	1.093	.002	285.639	244
44007.56	2	WA/clear	9	1.092	.003	286.228	145
UVS/PPS	2	-	4	1.090	.001	286.083	190.1

$\Delta = 2925 \pm 1$ km

$f_1 = 133588 \pm 1$ km

* FDS #'s for ISS data

Table IIb. B Ring Edge

Experiment* ID	Voyager S/C	Camera/ Filter	Ring Plane Resolution (km)	Radius (scaled)	Error (scaled)	Time from Epoch (days)	SOL Longitude (deg)
RSS	1	-	5	.464	.002	0.156	135.7
34956.55	1	WA/clear	55	.465	.005	0.430	62
34962.52	1	WA/clear	62	.487	.007	0.628	221
43864.48	2	NA/clear	53	.481	.005	281.458	71
43865.00	2	NA/clear	48	.495	.006	281.464	254
43912.04	2	NA/clear	36	.461	.003	283.033	69
43968.33	2	NA/clear	16	.467	.002	284.916	60
43968.41	2	NA/clear	45	.485	.006	284.920	354
43989.46	2	NA/clear	7	.471	.002	285.623	48
43993.06	2	NA/clear	6	.492	.002	285.734	243
43998.25	2	WA/clear	27	.483	.004	285.910	209
43999.40	2	WA/clear	20	.472	.002	285.953	223
UVS/PPS	2	-	4	.458	.001	286.060	192.6

$\Delta = 4719 \pm 5$ km

$f_1 = 115336 \pm 4$ km

* FDS #'s for ISS data

either side of reversal, i.e., as they approach and then recede from one another, yield a measure of the satellite mass ratio. Unfortunately, both Voyager encounters occurred during satellite approach. (Orbit reversal occurred in January, 1982, approximately 5 months after Voyager 2 encounter.) However, an estimate of the mass ratio, as well as an accurate measure of the average mean angular frequency of the co-orbital system, $\overline{\Omega}$, was obtained from the combination of Voyager 1 data and ground-based observations made in 1966 during satellite separation by Larson et al. (1981). From this analysis, Yoder et al. (1983) find $M = M_1/M_3 = 3.3 \pm 1$; $\overline{\Omega} = 518^\circ.291 \pm 0^\circ.002$ day^{-1}.

The resonant perturbations at the A ring edge are complicated by the presence of many potential components with slightly different pattern speeds. These frequency splittings arise from the libration of the two satellites; the pattern speeds differ from $\overline{\Omega}$ by $(k/2)(\Delta\Omega/7)$, where $\Delta\Omega = 0^\circ.254$ day^{-1} and k is an integer. For small libration angles (large $\varphi_{\min}$), the principal resonance at $k = 0$ is strongest. This is not the case for the present co-orbital configuration for which $\varphi_{\min} \sim 6^\circ$. The pattern speeds and relative absolute magnitudes, $\beta(k)$ of these potential components are given in Table IIc for $0 \le k \le 5$, $\varphi_{\min} = 6^\circ$, and $M = 2.3$, 3.3, and 4.3 to accommodate the uncertainty of ± 1 in the mass ratio.

Measurements of the errors in the A ring edge radii were made difficult by the lack of reliable benchmarks: many of the resonance-related features in this region change contrast with changing phase angle, rendering them useless as test features. Consequently, only two (or fewer) features in each scan were used to compute the error in the scaled radius. For two frames (FDS #'s 43968.29 and 43978.01), no measure of the error could be made at all. In these instances, the error was estimated to be ± 0.7 resolution elements, the average obtained for the entire A ring data set.

Table IIc

k	$\Omega_p(k,3.3)$	$\beta(k,2.3)$	$\beta(k,3.3)$	$\beta(k,4.3)$
0	518.291 day^{-1}	0.00	0.38	0.37
1	518.309	0.30	0.07	0.40
2	518.327	0.02	0.65	1.00
3	518.345	0.65	1.00	0.88
4	518.364	1.00	0.68	0.31
5	518.382	0.71	0.10	0.12

The two fiducial features chosen were the midpoints of the Encke and Keeler gaps. It is known that the edges of the Encke gap exhibit maximum peak-to-peak variations of 4 km, with wavelengths of ~ 1800 km or 0°.7 in azimuth (Cuzzi and Scargle 1983). However, problems due to this variation are believed to be small for several reasons. First, the waves seen in the Encke division edges are not continuous over $> 30^\circ$ in azimuth. Second, in each image two or more scans perpendicular to the ring features were made at azimuths differing in general by $\gtrsim 3^\circ$ in wide-angle frames and $\gtrsim 1^\circ$ in narrow-angle frames. The final scan from which positional measurements were made was an average of these. Third, the average position of the inner and outer Encke edges was used as the inner fiducial feature. The averaging processes tend to minimize the effects of the Encke variation.

A series of solutions was obtained by spanning the range of pattern speeds $517^\circ.75 < \Omega_P < 519^\circ.25$ day^{-1} in increments of 0°.003 day^{-1} while holding Ω_P fixed and letting a, e, and $\tilde{\omega}_0$ vary. The solutions corresponding to minimum normalized residuals, $\chi^2_{\rm min}$, were examined. The error quoted here in any parameter, p, was obtained by evaluating $p(\chi^2_{\rm min} + 1) - p(\chi^2_{\rm min})$; i.e., the difference in the values of the parameter corresponding to the solutions of $\chi^2_{\rm min}$ and $\chi^2_{\rm min} + 1$. This yields a formal 1σ uncertainty.

Figure 1 shows the residuals per degree of freedom (χ^2/DOF) vs. pattern speed where DOF = the number of data points minus the number of free parameters. Acceptable solutions are obtained with a family of pattern speeds $\Omega_P = 518^\circ.312 \pm \Delta\Omega_P\, n \pm 0^\circ.04$ day^{-1}, where n is an integer and $\Delta\Omega_P = 0^\circ.18$ day^{-1}, corresponding to the rotation of one extra lobe between the sampling epochs. Pattern speed $\Omega_P = 518^\circ.31$ is indicated in Fig. 1 with the 1σ error bar. The seven minimum χ^2 solutions shown in Fig. 1 are equivalent: each yields

Fig. 1. The residuals per degree of freedom (χ^2/DOF), obtained by fitting a 7-lobed pattern to the radius-longitude data of the A ring edge, vs. pattern speed (°/day^{-1}) in the vicinity of the mass-weighted averaged mean motion of the co-orbital satellite system, $\overline{\Omega} = 518^\circ.291$ day^{-1}. The minimum-residuals solution closest to $\overline{\Omega}$, $\Omega_P = 518^\circ.31 \pm 0^\circ.04$ day^{-1}, is indicated by (a).

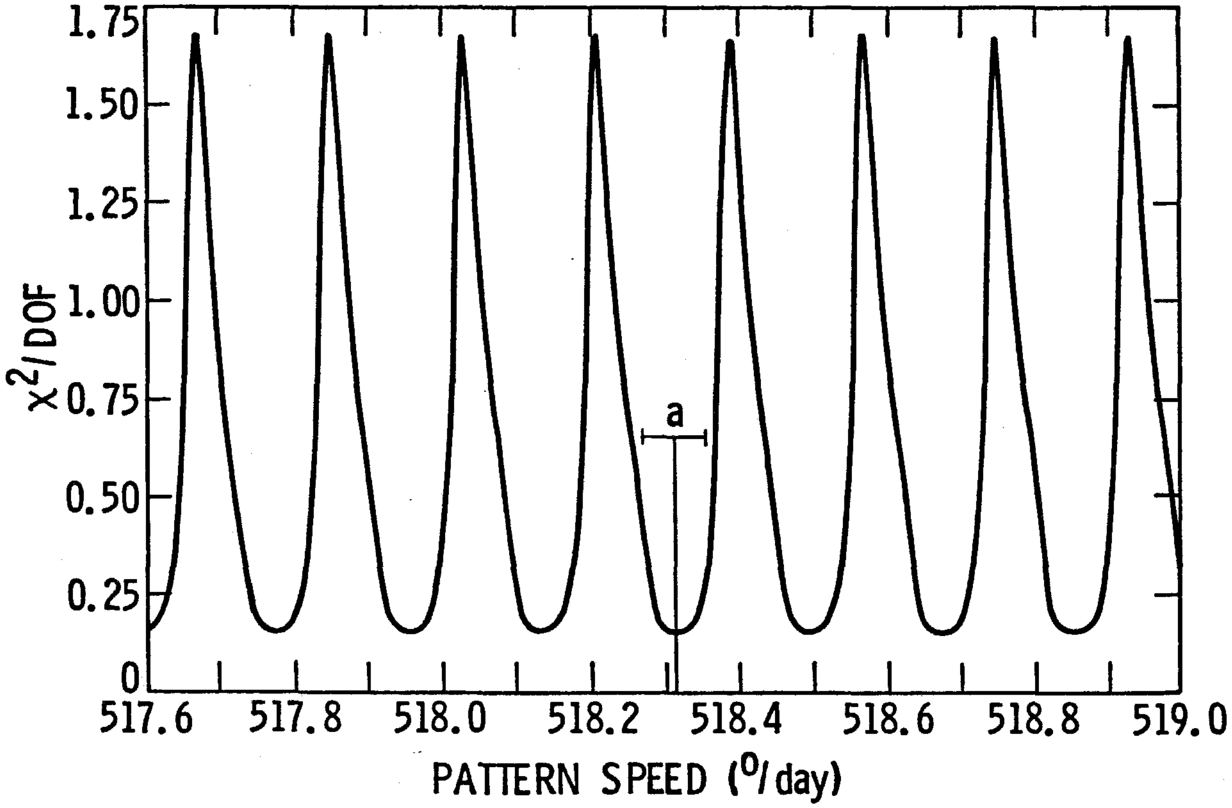
1.75
1.50
1.25
1.00
0.75
0.50
0.25
0
χ^2/DOF
a
517.6
517.8
518.0
518.2
518.4
518.6
518.8
519.0
PATTERN SPEED (°/day)

identical values of the 3 variable parameters a, e, and $\tilde{\omega}_0$ with $DOF = 7$. These are:

$$a = 136773 \pm 8 \text{ km}$$

$$e = 4.9\ (0.8) \times 10^{-5}$$

$$\tilde{\omega}_0 = 197^\circ \pm 10^\circ$$

$$\chi^2/DOF = 0.16 \quad .$$

The model solution with pattern speed closest to $\overline{\Omega}$, $\Omega_P = 518^\circ.31$ day^{-1}, is shown in Fig. 2. All data are precessed to the SOL system epoch. Fig. 2a displays the complete seven-lobed pattern. Four of the 7 lobes are sampled in this model. Fig. 2b shows the data folded onto one lobe with $\tilde{\omega}_0 = 197^\circ$.

The χ^2/DOF (= 0.16) is exceptionally small. The expected χ^2/DOF is 1.0 if the data are Gaussianly distributed around the model. The value obtained for this solution is a likely indication that the uncertainties assigned to the data were overestimated. This is not implausible in light of the previously mentioned difficulties in making these estimates.

To test the reality of the 7-lobed distortion, similar models with the number of lobes varying from 1 to 10 were tried. All yielded minimum residuals significantly higher than the 7-lobed model except one having 5 lobes. The lowest $\chi^2/DOF = 0.21$ for this model. Of course, there is no reason to suspect a 5-lobed distortion in the A ring edge: no strong $m = 5$ resonance with any known Saturnian satellite exists in this vicinity of the rings. The low χ^2/DOF for the 5-lobed model is probably an artifact of the incomplete sampling of the 7-lobed

Fig. 2. The 7-lobed model obtained for the A ring edge with Ω_P fixed at 518°.31 day^{-1}. The model parameters are given in text. Data points have been precessed to the SOL system epoch. Open circle is a Voyager 1 datum; filled circles are Voyager 2 data. a) Complete 7-lobed figure. b) Data folded onto one lobe with $\tilde{\omega}_0 = 197°$.

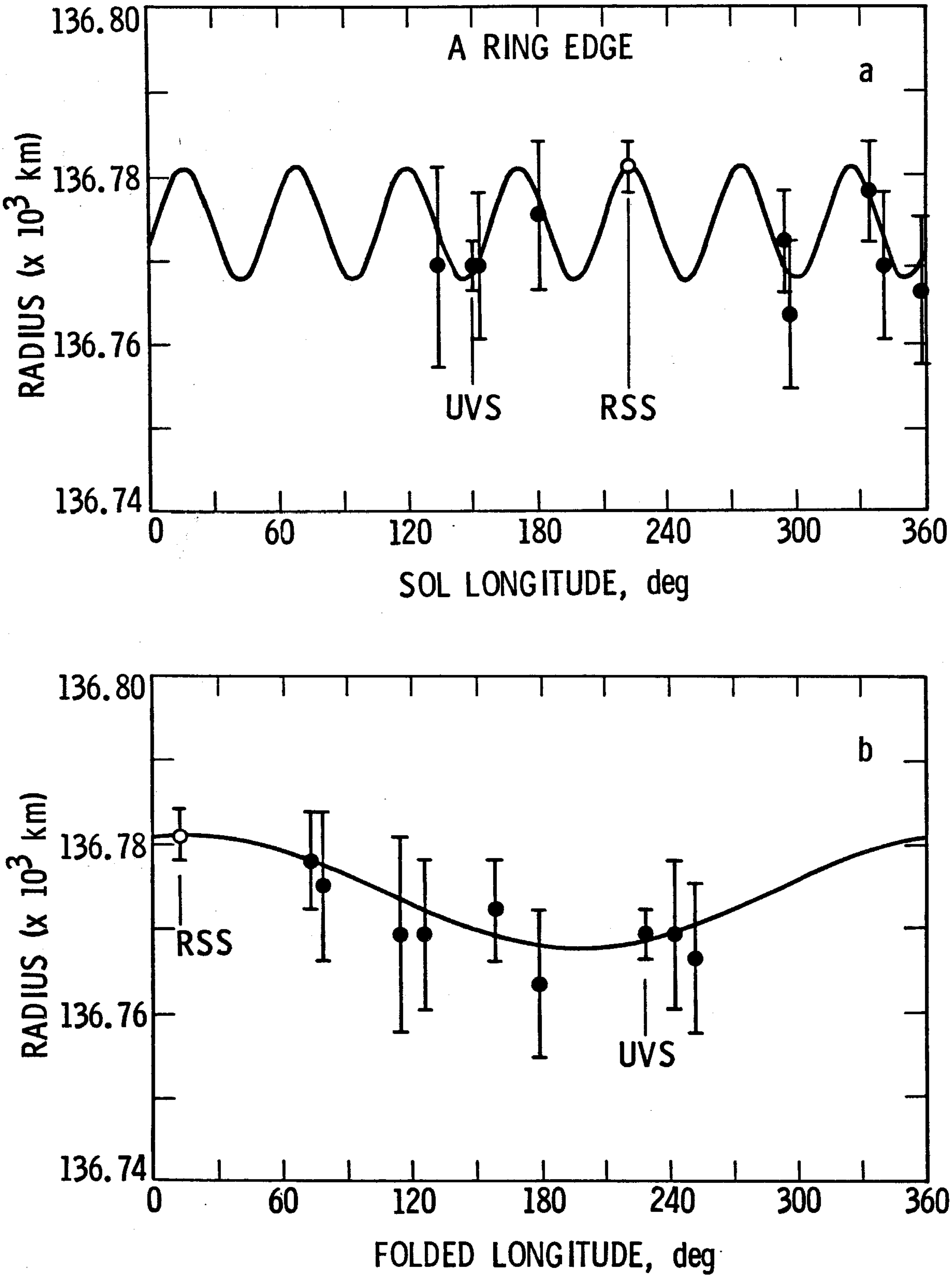
A RING EDGE
a
136.80
136.78
136.76
136.74
RADIUS (x 10^3 km)
UVS
RSS
0
60
120
180
240
300
360
SOL LONGITUDE, deg
b
136.80
136.78
136.76
136.74
RADIUS (x 10^3 km)
RSS
UVS
0
60
120
180
240
300
360
FOLDED LONGITUDE, deg

figure. However, it also indicates the degree to which our model for the A ring edge depends upon theoretical preconceptions. For a straight-line fit through the data, $\chi^2/DOF = 1.8$.

The semimajor axis is well-constrained by the data; no model solutions obtained from this study gave values for a differing by more than the 1σ uncertainty of $\sim \pm 1$ km. Thus it is believed that the semimajor axis quoted here, 136773 ± 8 km, is a model-independent result. Equivalent solutions are obtained with $\tilde{\omega}_0$ differing from the one given above by an integral number of $360°/7$.

It must be noted that there is only one Voyager 1 datum: the RSS occultation. It is this point alone which allows discrimination between pattern speeds separated by $360/(7\Delta T_2) < \Delta\Omega_P < 360/(7\Delta T_1)$, where ΔT_1 is the time interval spanned by the Voyager 2 data set, 1.2 days, and ΔT_2 is the total time interval between Voyager 1 and Voyager 2 epochs, 286 days. Our reliance on this single Voyager 1 datum would be worrisome were it not for its high precision. An error of $0°.1$ day^{-1} in the model solution Ω_P would require an error in the RSS observation of $\sim 9°$. The uncertainty in the SOL longitude of this observation is $\sim 0°.1$; the inaccuracy in the timing, < 1 min, is negligible.

3b. B Ring Edge

The initial 4-parameter solution for the B ring, with 9 degrees of freedom, was as follows:

$$a = 117577 \pm 15 \text{ km}$$

$$\tilde{\omega}_0 = 218^\circ \pm 11^\circ$$

$$e = 6.5\ (0.8) \times 10^{-4}$$

$$\Omega_P = 382^\circ.00 \pm 0^\circ.04\ \mathrm{day}^{-1}$$

$$\chi^2/DOF = 4.7 \quad .$$

The mean motion of Mimas is 381°.997 day^{-1}; its position in the SOL system at epoch is λ_{SOL} (Mimas) = 213° ± 1°. The solution pattern speed of the B ring is identical to Mimas' angular velocity. Note also that to within the formal uncertainty the periapse is aligned with the position of Mimas. The condition for closed orbits *interior* to a resonance imposed by basic resonance dynamics requires that conjunctions occur at periapse for test particle orbits. The 2:1 Mimas resonance location has been computed to be 117553 km, 24 km within the 4-parameter solution for the B ring edge semimajor axis. It is known that the inclusion of perturbations due to self-gravity and viscous stresses permits models in which the particle streamlines extend across the resonance location (Borderies et al. 1982). Thus the results reported here are consistent with the hypothesis of forcing by Mimas and we are justified in setting $\Omega_P = \Omega_s$, thus reducing the number of free parameters to 3. The best 3-parameter solution, with 10 degrees of freedom, is:

$$a = 117577 \pm 15\ \mathrm{km}$$

$$e = 6.3\ (0.8) \times 10^{-4}$$

$$\tilde{\omega}_0 = 215° \pm 6°$$

$$\chi^2/DOF = 4.3 \quad .$$

This solution is shown in Fig. 3. The SOL position of Mimas is indicated. The χ^2/DOF for this model, 4.3, is larger than those obtained from the model-fits of the other eccentric features in this study for which the data are of comparable quality (chapter III). It is plausible that the simple co-planar double-lobed model used here is insufficient to fully describe the B ring shape. Additional models will be investigated in the future.

4. Discussion

In light of the adequate sampling in radius and azimuth of the A ring edge, in particular the nearly extreme radial positions sampled by the high precision RSS and UVS data points, it can be said that the shape of the A ring edge is consistent with a 7-lobed distortion. The semimajor axis a = 136773 ± 8 km and the peak-to-peak variation of 14 ± 1 km are considered model-independent results of this analysis.

It is difficult to offer a precise interpretation of the kinematics of the A ring edge because of the complicated co-orbital resonance configuration in this region. The $k = 0$ (central) resonance is located at 136775 ± 2 km; the sidebands are spaced at intervals of ±3 km on either side. The A ring edge a = 136773 ± 8 km. To within the errors, the A ring edge overlaps the first several resonances ($0 \leq k \leq 3$) including the strongest ($k = 3$) for a mass ratio $M = 3.3$. (Resonances with $k < 0$ apparently fall outside the A ring). Note also from Table IIc that the pattern speeds for resonances with $0 \leq k \leq 3$ fall within the 1σ bounds of the model solution $\Omega_P = 518°.31 \pm 0°.04$ day^{-1}. The way in

Fig. 3. The model obtained for the B ring edge with Ω_P fixed at Ω (Mimas). Parameters are given in text. Data points have been precessed to the SOL system epoch. Open circles are Voyager 1 data; filled circles, Voyager 2. The position of Mimas in the SOL system at epoch is indicated.

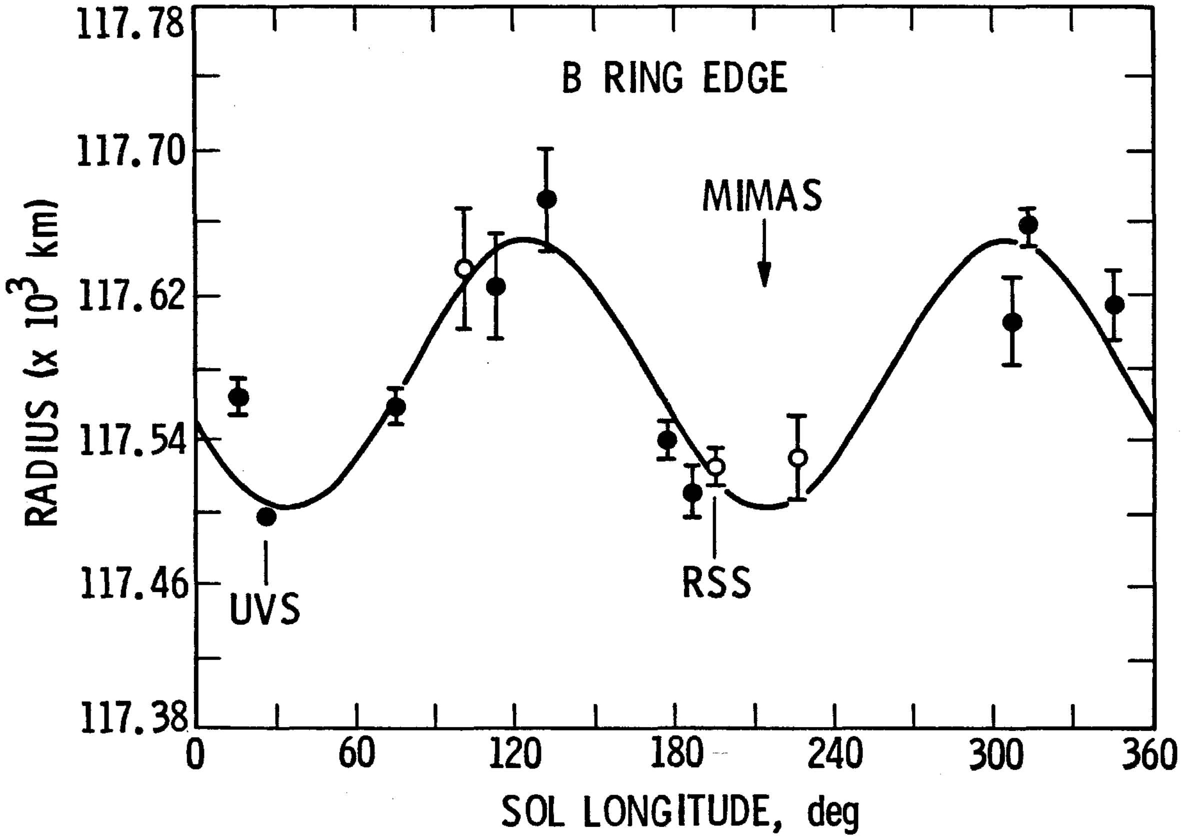
B RING EDGE
MIMAS
UVS
RSS
117.78
117.70
117.62
117.54
117.46
117.38
RADIUS (x 10^3 km)
0
60
120
180
240
300
360
SOL LONGITUDE, deg

which the disturbances produced at these closely-spaced resonances interfere is not well understood at the present time. The problem may be complicated further by the effects of self-gravity and collisional stresses which are presumably responsible for certain features of the B ring edge (see below). We can say however that the pattern speed of the A ring edge is consistent with the mass-weighted average angular velocity of the co-orbital system.

Several important features of the B ring can be deduced from the results obtained here. The amplitude of the variation in the B ring edge is $ae = 74 \pm 9$ km. Computations of the amplitude from test particle resonance dynamics indicate that the location where the particle streamlines begin to cross, i.e., where $a\partial a/\partial e = 1$, occurs for $ae = 21$ km. The self-gravity and viscous collisional stresses of the B ring particles are evidently responsible for the eccentricity enhancement and the location of the B ring edge outside the resonance position.

Self-gravity of the ring material is responsible for a portion of the perturbation of the particle orbit precession rates. The requirement that the orbits remain closed in the satellite frame consequently includes a term proportional to $\sum\limits_B$, the surface mass density of the perturbed region of the outer B ring: equation 25, Borderies et al. 1982. This equation is only a crude approximation as it treats the B ring edge as a single narrow ringlet. Using the B ring shape parameters obtained here, the solution of this equation indicates that $\sum_B$ is $O(> 10^2)$ gm/cm^2. Values obtained for other regions of the rings are of order 10-100 gm/cm^2 [see Esposito et al. (1983b) for references; chapter III]. It appears that the outer B ring may be not only a region of enhanced optical depth but also one of enhanced surface mass density.

The viscosity in unperturbed regions of the rings can be simply related to the velocity dispersion, V, and the optical depth (Goldreich and Tremaine 1982):

$$\nu \sim 0.5 \frac{V^2 \tau}{\Omega (1 + \tau^2)} \ .$$

Viscous dissipation in the outer region of the B ring will lead to a loss of energy and an angular separation, γ_B, between the periapse and the direction to Mimas. Angular momentum which enters the outer B ring must be transferred to Mimas if the outer edge is to remain stationary. Balancing the satellite torque on the ring with the rate of angular momentum flowing through it leads to an expression relating γ to ν in the outer B ring (Borderies et al.1982):

$$\sin\gamma \sim \frac{\nu}{\Omega (ma)^2} \left[\frac{M_p}{M_s} \right]^2 \ ,$$

where M_p and M_s are the planet and satellite masses, respectively, and m is the resonance label. The results found here are consistent with $0 < |\gamma| \lesssim 10°$. Using the upper value, ν is computed to be ~ 65 cm^2/sec; the corresponding velocity dispersion is $V \sim 0.2$ cm/sec. This implies a maximum ring height $h = V/\Omega < 10$ meters.

Ground-based observations of the rings seen edge-on yield values of h as large as 3 km. Interpretations of these observations in terms of the local ring thickness may be confused by effects such as optical depth enhancements for edge-on geometry, warping in the ring plane due to inclination resonances and the presence of a relatively few 1-2 km bodies (Shu et al. 1983; Henon 1981). It is not unreasonable that the typical vertical thickness of the ring plane is much less than that inferred from these observations. Values of h inferred from the damping of density and bending waves are of order 30 meters (Lane et al. 1982; Shu et al. 1983).

Inferences about the particle size distribution in the rings can be obtained from comparisons of ring observations over a broad range in wavelength. To date, only preliminary comparisons of this nature have been made. However, the Voyager RSS occultation experiment sensed particles of radius 1 cm and larger. The analysis of these data has revealed an apparent upper size limit of $r \sim 5$ meters and implies that most of the mass in the rings in concentrated in the 3-5 meter particles (Marouf et al. 1983). These results were derived at only 4 places in the rings: two in ring C and one each in the Cassini division and in ring A. The high optical depths for the B ring prevent such an analysis. However, if the mass in the B ring is also contained in the 3-5 meter particles, then the ring height upper limit derived here implies that at least dynamically the unperturbed ring plane may be considered a monolayer. This is the anticipated result for particles suffering sufficiently inelastic collisions. It also could imply that the massive particles are dominating the viscosity.

Without knowledge of the particle size distribution, it is difficult to unambiguously interpret the ring thickness inferred here. A more accurate measure of γ and h will hopefully be obtained in the future from a more satisfactory model for the B ring edge.

5. Conclusions

It is concluded from the analysis of Voyager imaging and occultation data of the A and B ring edges that:

1. the shape and kinematics of the B ring edge are determined primarily by its proximity to the Mimas 2:1 resonance. This confirms the results reported by Smith et al. (1982).

2. the data for the A ring edge are consistent with a 7-lobed distortion rotating with the mean angular velocity of the co-orbital satellite system. However, the dynamics in this region are complicated because the large libration of the co-orbital satellites gives rise to a set of closely-spaced resonances. These complications prevent us from giving a complete interpretation of the A ring kinematics at the present time.

3. the vertical thickness of the B ring in unperturbed regions is of order 10 meters, comparable to valued obtained from the analysis of spiral density and bending waves.

4. the shape of the B ring is apparently not completely described by a simple 2-lobed distortion which is co-planar with the rest of the ring plane. More complicated models will be tried in the future.

5. the semimajor axes and amplitudes of the A and B ring edges are:

$$a(B) = 117577 \pm 15 \text{ km}$$

$$ae(B) = 74 \pm 9 \text{ km}$$

$$a(A) = 136773 \pm 8 \text{ km}$$

$$ae(A) = 7 \pm 1 \text{ km}$$

The uncertainties in the a's include the systematic uncertainty (± 6 km) in the absolute radius scale determined by adopting the Saturn pole vector which brings the RSS and UVS/PPS into closest agreement. Any future changes in this scale must be applied to the values of the semimajor axes found in this analysis.

References

Borderies, N., Goldreich, P., and Tremaine, S. (1982). *Nature* **299**, 209.

Cuzzi, J.N. and Scargle, J. (1983). In preparation.

Goldreich, P. and Tremaine, S. (1982). *Ann. Rev. Astron. Astrophys.* **20**, 249.

Henon, M. (1981). *Nature* **293**, 33.

Lane, A.L., et al. (1982). *Science* **215**, 537.

Larson, S.M., Smith, B.A., Fountain, J.W., and Reitsema, H.J. (1981). *Icarus* **46**, 175.

Marouf, E.A., Tyler, G.L., Zebker, H.A., and Eshleman, V.R. (1983). *Icarus*, in press.

Null, G.W., Lau, E.L., Biller, E.D., and Anderson, J.D. (1981). *Astron. J.* **86**, 456.

Shu, F.H., Cuzzi, J.N., and Lissauer, J.J. (1983). *Icarus* **53**, 185.

Smith, B.A., et al. (1982). *Science* **215**, 504.

Yoder, C.F., Colombo, G., Synnott, S.P., and Yoder, K.A. (1983). *Icarus*, in press.

Chapter III. Narrow Eccentric Rings

1. Introduction

The main body of the Saturn ring system contains 3 major eccentric ringlets at 1.29, 1.45, and 1.95 R_s. By the time of Voyager 2 encounter in 1981, it was known that the shapes of these features are simple Keplerian ellipses with foci at Saturn's center. The latter two were observed to be precessing with rates expected from the multipole moments of Saturn (Smith et al. 1981, 1982). A multi-experimental analysis of Voyager data to study the 1.45 R_s ring has been made by Esposito et al. (1983a). They report an internal structure which is independent of azimuth as observed at ultraviolet and radio wavelengths, a mean optical depth across the ring of $\tau \sim 1$, and a surrounding gap essentially devoid of material ($\tau < 0.01$ in RSS, UVS, and PPS data). The ring's edges are sharp on a scale of ~ 1 km; its width varies from ~ 26 to ~ 100 km. Its precession rate is consistent with that expected from planetary oblateness. Some of these characteristics are shared by the Uranian rings, in particular the ε ring. The remaining two narrow ringlets at 1.29 and 1.95 R_s have until now not been analyzed in detail.

Tentative names have been assigned to these rings and will be used freely in the remainder of this chapter. The ring at 1.29 R_s is called the Titan ring because of its proximity to the 1:0 apsidal resonance with Titan. No official name has been given to the gap in which this ringlet sits. We call it the Titan gap. The 1.45 and 1.95 R_s rings, which lie in the Huygens and Maxwell gaps, are called the Huygens and Maxwell rings, respectively (see Plates 1-3).

The study of the shapes and kinematics of the eccentric Saturnian ringlets is described in this chapter. The basic properties of these features reported in Smith et al. (1981, 1982) and Esposito et al. (1983a) are confirmed. It is found that the rings at 1.29 R_s and 1.95 R_s are kinematically different than the Uranian and Huygens rings. The eccentricity and precession rate of the Titan ring are apparently completely determined by resonant forcing by Titan; the Maxwell ring, though not completely understood, appears to be forced in part by Mimas and the B ring. The requirement that differential precession in the Titan and Huygens rings be prevented by their internal self-gravity yields estimates of the ring masses, surface mass densities and specific opacities.

2. Ring Models

Comparisons of the imaging observations of the narrow rings, taken at different times and widely different azimuths, indicate that they are precessing as units; i.e., there appears to be no differential precession between inner and outer edges. The centerline of each ring was fitted in the least-squares sense with a model describing a uniformly precessing, low eccentricity ellipse with focus at Saturn's center and which is coplanar with the broader rings: i.e.,

$$r = a\left\{1 - e\cos\left[\vartheta - \tilde{\omega}_0 + \dot{\tilde{\omega}}(t - t_0)\right]\right\} \quad , \tag{1}$$

where a is the semimajor axis, e is the eccentricity, $\tilde{\omega}_0$ is the SOL longitude of periapse at epoch, t_0, $\dot{\tilde{\omega}}$ is the rate of apsidal precession, and r, ϑ, and t are the observed radius of the centerline, the SOL longitude and the time of the observation, respectively. The data were weighted by the inverse square of their errors. (Tables IIIa,b,c list the data for these three features). Four parameters were allowed to vary: a, e, $\tilde{\omega}_0$, and $\dot{\tilde{\omega}}$. *A priori* information regarding the

Table IIIa. Titan Ringlet

Experiment* ID	Voyager S/C	Camera/ Filter	Ring Plane Resolution (km)	Radius (scaled)	Error (scaled)	Time from Epoch (days)	SOL Longitude (deg)
34935.23	1	NA/clear	14	.356	.005	−0.287	10
UVS/PPS[1]	1	–	7	.342	.003	−0.024	176.4
RSS	1	–	3	.338	.001	0.149	115.5
43860.07	2	NA/clear	52	.356	.005	281.301	71
43861.02	2	NA/clear	49	.339	.005	281.332	253
43935.37	2	NA/violet	29	.353	.005	283.818	67
43995.02	2	NA/clear	4	.353	.001	285.799	32
43995.28	2	NA/clear	5	.342	.002	285.813	231
UVS/PPS[2]	2	–	4	.359	.002	285.869	345.3
UVS/PPS[3]	2	–	3	.342	.001	286.017	198.0

$\Delta = 2058 \pm 1$ km

$f_1 = 77155 \pm 1$ km

* FDS #'s for ISS data

[1] i Her exit

[2] δ Sco entrance

[3] δ Sco exit

Table IIIb. Huygens Ringlet

Experiment* ID	Voyager S/C	Camera/ Filter	Ring Plane Resolution (km)	Radius (scaled)	Error (scaled)	Time from Epoch (days)	SOL Longitude (deg)
34881.37	1	NA/clear	25	.480	.006	-2.080	73
34884.13	1	NA/clear	26	.499	.004	-1.993	256
34935.31	1	NA/clear	15	.478	.004	-0.283	359
RSS	1	---	1	.503	.002	0.166	122.0
34956.43	1	WA/clear	49	.490	.010	0.424	60
43858.29	2	NA/clear	55	.499	.011	281.240	71
43858.33	2	NA/clear	57	.490	.009	281.149	253
43935.37	2	NA/violet	27	.491	.010	283.818	67
43994.50	2	NA/clear	4	.487	.001	285.792	33
43995.40	2	NA/clear	5	.498	.001	285.819	233
43999.28	2	WA/clear	23	.500	.005	285.947	222
UVS/PPS	2	---	5	.495	.002	285.999	196.5

$\Delta = 2352 \pm 1$ km

$f_1 = 86336 \pm 1$ km

* FDS #'s for ISS data

Table IIIc. Maxwell Ringlet

Experiment* ID	Voyager S/C	Camera/ Filter	Ring Plane Resolution (km)	Radius (scaled)	Error (scaled)	Time from Epoch (days)	SOL Longitude (deg)
RSS	1	-	5	.529	.002	0.156	135.7
34956.55	1	WA/clear	55	.533	.005	0.430	62
34962.52	1	WA/clear	62	.517	.007	0.628	221
43864.48	2	NA/clear	53	.534	.005	281.458	71
43865.00	2	NA/clear	48	.526	.006	281.464	254
43912.04	2	NA/clear	36	.532	.003	283.033	69
43968.33	2	NA/clear	16	.534	.002	284.916	60
43968.41	2	NA/clear	45	.521	.006	284.920	354
43989.46	2	NA/clear	7	.536	.002	285.623	48
43993.06	2	NA/clear	6	.519	.002	285.734	243
43998.25	2	WA/clear	27	.526	.004	285.910	209
43999.40	2	WA/clear	20	.528	.002	285.953	223
UVS/PPS	2	-	4	.523	.001	286.060	192.6

$\Delta = 4719 \pm 5$ km

$f_1 = 115336 \pm 4$ km

* FDS #'s for ISS data

expected behavior of each feature was used to determine the input parameter for $\dot{\tilde{\omega}}$. The solution, $\{a\ , e\ , \tilde{\omega}_0\ , \dot{\tilde{\omega}}\}$, yielding lowest residuals was examined.

2a. 1.29 R_s

Equation 1 of chapter II gives the condition on the angular frequency of a perturbing satellite and the precession rate of orbits at a Lindblad resonance. An $m = 1$ resonance is called an 'apsidal' resonance and occurs where the pattern speed equals the rate of apsidal precession. The strongest resonances have pattern speeds equal to the satellite's angular frequency. The proximity of the 1.29 R_s ringlet to the 1:0 apsidal resonance with Titan suggested investigation of precession rates near Titan's mean motion, $22^\circ.577$ day^{-1}.

The 4 variable-parameter solution for this feature, with 6 degrees of freedom, is as follows:

$$a = 77871 \pm 8 \text{ km}$$

$$e = 2.6(0.2) \times 10^{-4}$$

$$\tilde{\omega}_0 = 128^\circ \pm 16^\circ$$

$$\dot{\tilde{\omega}} = 22^\circ.57 \pm 0^\circ.06 \text{ day}^{-1}$$

$$\chi^2/DOF = 0.82 \quad .$$

The location of the Titan 1:0 apsidal resonance is 77796 km; the errors in this value are large, of order 50-100 km, and are due to the uncertainties in Saturn's gravity coefficients (Null et al. 1981). The 1.29 R_s ring lies outside the nominal resonance position. At the SOL system epoch, the position of Titan is λ_{SOL}(Titan)

= 322° ± 1°. To within the formal uncertainties of this solution, the ring is precessing with Titan's mean motion; its apoapse is pointing to Titan. The alignment of the apoapse with the satellite's position is the expected result for orbits exterior to a resonance (chapter II, equation 6).

The simplest interpretation of these results is that the ring is stationary in Titan's reference frame with its eccentricity entirely forced by Titan. Under this assumption, it is reasonable to set the precession rate $\dot{\varpi} \equiv \Omega_{\text{Titan}}$ and to solve for 3 parameters with 7 degrees of freedom:

$$a = 77871 \pm 7 \text{ km}$$

$$e = 2.6(0.2) \times 10^{-4}$$

$$\varpi_0 = 129^\circ \pm 5^\circ$$

$$\chi^2/DOF = 0.7 \quad .$$

This solution is shown in Fig. 1. The data points have been precessed to the SOL system epoch using $\dot{\varpi} = 22^\circ.577 \text{ day}^{-1}$. Two of the UVS data points are coincident for this model. The position of Titan at the time of Voyager 1 encounter is indicated. The angular separation between the ring's apoapse and Titan's position is -13° ± 5° for this model.

2b. 1.45 R_s

There are no strong resonances near the Huygens ring at 1.45 R_s. Models with $\dot{\varpi}$ near the value expected from planetary oblateness were examined. The resulting solution, with 8 degrees of freedom, is shown in Fig. 2. The solutions for the 4 parameters are:

Fig. 1. The co-planar Keplerian ellipse, with apse precession rate fixed at Ω (Titan), which best fits the radius-longitude data for the Titan ringlet at 1.29 R_s. Parameters are given in text. Data points have been precessed to the SOL system epoch. Open circles are Voyager 1 data; filled circles, Voyager 2. The position of Titan in the SOL system at epoch is indicated.

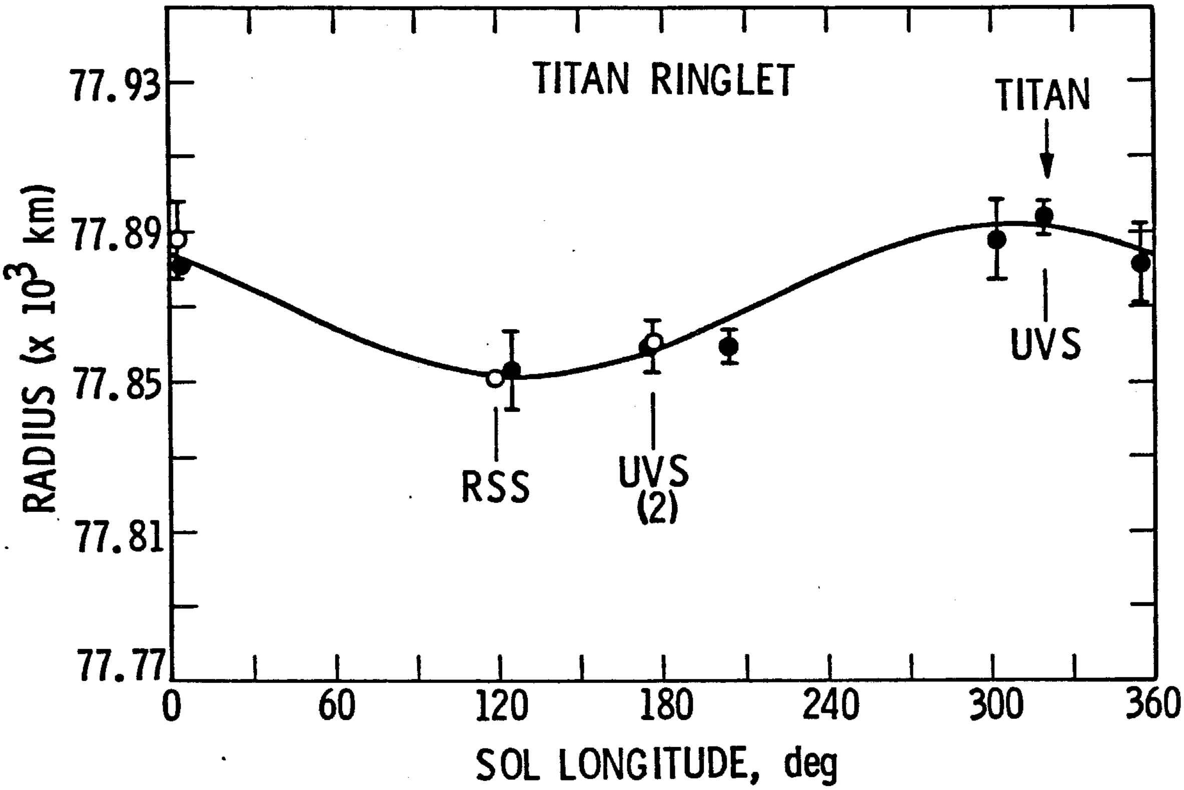
TITAN RINGLET
TITAN
UVS
RSS
UVS (2)
RADIUS (x 10^3 km)
77.93
77.89
77.85
77.81
77.77
0
60
120
180
240
300
360
SOL LONGITUDE, deg

Fig. 2. The best-fitting co-planar Keplerian ellipse obtained for the Huygens ringlet at 1.45 R_s. Parameters are given in text. Data points have been precessed to the SOL system epoch. Open circles are Voyager 1 data; filled circles, from Voyager 2.

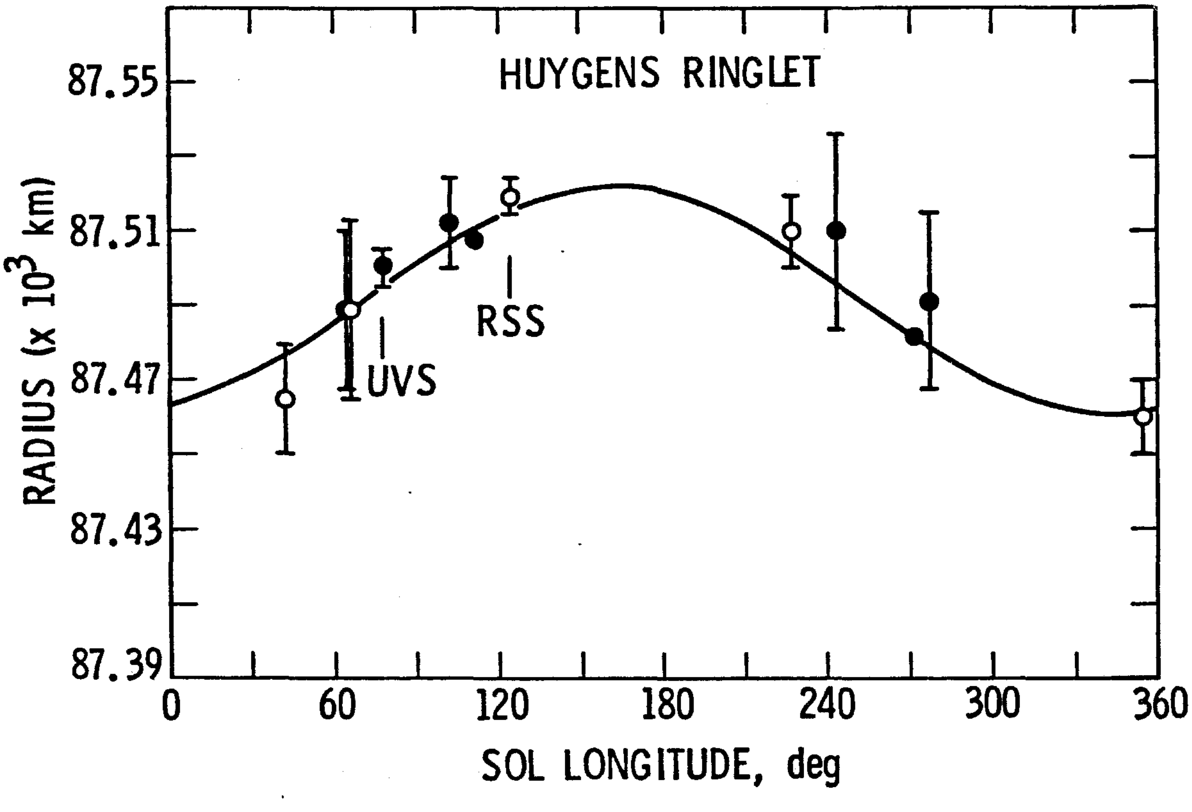
HUYGENS RINGLET
UVS
RSS
RADIUS (x 10^3 km)
87.55
87.51
87.47
87.43
87.39
0
60
120
180
240
300
360
SOL LONGITUDE, deg

$$a = 87491 \pm 8 \text{ km}$$

$$e = 3.4(0.4) \times 10^{-4}$$

$$\tilde{\omega}_0 = 342^\circ \pm 9^\circ$$

$$\dot{\tilde{\omega}} = 14^\circ.69 \pm 0^\circ.03 \text{ day}^{-1}$$

$$\chi^2/DOF = 0.70 \quad .$$

At a radius of 87491 km, the precession caused by planetary oblateness (equation 2, chapter II) is $14^\circ.68 \pm 0^\circ.05$ day^{-1}; the uncertainty is due to the formal errors in the values of J_2 and J_4 (Null et al. 1981). To within the formal uncertainties of this solution, $\dot{\tilde{\omega}} = \dot{\tilde{\omega}}_p$; this feature is apparently freely precessing in the multipole moments of Saturn's gravity field.

2c. 1.95 R_s

From Voyager images containing this feature (Plate 1), it is apparent that to first order the shape of the 1.95 R_s ringlet is a simple Keplerian ellipse, unlike the double-lobed figure of the B ring edge. The radius-longitude data were fitted initially with a Keplerian model; a precession rate near the value expected from planetary oblateness alone, $5^\circ.01$ day^{-1}, was used as an input parameter for $\dot{\tilde{\omega}}$. This model proved to be inadequate to fully describe the ring:

$$a = 117828 \pm 11 \text{ km}$$

$$e = 2.3(0.6) \times 10^{-4}$$

$$\tilde{\omega}_0 = 235^\circ \pm 28^\circ$$

$$\dot{\tilde{\omega}} = 5^\circ.01 \pm 0^\circ.12 \text{ day}^{-1}$$

$$\chi^2/DOF = 1.87 \quad .$$

The residuals, $\chi^2/DOF = 1.87$, are significantly higher than those for the previous two rings. No Keplerian co-planar elliptical model with a plausible precession rate had residuals lower than ~ 1.8. Elliptical ring models including inclination were tried for the Maxwell ring but yielded unsatisfactory results. A weighted straight-line fit through the data yields $\chi^2/DOF = 6.6$.

The Maxwell ring lies within 275 km of one of the strongest resonances in the Saturn ring system, the 2:1 inner Lindblad resonance with Mimas, and within ~ 250 km of the edge of the optically thick B ring. The possibility that the ring is significantly distorted by Mimas and the eccentric B ring was explored by fitting a model consisting of the linear superposition of two components:

$$r = a\left\{1 - e\cos\left[\vartheta - \tilde{\omega}_0 + \dot{\tilde{\omega}}(t - t_0)\right] - e_f\cos2\left[\vartheta - \tilde{\omega}_f + \Omega_P(t - t_0)\right]\right\} \quad . \tag{2}$$

The second term describes an $m = 2$ pattern with periapse angle, $\tilde{\omega}_f$, pattern speed, Ω_P, and forced eccentricity, e_f. Initially, 6 parameters were allowed to vary and $\Omega_P \equiv \Omega_{\text{Mimas}}$.

The solution of lowest residuals near $\dot{\tilde{\omega}} = 5^\circ.01 \text{ day}^{-1}$ with DOF = 7, is:

$$a = 117828 \pm 11 \text{ km}$$

$$e = 2.7(1.0) \times 10^{-4}$$

$$e_f = 1.3(0.9) \times 10^{-4}$$

$$\tilde{\omega}_0 = 213^\circ \pm 28^\circ$$

$$\tilde{\omega}_f = 303^\circ \pm 17^\circ$$

$$\dot{\tilde{\omega}} = 5^\circ.11 \pm 0^\circ.12 \text{ day}^{-1}$$

$$\chi^2/DOF = 1.91 \quad .$$

The χ^2/DOF for this model is comparable to that of the Keplerian model. In addition, the amplitude of the forced component, ae = 15 ± 10 km, is not significant at the 2σ level. From these considerations it would appear that the two component model is not an improvement on the simple Keplerian model. However, there is some indication from the former that the forcing by Mimas and the B ring is significant. The position of the 2:1 resonance with Mimas is 117553 ± 2 km. The model solution for a indicates that the ring lies outside the resonance. For this configuration the line joining the radial maxima of the forced component should be aligned with the satellite. The position of Mimas in the SOL system at epoch is λ_{SOL}(Mimas) = 213° ± 1°. The 6 parameter solution for the SOL longitude of the radial maximum of the forced component is $\tilde{\omega}_f$ - 90° = 213° ± 17°, identical to λ_{SOL}(Mimas).

In effect, the eccentric B ring edge behaves like an external satellite at the angular location of Mimas. Its radial minima point to Mimas. As a consequence, its inward-directed perturbation on the Maxwell ring is least (greatest) at those azimuths where the outward-directed perturbation due to Mimas is the greatest (least). Therefore, the evidence presented above applies equally well to the case of forcing by the B ring.

Assuming the reality of the forced component, we are justified in setting $\Omega_P \equiv \Omega_{\mathrm{Mimas}}$ and $\tilde{\omega}_f \equiv \lambda_{SOL}(\mathrm{Mimas}) + 90°$. (In doing so, we are neglecting the possibility that viscous stresses in the ring have caused a measurable angular separation between the radial maximum of the Maxwell ring and the direction to the satellite).

The resulting solution with 5 variable parameters and DOF = 8 is:

$$a = 117828 \pm 11 \text{ km}$$

$$e = 2.7(0.8) \times 10^{-4}$$

$$\tilde{\omega}_0 = 213° \pm 26°$$

$$\dot{\tilde{\omega}} = 5°.11 \pm 0°.11 \text{ day}^{-1}$$

$$e_f = 1.3(0.9) \times 10^{-4}$$

$$\chi^2/DOF = 1.68 \quad .$$

In Fig. 3a, the Maxwell ring data are precessed to the SOL epoch using the solution $\dot{\tilde{\omega}}$ given above and plotted against the major (Keplerian) component. (Inspection of Fig. 3a confirms the inadequacy of a single component model). The shape of the Maxwell ring in the two component model undergoes rapid changes due to the vastly different angular frequencies, 5°.01 day^{-1} and 381°.997 day^{-1}, of the two components. The forced component may be thought of as a

Fig. 3. The current best-fitting two component model obtained for the Maxwell ringlet at 1.95 R_s. a) The major component, a co-planar Keplerian ellipse, is plotted against SOL longitude. The radius-longitude data have been precessed to the SOL system epoch using the apse precession rate obtained for this component, $\dot{\tilde{\omega}} = 5^\circ.11$ day^{-1}. b) The forced component, a double-lobed Saturn-centered pattern, is plotted against SOL longitude. This model was obtained by fixing the pattern speed $\Omega_P = \Omega$ (Mimas) = 381°.997 day^{-1} and the periapse $\tilde{\omega}_f$ = λ_{SOL}(Mimas) + 90° = 303°. The position of Mimas at the SOL epoch is indicated. The data (differenced radius vs. longitude) have been precessed to the SOL system epoch using Ω_P = 381°.997 day^{-1}. See text for parameters and further explanation. In a) and b), open circles are Voyager 1 data; filled circles, Voyager 2.

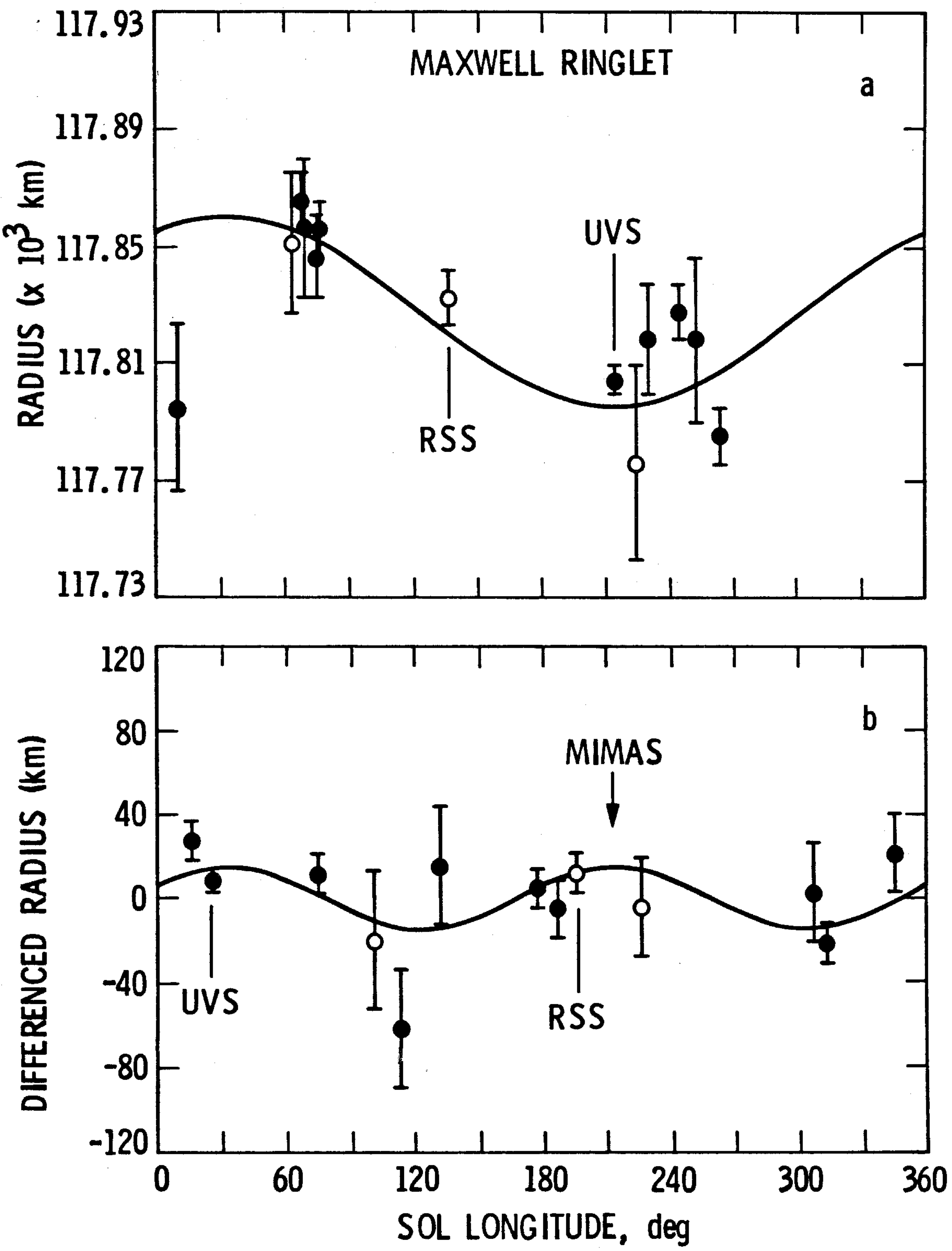
MAXWELL RINGLET
a
RADIUS (x 10^3 km)
117.93
117.89
117.85
117.81
117.77
117.73
UVS
RSS
b
DIFFERENCED RADIUS (km)
120
80
40
0
-40
-80
-120
MIMAS
UVS
RSS
0
60
120
180
240
300
360
SOL LONGITUDE, deg

wave disturbance with an azimuthal dependence $\propto \cos 2\left[\vartheta - \lambda_{SOL}(\text{Mimas})\right]$ traveling around the ring with $\Omega_P = \Omega_{\text{Mimas}}$. Consequently, the deviations of the data points from the Keplerian curve in Fig. 3a are time-dependent and will vary with a frequency equal to $(\Omega_{\text{Mimas}} - \dot{\tilde{\omega}})/180 = 2.1$ cycles/day. A visual representation of the 'goodness of fit' of the forced component was obtained by using the deviations from the Keplerian component as radii, precessing the data to the SOL epoch using $\Omega_P = 381^\circ.997$ day^{-1}, and plotting the data (differenced radius vs. precessed SOL longitude) and the forced component model in the SOL system. The results are shown in Fig. 3b. The position of Mimas in the SOL system at epoch is indicated.

The solution for $\dot{\tilde{\omega}}$ is consistent with the value expected for free precession, though it is surprising that the nominal solution differs from $\dot{\tilde{\omega}}_p$ by as much as $0^\circ.1$ day^{-1}. This may have implications for estimating the surface mass density, $\sum_B$, in the outer B ring (see section 4).

Note that the periapse of the Keplerian component is aligned with Mimas at the SOL system epoch; i.e., $\tilde{\omega}_0 = \lambda_{SOL}(\text{Mimas})$. There is no reason to suspect a kinematical relation between Mimas and the orientation of the apsidal line of the freely precessing component. Moreover, it is unlikely that this coincidence represents incomplete separation in time of the two components. The observations made during Voyager 2 encounter extended over ~ 4.5 days during which the radial deviations of the data points from the Keplerian curve executed ~ 9.5 cycles. The locations of the Voyager 2 data in Fig. 3b reveal the high degree to which the second component is sampled in azimuth during this time interval.

It is possible that the apsidal alignment of the free component with

Mimas is a result of using a linear superposition of components in place of a model which incorporates interactions between them. Note also that the scatter of the data around the curve in Fig. 3b is large. This may be an additional indication that important dynamical effects have been overlooked in studying the Maxwell ring. Further observational and theoretical analysis of this feature is required to reach a thorough understanding of its behavior.

3. Width-Radius Relations

Figures 4 and 5 show the relations between the radial (FWHM) width and the radius for the Titan and Huygens rings, respectively. Only those ISS data for which the feature was resolved were used. The Titan ringlet was not resolved in the RSS data for which the resolution was limited by diffraction. The RSS datum for this feature represents an upper limit in width. The solid lines are least-squares fits to the data, weighted by the errors in the widths only:

$$1.29\ \mathrm{R_s}: \qquad W(R) = 0.616\,(R - 77830) \quad ,$$

$$1.45\ \mathrm{R_s}: \qquad W(R) = 0.803\,(R - 87440) + 23 \quad ,$$

where W is the width and R is the radius, in km. The minimum and maximum model widths and model radii are indicated on the ordinate and the abscissa, respectively. Clearly, these figures are well-fitted by straight lines of positive slope.

The time scale over which differential precession due to oblateness would circularize a narrow Saturnian ring of non-interacting particles is very short, $< 10^2$ years. This time scale is lengthened for an optically thick ring in which collisions are important (Borderies et al. 1983), but it is still relatively short,

Fig. 4. Width-radius relation for the Titan ringlet. Open circles are Voyager 1 data; filled circles are Voyager 2 data. The straight line is a weighted least-square fit to these data. The maximum and minimum model widths and radii are indicated on the ordinate and abscissa, respectively. The RSS datum is an upper limit.

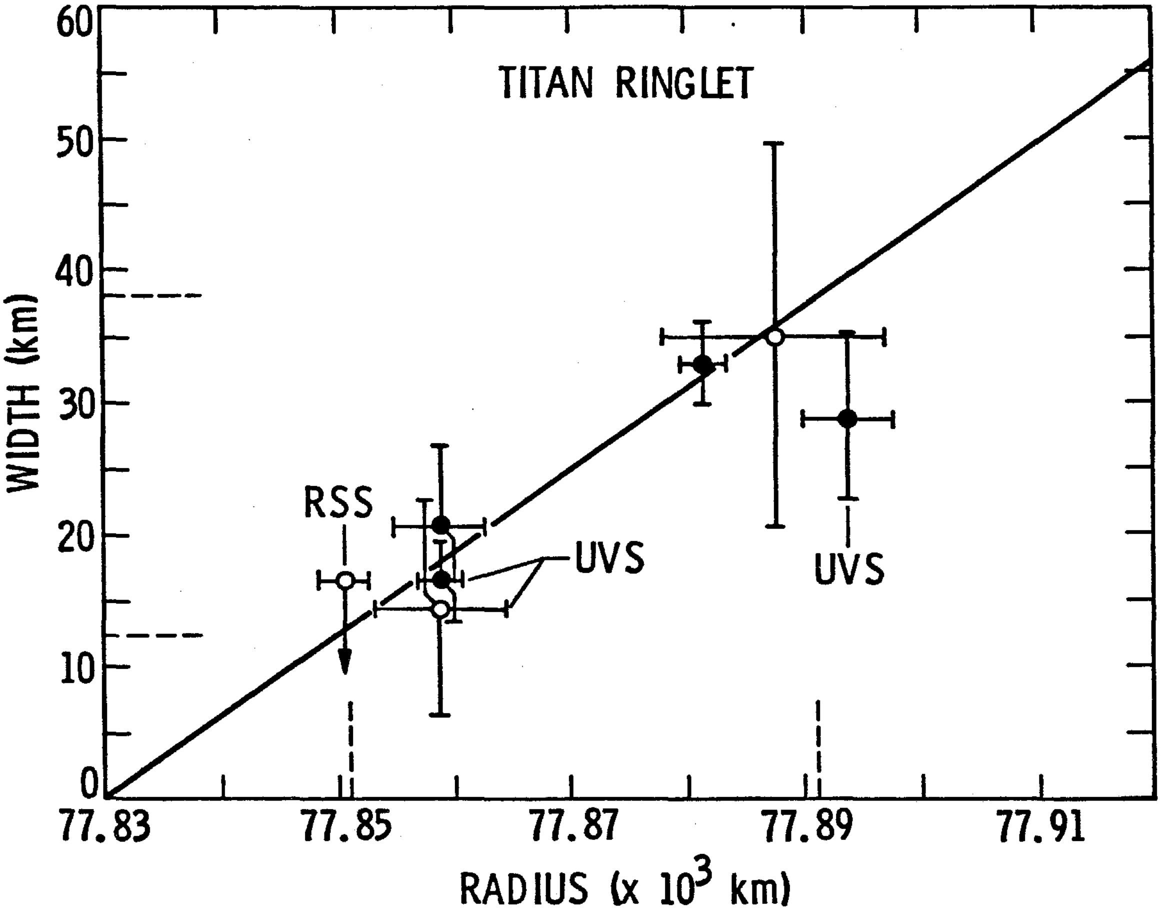
TITAN RINGLET
WIDTH (km)
0
10
20
30
40
50
60
RADIUS (x 10^3 km)
77.83
77.85
77.87
77.89
77.91
RSS
UVS
UVS

Fig. 5. Width-radius relation for the Huygens ringlet. Open circles are Voyager 1 data, filled circles are Voyager 2 data. The straight line is a weighted least-square fit to these data. The maximum and minimum model widths and radii are indicated on the ordinate and abscissa, respectively.

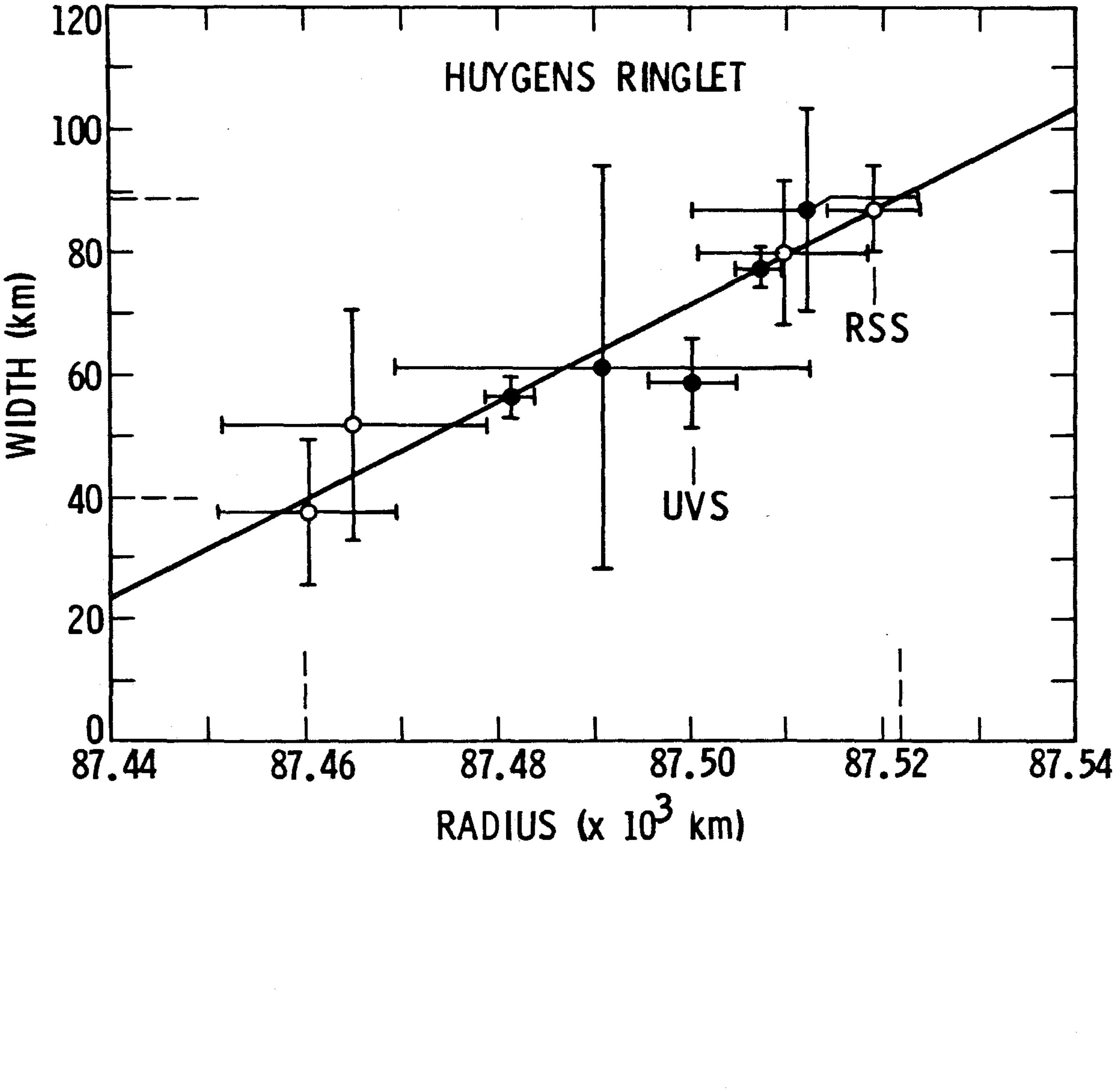
HUYGENS RINGLET
WIDTH (km)
RADIUS (x 10^3 km)
0
20
40
60
80
100
120
87.44
87.46
87.48
87.50
87.52
87.54
RSS
UVS

$\sim 10^6$ years. Goldreich and Tremaine (1979a) have shown that a possible mechanism for preventing differential precession in a narrow ring is the self-gravity of the constituent particles. A necessary requirement of this mechanism is a positive eccentricity gradient, $\delta e/\delta a > 0$, across the ring. The positive width-radius relations for the Titan and Huygens rings are consistent with this hypothesis. This is particularly significant for the Titan ring: in the absence of self-gravity its eccentricity gradient would be negative owing to its position exterior to the resonance.

The masses of these two rings can be calculated once the eccentricity gradients are known. Implicit in this calculation is the assumption that the gradient has adjusted itself to balance the opposing effects of self-gravity and differential precession. (In the case of the Titan ring, the tendency for differential precession includes the perturbing effect of Titan). To determine the eccentricity gradients, the data for the inner and outer boundaries of the rings were fitted with elliptical models in which $\dot{\tilde{\omega}}$ was held fixed at the value determined for the centerline. Only those data in which the rings were resolved were used. The ranges in a and e across each ring, δa, and δe, are tabulated in rows 5 and 6 of Table IIId. The masses, M_r, determined by a numerical procedure described in Goldreich and Tremaine (1979b), with a modification due to the effect of Titan for the 1.29 R_s ring, are listed in row 9. To first order in e, the mass in the ring is evenly distributed in azimuth. The linear mass density is given by $L = M/2\pi a$. The mean surface mass density, $\sum = L/\overline{W}$, where $\overline{W}$ is the ring's mean width, is listed in row 10 for each ring.

Reliable optical depths have been determined from the UVS/PPS data only. The mean optical depth across the ring and the width are $\tau \sim 1.0$ and W = 57 km for 1.45 R_s; $\tau \sim 1.8$ and W = 18 km for 1.29 R_s in the δ Sco occultation.

TABLE IIId

	Titan Ringlet[2] (1.29 R_s)	Huygens Ringlet (1.45 R_s)
1. a (km)[1]	77871 ± 7	87491 ± 8
2. e (10^{-4})	2.6 ± 0.2	3.4 ± 0.4
3. $\tilde{\omega}_0$	129° ± 5°[3]	342° ± 9°
4. $\dot{\tilde{\omega}}$ (°/day)	22.577	14.69 ± 0.03
5. δa (km)	25 ± 3	64 ± 3
6. δe (10^{-4})	1.4 ± 0.4	3.4 ± 0.6
7. r_i (km)[1] [e_{up}]	77735 ± 12	87322 ± 8 [1×10^{-4}]
8. r_o (km)[1] [e_{up}]	77919 ± 8 [8×10^{-5}]	87590 ± 8 [1×10^{-4}]
9. M_r (10^{18}gm)	2.1	6.1
10. Σ (gm/cm^2)	17	17
11. κ (cm^2/gm)	.075	.052

[1] Error includes the systematic uncertainty in absolute radius of ±6 km.

[2] Solution for $\dot{\tilde{\omega}} \equiv \Omega(\text{Titan}) = 22^{\circ}\!.577$ day^{-1}.

[3] λ_{SOL}(Titan) + 180° = 142° ± 1°.

These values may be used to compute the specific opacity (i.e., the optical extinction cross-section per unit mass), $\kappa = \tau W/L$, at a particular location in the ring. Normal optical depth is inversely related to width for a ring with L independent of azimuth. This is observed in the Uranian α, β, and ε rings for which optical depth and width measurements have been obtained at varying azimuths (Nicholson et al. 1982). For these rings, κ is independent of azimuth. Assuming this to be true for the Saturnian rings as well, we find for the Titan ring $\kappa = 0.075$ cm^2/gm; for the Huygens ring, $\kappa = 0.052$ cm^2/gm.

Figure 6 displays the width-radius relation for the Maxwell ring. A weighted linear least-squares fit to these data was not satisfactory: the result was consistent with relations of either positive or negative slope. The appearance of Fig. 6 provides strong evidence that this feature in significantly different than the Titan or Huygens rings. The measurements of $\delta e/\delta a$ and the calculation of the mass and specific opacity will be deferred until the shape and kinematics of the Maxwell ring have been satisfactorily explained.

4. Discussion

The Huygens ring is the most readily understood of the Saturnian eccentric rings. There are no strong resonances near this feature. Its eccentricity is presumably unforced by resonant perturbations from distant satellites; its motion is consistent with free precession in Saturn's non-spherical gravity field. The observed positive linear eccentricity gradient is consistent with the hypothesis of suppression of differential precession through the collective self-gravitating behavior of its ring particles. Its model width varies from 40 to 88 km. The mass and $\sum$ are 6.1×10^{18} gm and 17 gm/cm^2, respectively. Esposito et al. (1983a) have compared the radial profile of the

Fig. 6. Width-radius relation for the Maxwell ringlet. Open circles are Voyager 1 data; filled circles are Voyager 2 data.

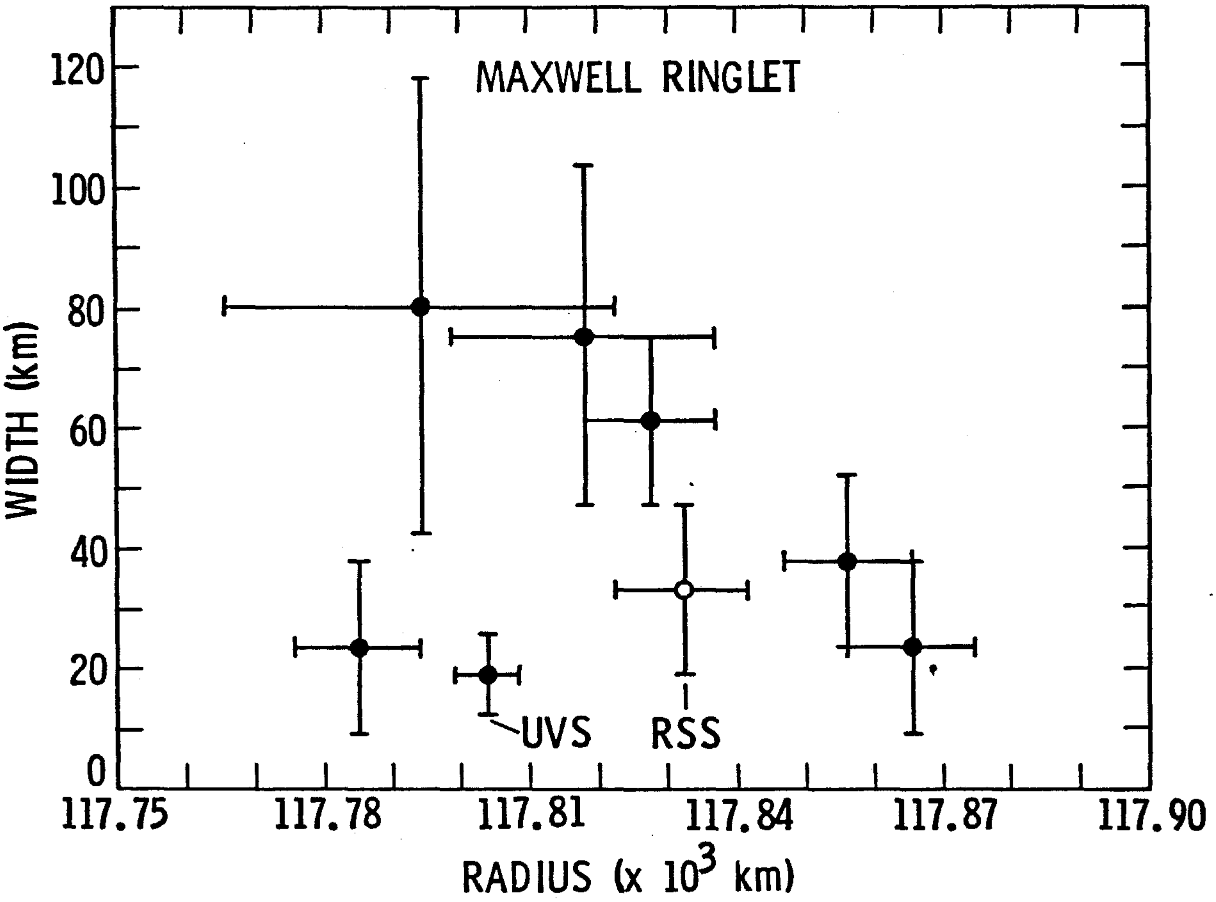
MAXWELL RINGLET
WIDTH (km)
0
20
40
60
80
100
120
117.75
117.78
117.81
117.84
117.87
117.90
RADIUS (x 10³ km)
UVS
RSS

1.45 R_s ring in the UVS, PPS, and RSS data. The internal structure within this feature is reproducible at different azimuths (and different widths) on a scale of ~4 km, and appears the same at ultraviolet and radio wavelengths. These characteristics are similar to those of the Uranian ε ring which has a mass of 5×10^{18} gm and $\sum = 25$ cm^2/gm (Goldreich and Tremaine 1979b), a radial width varying from 20-100 km, a positive linear eccentricity gradient, free precession in Uranus' gravity field and reproducible internal structure on a scale of ~ 3 km (Nicholson et al. 1978; Nicholson et al. 1982).

The Titan ring is the only major eccentric narrow ring of either the Saturnian or Uranian ring systems which appears to be entirely forced by the perturbations of a distant satellite. The angular difference between the ring's apoapse and the direction to Titan is $-13° \pm 5°$. Though the magnitude of this number is not significant on the 3σ level, the sign implies that the ring is leading Titan in rotation. This is the anticipated result for a self-gravitating ring in which orbital energy is being dissipated through collisions. However, this result may also imply that the ring has a small component of free eccentricity and is librating in the reference frame of Titan.

Equation (6) in Chapter II is the relation between the (forced) eccentricity of the periodic orbits in a ring in terms of Δa, the distance of the ring from the resonance location, and other known quantities. For the Titan ring, this relation is:

$$e_{per} = \frac{M_{\text{Titan}} a^2 H_{11}}{M_p a_{\text{Titan}} \Delta a} \left[\frac{21}{2} J_2 \left(\frac{R_p}{a} \right)^2 - \frac{165}{4} J_4 \left(\frac{R_p}{a} \right)^4 \right]^{-1} , \tag{3}$$

with

$$H_{11} = \left[\alpha \frac{d b_{1/2}^{(1)}}{d\alpha} - 3\alpha + 2 b_{1/2}^{(1)} \right] . \tag{4}$$

For a librating ring, the semimajor axis and forced eccentricity of the ring vary periodically. However, the magnitude of the forced eccentricity is always uniquely related to Δa by (3). The possibility of free eccentricity in the Titan ring will be investigated in the future. At present we assume that its eccentricity is entirely forced. Subject to this assumption, Δa may be calculated using (3) and the measured values of a and e: $\Delta a = 19 \pm 2$ km. Using the zonal harmonics of Saturn's gravity field given by Null et al. (1981), $\Delta a = 75$ km; the error is large, of order 50-100 km. It is undoubtedly greater than the error in Δa found using the ring's measured eccentricity. Thus the analysis of this feature, in principle, provides a precise linear relation among J_2, J_4, and J_6 which constrains the gravity coefficients obtained from the combination of Pioneer gravity data and satellite secular rates. [In particular, it provides a better constraint on J_4 (with J_6 assumed) because the Titan ring is closer to Saturn than the closest approach distance of Pioneer 11, 1.35 R_s.] This relation will be given at a later date when an estimate of the maximum free eccentricity that can be accommodated by the data has been made. At present our model-dependent value for the location of the Titan 1:0 apsidal resonance is $a_{res} = 77852 \pm 9$ km. The error includes the systematic uncertainty in the absolute radius scale of ± 6 km.

In many respects, the 1.29 R_s Saturnian ring resembles the Huygens and Uranian ε rings. Though narrower than these rings (its model width varies from 13-38 km), its mass and $\sum$ are comparable: $M_r = 2.1 \times 10^{18}$ gm; $\sum = 17$ gm/cm^2. The PPS profile reveals sharp edges on a scale of ~ 1 km and a normal optical depth $\tau \sim 1.8$. It is embedded in a 184 km gap essentially devoid of material ($\tau < 0.05$).

The PPS profile of the Maxwell ring also exhibits sharp edges, a normal optical $\tau \sim 1.8$, and $\tau < 0.05$ for the Maxwell gap. However, this feature is kinematically different than any of the known narrow eccentric rings. At the present time the most plausible model involves the linear superposition of two components. The major component is a Keplerian ellipse precessing predominantly under the influence of Saturn's multipole moments. The other is, like the outer B ring edge, a Saturn-centered ellipse with a pattern speed and orientation expected for a ring whose eccentricity is forced by Mimas and the elliptical outer B ring. However, the residuals are large enough to suggest that important dynamical effects may be yet unaccounted for in the current model. These will be investigated in future work on this ring. The width-radius relation is unlike those of the Titan and Huygens rings and confirms the uniqueness of this feature among Saturn's ringlets.

It is known that the mass in the outer B ring will induce a perturbation, $\dot{\tilde{\omega}}_B$, on the precession rate of orbits in the Maxwell ring which can be related to $\sum_B$. Though the solution for $\dot{\tilde{\omega}}$ falls within the formal uncertainties of the value expected for free precession in Saturn's field, $\dot{\tilde{\omega}}_p$, it is possible that the large difference $\Delta\dot{\tilde{\omega}} = \dot{\tilde{\omega}} - \dot{\tilde{\omega}}_p = 0^\circ.1$ day^{-1}, is attributable to this effect and could be used to estimate $\sum_B$. Verification of this assertion must await a more precise model solution for $\dot{\tilde{\omega}}$: the current uncertainties are $O(\Delta\dot{\tilde{\omega}})$ and can provide only a crude upper limit to $\sum_B$. An independent estimate of $\sum_B$ may be obtained from the shape of the B ring edge and more precise versions of the conditions for non-precessing streamlines in the outer B ring (see Borderies et al. 1982; Section 4, Chapter II).

It has been suggested that small shepherding satellites may confine a narrow ring of material and in some cases excite and maintain the eccentricities of the ring particles (Goldreich and Tremaine 1979a). This mechanism was proposed to explain the narrow Uranian rings and was observationally verified by the Voyager discovery of the F ring shepherds. A natural consequence of the shepherding interaction is a high optical depth ring ($\tau \gtrsim 0.5$) embedded in a low optical depth region. This is the observed configuration for the Uranian and Saturnian ringlets. It is possible that the Titan, Huygens, and Maxwell ringlets owe their existences to small shepherding satellites orbiting within each gap.

The dimensions of these gaps are given in Table IIId. The radii of the inner and outer gap edges, which are circular to within measurement errors, are listed in rows 7 and 8, respectively. An upper limit on the eccentricity of each edge, e_{up}, is listed in brackets below its radius, with the exception of the Titan gap inner edge. The optical depth of the ring material at this edge is low (Plate 3). Consequently, radius measurements were too scanty to permit an estimate of e_{up}.

Forcing by Titan is expected to produce an eccentricity of $\sim 1 \times 10^{-4}$ in the outer Titan gap edge. We estimate $e_{up} = 8 \times 10^{-5}$. It is possible that detailed analysis of this edge will yield a measured eccentricity. This matter will be investigated in the future.

The semimajor axis of the ringlet's inner edge is given by $a_i = a - \delta a/2$. Comparison of this value with the gap center reveals that in each case the ringlet is situated in the outer half of its gap. [Note in particular that a_i(Titan) = 77859 ± 2 km. Considering the uncertainties, this position is identical to the 1:0 apsidal resonance location found from this work, a_{res} = 77852 ± 9 km]. The maximum radial extent of the ringlet's outer edge is given by:

$$r_{\max} = a + \delta a/2 + (a + \delta a/2)(e + \delta e/2) \quad . \tag{5}$$

The Titan, Huygens, and Maxwell rings come within 10 ± 4, 21 ± 5, and ~ 80 km, respectively, of the outer gap edges. [We can say from these results that the outer edge of the Huygens ring never touches the outer edge of the Huygens gap, in contrast to the statements made by Esposito et al. (1983a)].

In the C ring, where typically $\tau \lesssim 0.5$ and the viscous stresses are likely to be small, a satellite of radius r_{sat} (km) and density $\rho \sim 1$ gm/cm^3 can open and maintain a gap of width W_{gap} (km) $\sim (r_{sat})^2$. For the Titan and Huygens rings, it is possible that satellites a few kilometers in radius are maintaining the separation between ring and outer gap edge. The Maxwell ring presents a special case in this regard: there is a very narrow (~ 2 km wide) ringlet situated ~ 20 km inside the outer Maxwell gap edge. (This feature was not considered a major ringlet and was not studied here.) Presumably this tiny ringlet is also shepherded by satellites which are maintaining the ring's position relative to the gap edge. There is no need, therefore, to invoke a satellite 10 km in radius to maintain the 80 km outer Maxwell gap. A systematic search for embedded satellites in the Cassini division (of which the Maxwell gap is a part) yielded negative results. An upper limit of $r_{sat} \sim 6$ km was placed on any shepherding bodies in this division of albedo = 0.3 and $\rho = 1$ (Smith et al. 1982).

The origin of the gaps in which the ringlets lie remains a puzzle. The Mimas 2:1 resonance is the strongest in the entire ring system and has been held responsible for the Cassini division (Goldreich and Tremaine, 1978). The Titan 1:0 apsidal resonance is the strongest in the C ring. It is reasonable to suggest that it is responsible for the Titan gap. The Huygens gap, however, is not associated with any strong resonances. Evidently, resonances are not necessary for the clearing of gaps: the Encke gap at 2.21 R_s, among others, is not associated with any resonances. However there is indirect evidence of shepherding satellites in the Encke gap (Cuzzi and Scargle 1983). It is possible that the clearing of a gap by either strong resonances or small embedded satellites may leave behind ring particles large enough to shepherd the material between their orbits into a narrow ring.

The eccentricities of the Huygens, Maxwell, and F rings may well be maintained by shepherding bodies. From the work presented here, it appears that the eccentricity of the 1.29 R_s ring is predominantly if not completely forced by Titan. The dynamical interaction between a shepherd and a narrow confined ring may be complex; the orbits of both may evolve through this interaction (Goldreich and Tremaine, 1981). If shepherding bodies are confining the Titan ring, it is likely that their orbital motions have also fallen under the dominating influence of Titan.

The close passage of a shepherding body may induce perturbations in nearby ring particle orbits which take the form of radial variations or waves. Based on the arguments presented above it appears worthwhile to search for a wave pattern in the outer edges of these ringlets and/or the outer edges of the gaps in which they lie. Such an observation would lend credence to the hypothesis of shepherding satellites in explaining the existence of the narrow Saturnian rings.

It is illuminating to compare κ's deduced for different ring locations. Values have been inferred for a few local regions in the A and B rings and the Cassini division from the analysis of spiral density and bending waves. These vary from $\kappa \sim$ 0.4–2.1 × 10^{-2} cm^2/gm (Esposito et al. 1983b) and are ~5-20 times smaller than those obtained here for the Titan and Huygens rings. [The only previously reported value of specific opacity in the C ring, $\kappa = 0.05$ cm^2/gm, was obtained by Esposito et al. (1983a) for the Huygens ring in a manner virtually identical to that described here].

For a mono-dispersive particle size distribution with spherical particles of radius a_p and density ρ, $\kappa \sim 1/(\rho a_p)$ and a_p is a measure of the particle size in the ring. For a ring with a broad particle size distribution, it is untenable to assign a precise physical meaning to a_p. Nonetheless, the differing values of κ may imply a greater relative number of small particles in these C ringlets than that found in the A ring, the B ring or the Cassini division.

There is evidence that these ringlets differ significantly from the majority of the C ring as well. The τ_{UVS} and τ_{PPS} of the Titan and Huygens rings are among the highest in the entire C ring when examined at a resolution of ~5 km. The only other C ring region of $\tau \sim 2$ at this resolution is associated with the Mimas 3:1 resonance at 1.495 R_s (Lane et al. 1983). Optical depths throughout the remainder of the C ring are $\lesssim 0.5$. In addition, it is found from preliminary comparisons of Voyager observations made in the ultraviolet, visible, infrared, and radio that most of the C ring is apparently devoid of particles of millimeter size and smaller (Esposito et al. 1983b). In comparing τ_{UVS} and τ_{RSS} of the Huygens ring, Esposito et al. (1983a) infer that ~1/2 of the cross-sectional area of the ring is due to particles with typical radii < 1 cm. The greater optical depths and greater relative number of small particles in the Huygens and (presumably) Titan rings, compared to other C ring locations, are consistent with the expected association of increased collision frequency and small-particle production in regions of high τ. These results may imply that high τ's and high small-particle concentrations, which are not representative of the C ring, are being produced in these features by either resonances or the confining of material by shepherding satellites.

5. Conclusions

1. The Titan and Huygens rings at 1.29 and 1.45 R_s are the Saturnian analogs of the α, β, and ε rings of Uranus. The following structural characteristics may be compared:
   - i. narrow and eccentric: e(Titan, Huygens, α, β) $\sim$ 3-6 $\times$ 10^{-4}; $e(\varepsilon) \sim 8 \times 10^{-3}$; $\overline{W} \sim$ 10-60 km.
   - ii. sharp edges on scale of $\sim$ 1 km (ε, Titan, Huygens).
   - iii. normal optical depths $\tau \sim$ 0.5–2.0 (all).
   - iv. normal optical depth of surrounding region $\tau \lesssim$ 0.05 (all).
   - v. positive linear width-radius relations (all).
   - vi. $\sum \sim$ 20 gm/cm^2 (ε, Titan, Huygens).
2. The Titan ring is the only feature whose dynamics appear to be completely determined by an external satellite. A determination of the location of the Titan 1:0 apsidal resonance, more precise than that obtained using Saturn's gravity coefficients, has been made: 77852 ± 9 km. To within the model errors, the semimajor axis of the ringlet inner edge coincides with this resonance position.
3. There is some evidence of an angular separation between the Titan ring's apsidal line and the direction to Titan. This may

be a manifestation of viscous effects in the ring or a small-amplitude libration around the Titan-Saturn line. Neither possibility can be excluded on the basis of the present analysis.

4. The kinematics of the Huygens ring are determined solely by Saturn's non-spherical gravity field.

5. The amplitudes of the radial variations of these two rings are:

$$ae\,(1.29\ R_s) = 20 \pm 2\ \mathrm{km}$$

$$ae\,(1.45\ R_s) = 30 \pm 4\ \mathrm{km}$$

   The outer edges of the 1.29 and 1.45 R_s rings come within 10 ± 4 and 21 ± 5, respectively, of their gaps' outer edges.

6. The comparatively large measured optical depths and large inferred specific opacities for the Titan and Huygens rings suggest an environment and particle-size distribution different from the remainder of the C ring and presumably caused by the mechanism responsible for ring confinement.

7. The Maxwell ring at 1.95 R_s shares with the other eccentric rings the first 4 characteristics mentioned in 1). However, the radius-longitude and width-radius observations of this ring are inconsistent with its being kinematically identical to the Titan, Huygens, or Uranian (α, β, ε) rings. The current best-fit model suggests that the ring particle orbits are being perturbed by Mimas and the B ring. Further analysis of this

feature may provide an estimate of the surface mass density in the outer B ring.

References

Borderies, N., Goldreich, P., and Tremaine, S. (1983). *Icarus*, submitted.

Cuzzi, J.N. and Scargle, J. (1983). In preparation.

Esposito, L.W., et al. (1983a). *Science*, submitted.

Esposito, L.W., Cuzzi, J.N., Evans, D.R., Holberg, J.B., Marouf, E.A., Tyler, G.L., and Porco, C.C. (1983b). In *Saturn*, T. Gehrels (ed.), University of Arizona Press, Tucson.

Goldreich, P. and Tremaine, S. (1978). *Icarus* **34**, 240.

Goldreich, P. and Tremaine, S. (1979a). *Nature* **277**, 97.

Goldreich, P. and Tremaine, S. (1979b). *Astron. J.* **84**, 1638.

Goldreich, P. and Tremaine, S. (1981). *Ap. J.* **243**, 1062.

Lane, A.L., Graps, A.L., and Simmons, K.A. (1983). In *Proceedings of IAU Colloquium No. 75, Planetary Rings*, A. Brahic (ed.), CNES, Toulouse. In press.

Nicholson, P.D., Persson, S.E., Matthews, K., Goldreich, P., and Neugebauer, G. (1978). *Astron. J.* **83**, 1240.

Nicholson, P.D., Matthews, K., and Goldreich, P. (1982). *Astron. J.* **87**, 433.

Null, G.W., Lau, E.L., Biller, E.D., and Anderson, J.D. (1981). *Astron. J.* **86**, 456.

Smith, B.A., et al. (1981). *Science* **212**, 163.

Smith, B.A., et al. (1982). *Science* **215**, 504.

PART 2

THE PERIODIC VARIATION OF SPOKES

Preface

The spokes in Saturn's rings were perhaps Voyager's most mystifying discovery and still elude understanding. Part 2 of this dissertation is an investigation of the long-term kinematics of these features. In Chapter IV, a summary of the spoke studies made to date is given and the results of these studies are placed in context with the results presented here. Chapter V is a published paper written in collaboration with G.E. Danielson [(1982), *Astron. J.* **87**, 826]. It reports on the discovery of a periodicity in the variation of spoke activity on the morning ansa of Saturn's rings as observed in Voyager 1 images and the correlation of this activity with the sector of Saturn's magnetic field responsible for the most intense emission of the Saturn Kilometric Radiation (SKR). The sixth and final chapter, a collaboration with G.E. Danielson and V. Haemmerle, details the results of extending the analysis of Chapter V to include Voyager 2 data.

Chapter IV. A Summary of Spoke Observations

There is still doubt concerning the first detection of spokes. Claims have been made in the past of observations of spoke-like markings on the rings but none seem to fit the precise description of these features as we now know them. Between 1887 and 1955, at least six independent observations of radial and/or triangular-shaped features projecting from the outer Cassini division into the A ring were reported (Beck and Koppmann 1982; Alexander 1962). These include remarkably similar drawings made by E.M. Antoniadi in 1896 and by P. Stroobandt in 1923. G. Ruggieri in 1955 noted clear (as opposed to dark) radial streaks in the A ring but attributed all previous findings plus his own to optical illusion. The most recent claims of visual detection of spokes and the only ground-based report of such features in the B ring were made by S. O'Meara (1982). His observations were made between the years 1976 and 1978 using a 23 cm telescope in twilight (to avoid glare from the rings) and included time-invariant dark 'bridges' seen with equal prominence on both ansae of the A ring and 'spikes' in the B ring, prominent only on the morning ansa and variable in visibility with a period approximately equal to Saturn's rotation period. The lack of apparent motion of the A ring bridges in O'Meara's observations leads one to agree with Ruggieri and O'Meara in suspecting that these features may indeed be an illusion and one, in fact, connected with the inherent azimuthal variation in brightness of the A ring. No ground-based photographic or photoelectric detection has yet been made of any spoke-like features in the A or B ring.

As seen by the Voyager cameras at low phase angles, the spokes appear as dark features against the bright rings (Fig. 1, chapter V) but their distribution in radius is strictly confined to the outer half of the B ring. They have been seen up to, but never past, the outer B ring edge at a radius of 117580 km and extend inwards to ~ 100000 km. Spokes of all contrasts (from the limit of detectability up to the maximum of 25%) may extend the entire length of this region (which includes the radius at which orbital motion equals the angular velocity of the magnetic field), and are typically 2000 to 5000 km wide. However, short wispy spokes (as appear in Plate 4) are almost always of low contrast and are generally seen in the outer part only. All spokes are roughly radial or sheared away from radial in the trailing direction. A qualitative search was conducted for spoke-like markings on both the illuminated and unilluminated sides of the A ring as seen in the frames comprising the Voyager 2 inbound (110 km/pix) and outbound (300 km/pix) movies. This search yielded negative results.

Grun et al. (1983) distinguish three classes: 1) extended spokes, seen between 100000 km and the corotation radius at ~ 112000 km, which have diffuse edges and are slightly wedged shaped. Their widths at the base (towards Saturn) can be as great as 20000 km; 2) narrow spokes between 104000 and 116000 km having sharp edges, and typical lengths and widths of 6000 and 2000 km, respectively; and 3) filamentary spokes, outside 110000 km, which in general join with a wider spoke further in. They are typically 3000 km in length and 500 km wide.

The distribution of spokes in orbital longitude on the ring plane is difficult to quantify as it depends on their size, number and contrast. If we use an index which is the product of these three variables, called 'spoke activity', then it can be said that the distribution of activity in azimuth (at a fixed time) generally peaks on the morning ansa. The distribution in time at a fixed orbital longitude (Porco and Danielson 1982) exhibits a variable component with a period consistent with that inferred for Saturn's rotation period: 639.4 minutes. These findings provide the first demonstration of a relationship between the magnetic field and the spokes.

A spectacular contrast reversal was discovered after Voyager's closest approach to Saturn: viewed in a forward-scattering geometry the spokes appeared brighter than the background ring plane (Smith et al. 1981; Plate 4). This observation suggests that spokes are comprised of particles whose sizes are comparable to the wavelength of visible light so that their phase functions are dominated by a strong forward-scattering diffraction lobe. This interpretation is strengthened by the association of spokes with the most optically thick part of the rings which itself looks brighter in forward-scattered light (relative to the inner B and middle A rings), suggesting that the entire spoke region is one of enhanced concentration of small particles relative to other regions.

The presence of small particles raises the question: how high are they above the ring plane? The analysis of a Voyager image taken within ± 5 seconds of ring plane crossing yielded an upper limit of 80 kilometers (Grun et al. 1983). The actual value, however, is probably much less. For spoke particles to appear distinct from the other particles in the rings requires only that they behave as individual scatterers: for sub-micron particles scattering visible light, a particle diameter's separation is sufficient.

In detail, the B ring is a random array of narrow ringlets of varying optical brightness (Plate 4). Recent analysis (Cuzzi 1983) indicates that these ringlets are the result of albedo rather than optical depth variations. One of the most puzzling aspects of spokes is that they lie coherently across these regions for many thousands of kilometers. Whether spoke particles move across the B ring or are observed close to their points of initial elevation has not yet been demonstrated. However, the latter seems much more plausible. Smith et al. (1982) observed a narrow radial spoke grow to a length of 6000 km in less than 5 minutes. If the spokes are indeed the manifestation of a discharge phenomenon which proceeds along the length of a spoke then this formation time implies a minimum disturbance speed of 2×10^6 cm/sec, much greater than any expected mechanical propagation speed for the rings: e.g., the velocity dispersion of the larger ring particles is $\lesssim 0.5$ cm/sec.

Knowledge of the ways in which spokes evolve with time is obviously essential to understanding the mechanisms which determine their origin and decay. Initial analysis of Voyager 1 images of the morning ansa of the rings taken in sequence 30 minutes apart revealed that spokes were predominantly moving at Keplerian angular velocities (Fig. 1). Since the time of their discovery it was suspected that spokes formed as perfectly radial features. The discovery of a radially forming spoke in a sequence of Voyager 2 images supported this suspicion (Smith et al. 1982). Spokes have been observed to travel the entire circumference of the rings; yet no where on the ring plane, in either Voyager 1 or Voyager 2 frames, do spoke tilts approach that value expected for constant Keplerian motion over an entire orbit. This implies that either average individual particle motions over several hours or more can significantly depart from Keplerian or the recycling time of spoke particles in a single feature is less than one rotation (Porco and Danielson 1982). The spoke motion observed in the latter case is a phase speed.

Recent measurements have shed some light on this. In measuring the motions of two narrow forming spokes (including the one reported in Smith et

Fig. 1. Measurements taken from two sets of Voyager 1 images, each set consisting of three frames recorded 30 minutes apart. The angular velocity of spokes is plotted against radial distance. The angular velocity of the magnetic field and the variation of Keplerian motion with radius are indicated. [From Smith et al. (1981).]

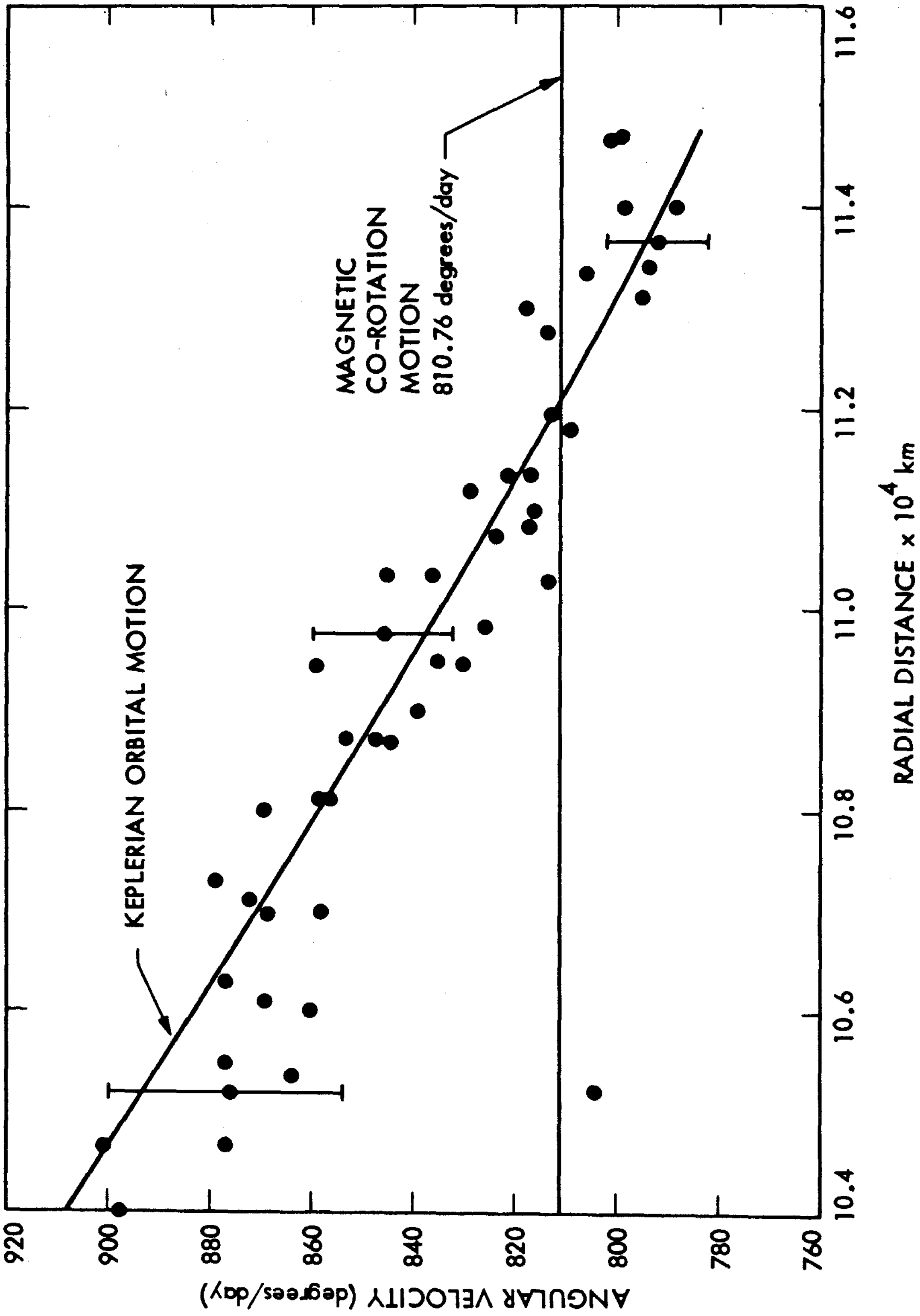
KEPLERIAN ORBITAL MOTION
MAGNETIC
CO-ROTATION
MOTION
810.76 degrees/day
ANGULAR VELOCITY (degrees/day)
920
900
880
860
840
820
800
780
760
RADIAL DISTANCE × 10^4 km
10.4
10.6
10.8
11.0
11.2
11.4
11.6

al. 1982), Grun et al. (1983) determined that inside the corotation point the trailing edges travel with the angular speed of the magnetic field, thereby remaining radial, while the leading edges move at Keplerian speeds. After formation, both edges tilt away from radial at the Keplerian rate. (Both edges of 'old' spokes measured in this study moved with Keplerian motion). The angle of the wedge produced by the differential motion between edges is taken to be a measure of the time during which the spoke was 'active.' Typical active times inferred from wedge-angle measurements of old spokes are one to three hours.

However, other recent measurements of spoke kinematics are apparently in conflict with these. Two different spokes were observed to form as diffuse features, grow in radius, darken, and move (both leading and trailing edges) with corotation motion for ~ 2 hours, after which their motions became Keplerian (Epplee and Smith 1983). All other non-forming spokes observed in this study also moved with Keplerian speeds.

In total, only 4 spokes have been observed to form. While it appears from these two analyses that the angular velocities of forming spokes can significantly differ from Keplerian, there is still some disagreement concerning the kinematics of formation. More measurements of this nature are necessary to clarify this important issue.

The question of where on the ring plane and where in the magnetic field individual spokes are most likely to form is related to the foregoing arguments and has only been partially addressed. Grun et al. (1983) have compiled frequency histograms of the orbital and magnetic longitudes at which old spokes, mapped backward in time under Keplerian motion, would have appeared perfectly radial. They studied morning ansa spokes only and found that the distribution in orbital longitude peaks ~2 hours out of the shadow, and that the distribution in magnetic longitude is slightly peaked in the SKR-active sector. The latter finding is consistent with that of Porco and Danielson (1982). The significance of the former will be in question until a) the same measurements are made on evening ansa spokes and b) the kinematics of spoke formation is understood.

Spokes were also seen on the unilluminated side of the rings by the Voyager 2 cameras. They presumably extend below the ring plane and are illuminated by light from the disc of Saturn which is scattered off the ring plane through phase angles of 80°-120° (Smith et al. 1982). It was concluded from the small degree of shear in these features and the assumption of continual Keplerian motion that they were not spokes which had passed through the ring plane one-half an orbital period after their creation on the illuminated side of the rings. However, if spoke velocities differ from Keplerian for a time as long as that suggested by the measurements of Epplee and Smith (1983), then this conclusion may be incorrect. Further analysis is required to determine the origin of the dark-side spokes.

References

Alexander, A.F. (1962). *The Planet Saturn*, Faber and Faber, London.

Beck, R. and Koppmann, R. (1982). *Spaceflight* **24**, 85.

Cuzzi, J.N. (1983). In *Proceedings of IAU Colloquium, No. 75, Planetary Rings*, A. Brahic, ed., CNES, Toulouse, in press.

Epplee, R.E. and Smith, B.A. (1983). In *Proceedings of IAU Colloquium, No. 75, Planetary Rings*, A. Brahic, ed., CNES, Toulouse, in press.

Grun, E., Morfill, G.E., Terrile, R.J., Johnson, T.V., and Scwehm, G. (1983). *Icarus*, submitted.

O'Meara, S. (1982). Presentation at Saturn Conference, Tucson, Arizona.

Porco, C.C. and Danielson, G.E. (1982). *Astron. J.* **87**, 826.

Smith B.A. et al. (1981). *Science* **212**, 163.

Smith, B.A. et al. (1982). *Science* **215**, 504.

Chapter V. The Periodic Variation of Spokes in Saturn's Rings

Carolyn C. Porco and G. Edward Danielson

Division of Geological and Planetary Sciences
California Institute of Technology
Pasadena, California 91125

Contribution No. 3725 of the Division of Geological and Planetary Sciences, California Institute of Technology, Pasadena, California 91125.

Published *Astronomical Journal* **87**, 826-833, 1982

ABSTRACT

The discovery of a periodic variation in spoke activity in Saturn's rings from the analysis of *Voyager* images is reported. A Fourier power spectrum was computed using a data set generated by quantifying spoke activity observed on the morning (western) half of the rings in *Voyager* images spanning 5.5 (~ 12 Saturn rotations). A peak ~ 14σ above the noise in the frequency domain was found at a period of 621 ± 22 min. Within the formal error, this value is consistent with the 639.4-min rotation period of Saturn's magnetic field. Maximum spoke activity is most likely to be observed on the morning half of the rings when a particular magnetic field sector coincides with this area. This magnetic sector contains the region which is aligned with local noon at the time of the emission of the SKR (Saturn Kilometric Radiation). These results suggest that the fundamental period of spoke variation is that of Saturn's magnetic field, and that spoke activity is associated with the region of the field which gives rise to the SKR. Passage of this region through Saturn's shadow may play a significant role in the creation and/or rejuvenation of spokes.

INTRODUCTION

Thirty-seven days before closest approach to Saturn, the *Voyager 1* Imaging Science experiment team discovered radial features on Saturn's B ring. These features, which came to be called "spokes," are described in a paper by Smith *et al.* (1981) devoted to the *Voyager 1* Saturn encounter. Mentioned in that paper, and of particular importance to the study here, are the following:

1. Observations of spokes taken over widely varying phase angles indicate the presence of micron-sized particles which are possibly elevated above the ring plane.

2. Spokes are typically 10,000-20,000 km in length and extend over a region of the B ring which includes the point at which Keplerian motion matches the motion of the magnetic field.
3. By tracking spoke features from image to image, it was determined that over time scales of order 30 min spokes move predominantly at Keplerian angular velocities and not with the angular velocity of the magnetic field.
4. The majority of spokes are sheared away from radial in the trailing sense. When mapped backward in time under Keplerian motion to Saturn's shadow on the ring plane, spokes are parallel to neither the morning nor the evening edge.
5. Spokes are observed most commonly and with greatest contrast on the west (morning) ansa.

Also of importance are the discoveries by the Planetary Radio Astronomy (PRA) experiment of (Warwick *et al.* 1981) of very broadband electrostatic discharges (SED) believed to arise on the ring plane, and of a strong source of kilometric wavelength radiation (SKR). Analysis of the SED by Evans *et al.* (1981) confirmed the periodic nature of these emissions which occur over at least one-half of the orbit of a system rotating around Saturn with a period of 611 ± 5 min. From the statistical properties of the SKR and from a reasonable source model, Kaiser, Desch, and Lecacheux (1981) were able to constrain the possible locations of these long-wavelength emissions. They favor a source which is confined to high magnetic latitudes ($\varphi_{SLS} > 60°$) and begins emitting most intensely when magnetic longitude $\lambda_{SLS} = 100°$ coincides with the noon meridian. (The magnetic longitude system used here is the Saturn Longitude System, SLS, defined by Desch and Kaiser 1981.) An association with a dayside polar cusp in Saturn's magnetosphere is suggested. In addition, from data acquired by the *Voyager 1* Ultraviolet Spectrometer, Sandel and Broadfoot (1981) found a reasonable correlation between the SKR emission probability and the intensity of Saturn's northern aurora when the two phenomena were compared in a system defined by the SLS longitude of the Sun at the time of emission.

The present work describes the beginnings of an analysis of *Voyager* imaging data for the purposes of investigating the kinematics of spokes and their relationship, if any, to observed magnetic phenomena within the Saturn system. The data and methods of reduction used for this study are outlined. It is found from *Voyager 1* data that the variation of spoke activity on the ring plane at a fixed solar longitude (i.e., relative to the subsolar point) is periodic in time. A preliminary analysis of *Voyager 2* imaging data supports this result. Furthermore, maximum spoke activity is most likely to occur within a range of magnetic longitudes (herein referred to as the "spoke-active" sector) which coincides with that region of Saturn's field which is aligned with local noon at the time of the SKR emission (herein referred to as the "SKR-active" sector). The implications of these findings are discussed.

DATA DESCRIPTION

The data used for this analysis fall into three separate groups:

1. *Voyager 1 inbound ring movie frames.* These were taken

every 288 s for a period of ~ 10 hr on day 299 of 1980 with the *Voyager 1* narrow-angle camera through the clear filter (Smith *et al.* 1977) at a range of 25,000,000 km. The resolution obtained was 230 km/pixel. The spacecraft angle above the ring plane was ~ 9° and the phase angle was ~ 13°. In these images, as for all images used in this study, the spokes appear dark. Only the morning ansa of Saturn was imaged, giving a total azimuthal coverage of the ring plane of ~ 100° per frame.

2. *Voyager 1 intermediate frames.* Between the *Voyager 1* inbound movie and closest approach, the *Voyager* cameras repeatedly took a series of exposures. Once in every series an image of the western half of the ring system was obtained in the blue filter with the narrow-angle camera. The best of these images, those for which the pointing was accurate, comprise the *Voyager 1* intermediate data set. This set covers ~ 5.5 days (~ 12 Saturn field rotations), starting at day 303 of 1980. As for the inbound movie, the phase angle was ~ 13° and the subspacecraft latitude was ~ 9°. The resolution for these frames was ~ 180 km/pixel.

3. *Voyager 2 frames.* These frames were taken between day 177 and 198 of 1981 with the *Voyager 2* narrow-angle camera through a clear filter. The resolution ranges from 354 to 532 km/pixel. The spacecraft latitude and phase angles were 10° and 7°, respectively.

DATA REDUCTION AND ANALYSIS

a) Intermediate Data Set

To investigate long-term spoke motion, the *Voyager 1* intermediate frames were used. (*Voyager 2* frames were reduced in an identical way but the detailed analysis of these images is not yet complete.) The interval between these frames was typically 2 hr or more, corresponding to ~ 70° of rotation in the "spoke region" of the B ring. Therefore no attempt was made to follow or weight individual spokes. Instead, a judgment was made by eye of the total amount of spoke activity within an arc of ~ 40° centered on the semimajor axis of the western ansa of each image.

The spoke activity thus measured was binned into four categories based on the following criteria (Fig. 1):

1. *Category 1 (least activity)*: few if any distinct, low-contrast spokes. Diffuse background activity (defined to be that which often appears in a region from ~ 103,000 to ~ 105,000 km) is sometimes evident at low contrast.
2. *Category 2 (intermediate low)*: generally one or two medium-contrast, distinct spokes and in some cases some medium-contrast background activity.
3. *Category 3 (intermediate high)*: in general, two high-contrast spokes, or alternatively, several medium-contrast spokes with medium- to high-contrast background activity.
4. *Category 4 (maximum activity)*: at least three very high-contrast, long spokes with or without background activity or,

Fig. 1. *Voyager 2* narrow-angle frames taken through the clear filter ($\lambda_{eff} = 4970$ Å) exemplifying the four spoke-activity categories. The resolution in these frames is ~500 km/pixel. The distinct black dots are part of the camera system and are not real.

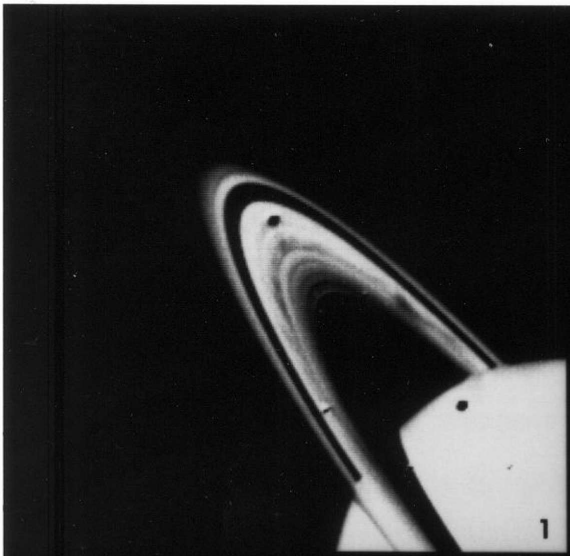

1

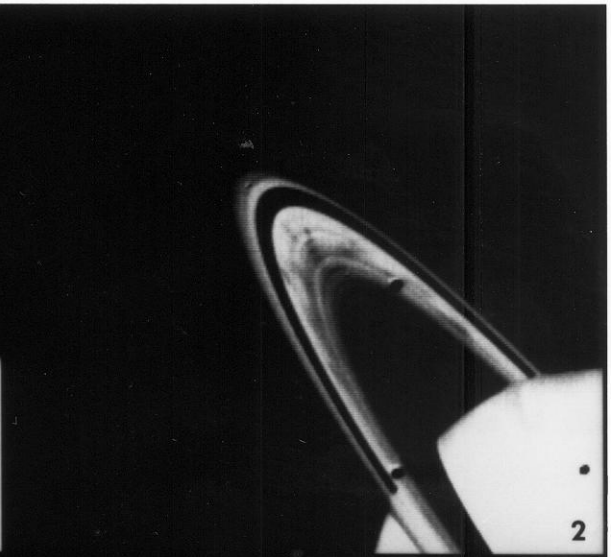

2

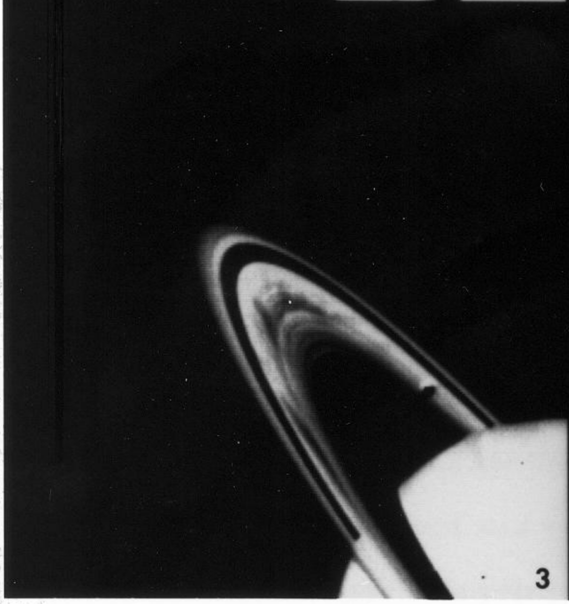

3

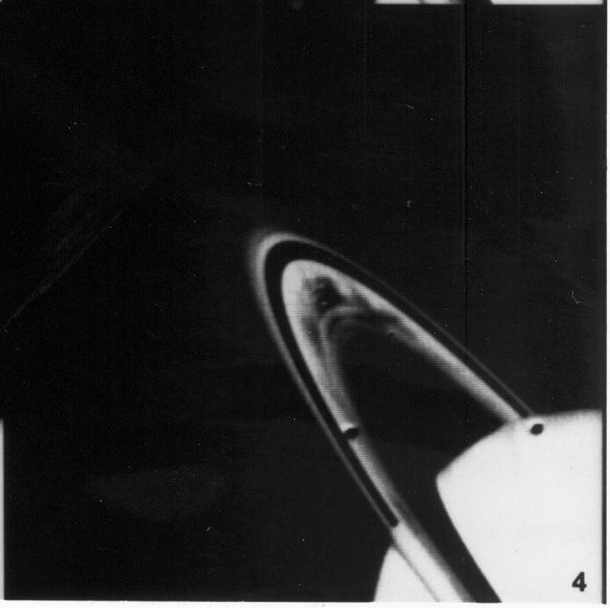

4

alternatively, one or more very wide and long dark blobs. Oftentimes, spokes in this category extend inward of the common spoke inner boundary at ~ 103,000 km.

The appearance of spokes is more varied than is accounted for by these criteria. Therefore, the descriptions given above must be considered typical but not strict representations of each category. A frame was placed into a particular category if the spoke activity within the 40° measurement "window," integrated over distinct and diffuse features, was approximately equal to the activity of the representative frame.

The function of this type of quantization represents is monotonic but not linear. In the analysis described below, no use is made of the amplitude of the variation in spoke activity.

The Fourier power spectrum of the intermediate data set was computed using periods ranging from 4000 to 250 min by employing a technique appropriate for unequally spaced data (Deeming 1975). The results are shown in Fig. 2. A pronounced feature can be seen near 625 min. This feature is ~ 4 times stronger than the next highest peak at 735 min and is ~ 14σ above the noise. To determine the period more accurately, a value of 625 min was used as a first-guess input parameter to a non-linear least-squares routine that fitted a sinusoid to the data. The amplitude of the sinusoid was held fixed while the phase and the period were allowed to vary. This procedure determined the phase and period at which the residuals for the intermediate data set were minimized.

The uncertainty associated with this period was assessed in the following way. The categorization of spoke activity was done on a subset of

Fig. 2. The Fourier power spectrum of spoke activity observed on the morning ansa between days 303 and 309 of 1980. The ordinate is spectral power relative to σ, the standard deviation of the noise inherent in this analysis. The only significant peak occurs 14σ above the noise at a period of 621 min. The half-width at half-maximum is 22 mn.

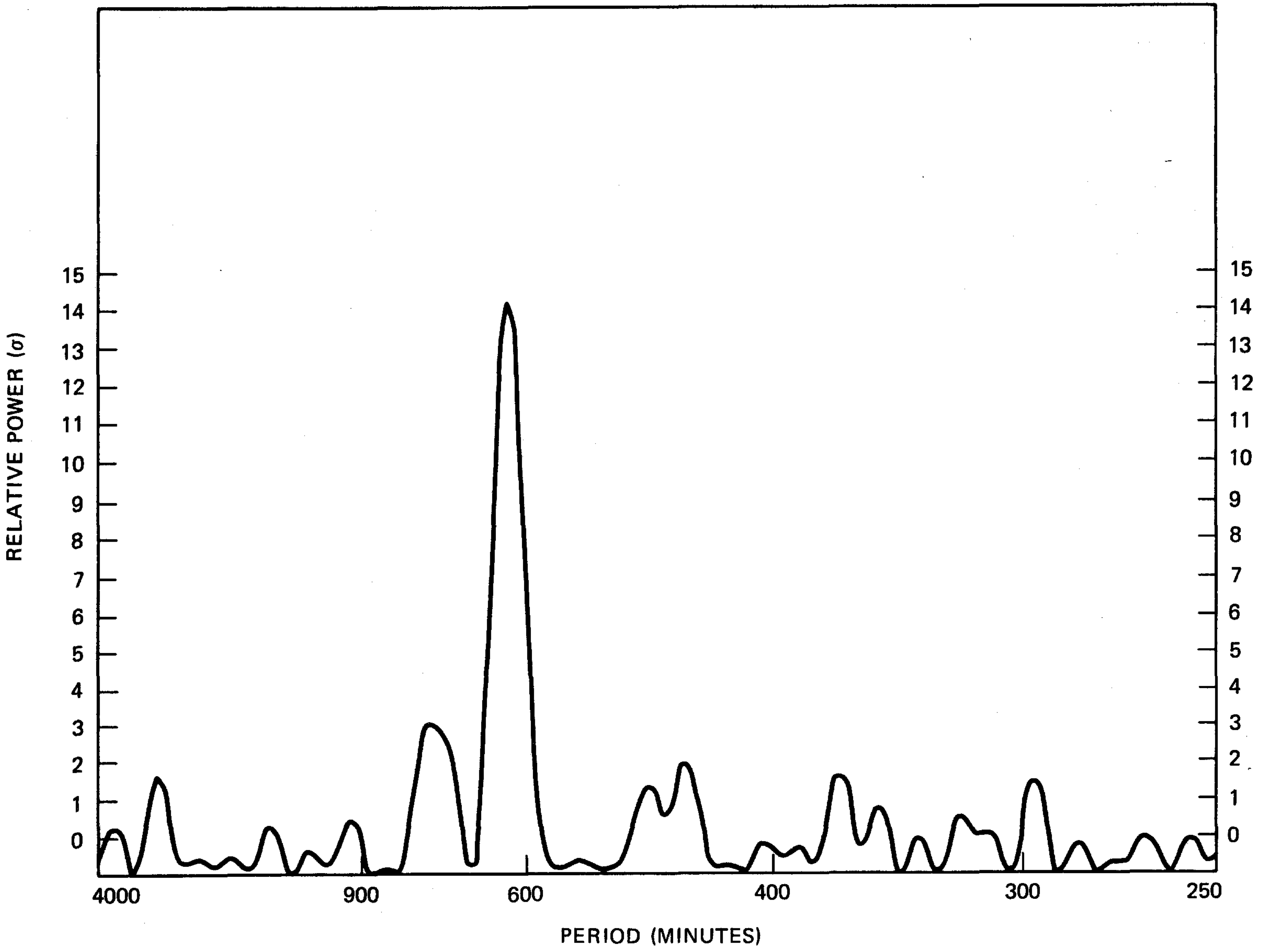
RELATIVE POWER (σ)
0
1
2
3
4
5
6
7
8
9
10
11
12
13
14
15
4000
900
600
400
300
250
PERIOD (MINUTES)

the data by several different observers and the standard deviation about the mean category for each frame used in these trials was computed. This deviation, 0.6 (where 1 = 1 category), is small, giving us confidence in the categorization procedure. Experiments were then run in which Gaussian noise with a 1-category standard deviation was added to the data; the power spectrum was again computed. The height of the spectral feature was degraded as would be expected from adding noise, but the rms displacement of the feature in these experiments, ± 8.5 min, was small in comparison with its width. This implies that measurement errors due to the rather subjective method of estimating spoke activity are not the dominant source of uncertainty. Therefore we take the half-width at half-maximum to be the uncertainty, and obtain a final value for the period of 621 ± 22 min.

b) Association of Magnetic Longitude with Spoke Activity

The proximity of this value to the rotational period of Saturn's magnetic field, 639.4 min (± 3 s), motivated a search for a preferred magnetic region of spoke activity. To this end, we chose the *Voyager 1* and *Voyager 2* frames which fell into categories 4 (highest activity) and 1 (lowest activity) and computed the SLS longitudes of the morning ansa at the (spacecraft event) times at which the frames were acquired. These longitudes were binned into magnetic quadrants and the resulting histograms are shown in Fig. 3.

Although the statistics from *Voyager 1* data are poor (there are only ten category-4 frames and 14 category-1 frames), there is a suggestion in Fig. 3(a) that high-contrast spokes occur within the magnetic quadrant which coincides with the SKR-active sector; the quadrant of least activity coincides with the SKR-

Fig. 3. Frequency distributions showing the number of frames (ordinate) in category 4 (greatest activity) and in category 1 (least activity) that fall within the SLS quadrants given on the abscissa. (a) *Voyager 1* results spanning ~ 12 Saturn rotations. (b) *Voyager 2* results spanning ~ 47 Saturn rotations.

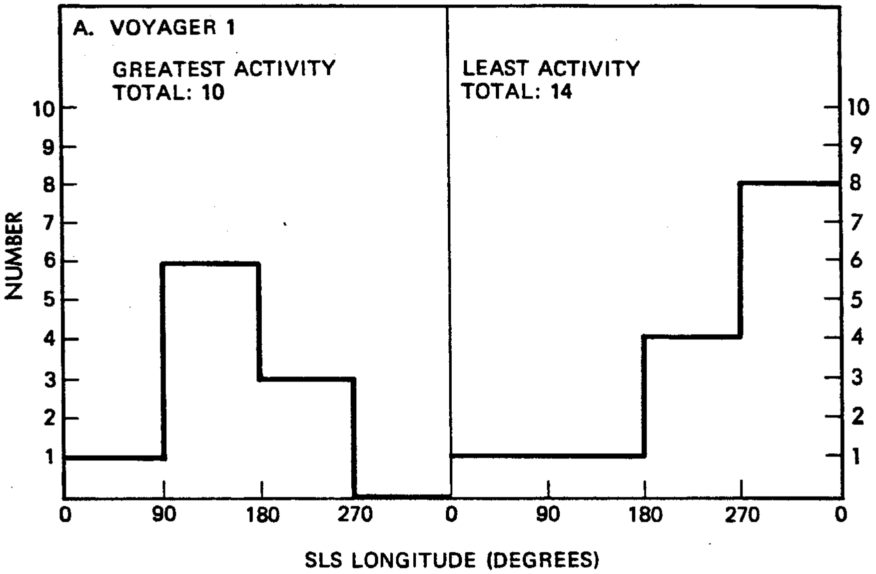
A. VOYAGER 1
GREATEST ACTIVITY
TOTAL: 10
LEAST ACTIVITY
TOTAL: 14
NUMBER
1
2
3
4
5
6
7
8
9
10
0
90
180
270
0
90
180
270
0
SLS LONGITUDE (DEGREES)

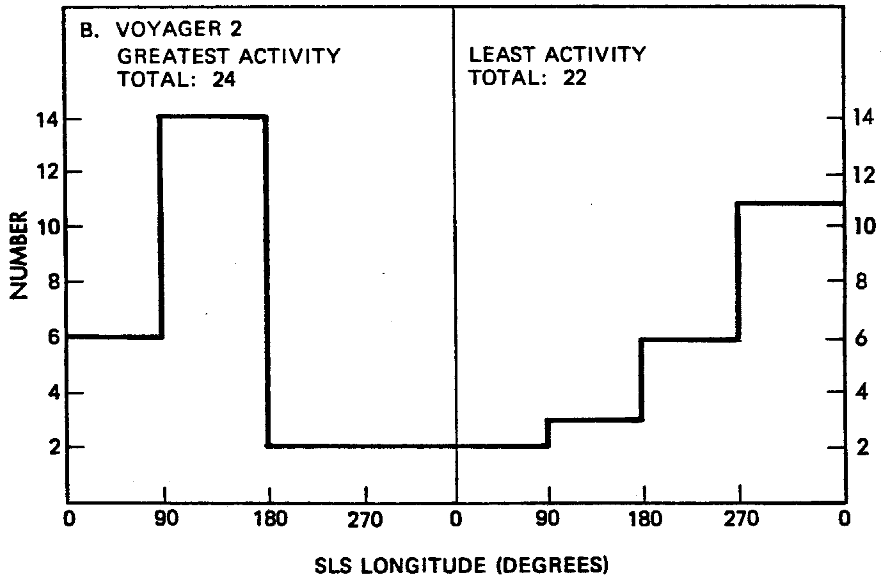
B. VOYAGER 2
GREATEST ACTIVITY
TOTAL: 24
LEAST ACTIVITY
TOTAL: 22
NUMBER
2
4
6
8
10
12
14
0
90
180
270
0
90
180
270
0
SLS LONGITUDE (DEGREES)

inactive sector (see Fig. 2 of Kaiser *et al.* 1981).

A similar analysis performed on 22 category-1 and 24 category-4 *Voyager 2* frames extending over 21 days (~47 rotations) yields similar results [Fig. 3(b)].

From data acquired by the *Voyager 2* PRA experiment, Kaiser and Desch (1982) have determined that the northern-hemisphere SKR source is centered at $\lambda_{SLS} = 115° \pm 15°$ and $\varphi_{SLS} = 76° \pm 4°$. Figure 4 shows the results of summing the *Voyager 1* and *Voyager 2* data, which span a total interval of 260 days (~586 Saturn rotations), dividing the abscissa into octants 45° wide, and centering the entire scale on $\lambda_{SLS} = 115°$. Also plotted in Fig. 4 are the 100-kHz occurrence rates of the SKR for the *Voyager 1* inbound observing position (taken from Fig. 2 of Kaiser *et al.* 1981). The correlation in both SLS longitude and distribution width between the spoke-active sector and the SKR-active sector is striking. The likelihood of observing a similar distribution of spoke activity from an equivalent-sized random sample of data in which no correlation exists has been computed using a chi-squared test to be < 0.5%.

[It must be noted that the current estimate of the formal error in the period of rotation of Saturn's field, ± 3 s, implies a possible accumulation of ± 35° uncertainty in magnetic longitude between the SLS epoch (1980.0) and the *Voyager 1* data analyzed here, and a possible relative uncertainty of ± 20° between *Voyager 1* and *Voyager 2*. However, the accepted value of the period remains unrevised at 639.4 min (Kaiser 1981, private communication).]

c) Inbound Movie

A study of the detailed variation in spoke activity on the morning ansa during one complete and fully sampled magnetic field rotation was made by

Fig. 4. Frequency distribution like those in Fig. 3, but showing the sum *Voyager 1* and *Voyager 2* results which span a total interval of ~ 586 Saturn rotations. The data are binned into octants 45° wide; the abscissa is centered on λ_{SLS} = 115°. Also shown are the ± 15° uncertainty in the location of the SKR source region and the 100-kHz SKR occurrence rates (dotted distribution) taken from Fig. 2 of Kaiser *et al.* (1981).

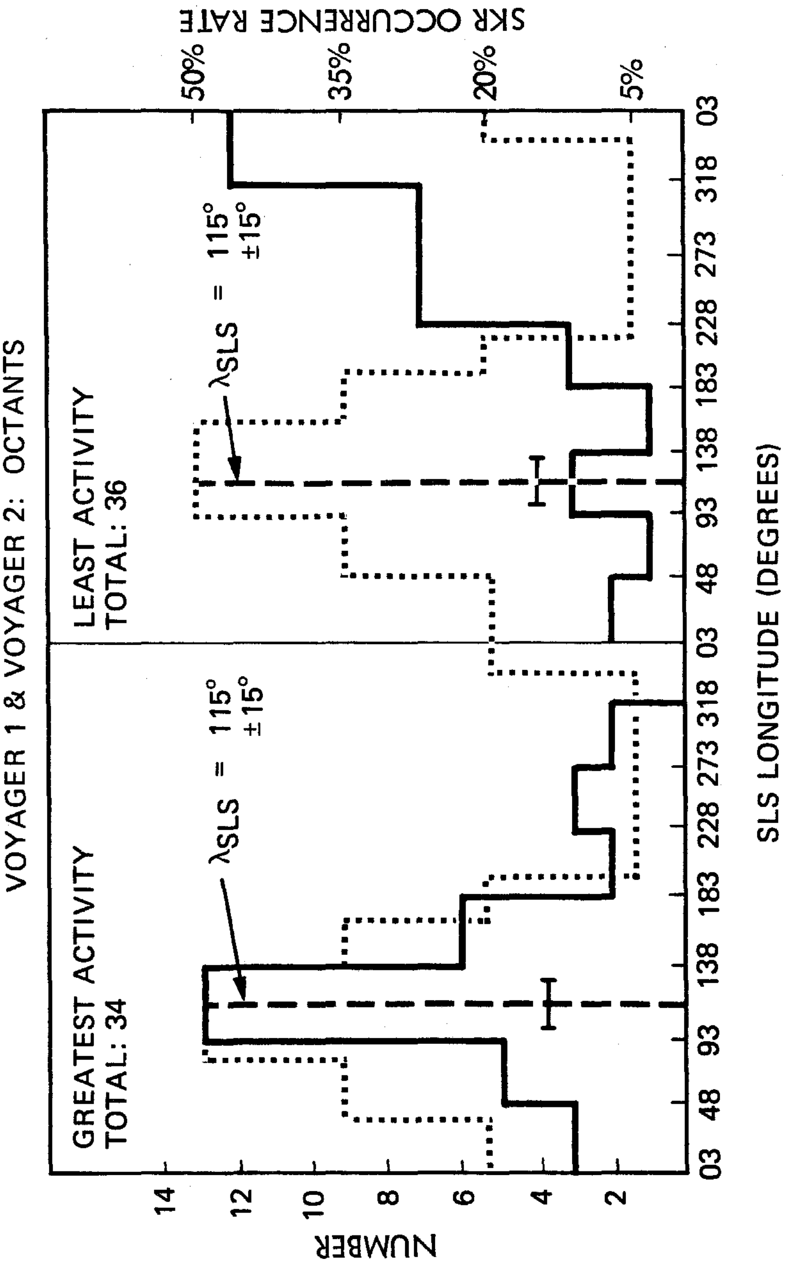
VOYAGER 1 & VOYAGER 2: OCTANTS
GREATEST ACTIVITY
TOTAL: 34
λSLS = 115°
±15°
LEAST ACTIVITY
TOTAL: 36
λSLS = 115°
±15°
NUMBER
14
12
10
8
6
4
2
SKR OCCURRENCE RATE
50%
35%
20%
5%
03
48
93
138
183
228
273
318
03
48
93
138
183
228
273
318
03
SLS LONGITUDE (DEGREES)

examining the frames from the *Voyager 1* inbound movie. These frames were reduced on an image-processing system at Caltech using a Vax 11/780 computer and an ellipse-fitting program specifically designed for the present study. Navigation parameters for each image were acquired from the Supplementary Experimental Data Record (SEDR) and were used to compute first-guess ellipse parameters. The difficult process of accurately determining these parameters from the SEDR in the case when only half or less of the ring system was imaged was made easier by constraining the semimajor axis. The absolute radius of a given ring feature was obtained independently (Diner 1981, private communication) and converted into pixels using the scale (km/pixel) given in the SEDR. This parameter was held constant while the others (center, axis ratio, and orientation in the frame) were adjusted. The ellipses were fitted to images of the rings to within a precision of $\sim \pm 1$ pixel in radius as determined by visual inspection. A longitude system fixed with respect to the Sun (i.e., approximately inertial) was projected on the ring plane and thus allowed the absolute coordinates of spokes to be measured. Spokes were followed from frame to frame; those passing a particular solar longitude on the morning ansa per unit time were counted and weighted by eye in proportion to their area and contrast. These weighted numbers were added, yielding a subjective but consistent measure of spoke activity for each time interval.

The data are shown in Fig. 5. The unit of time is 1 FDS (Flight Data Subsystem) count of 48 min. The height of each interval is proportional to spoke activity. We have computed the SLS longitude of the morning ansa at the central time of each interval; these longitudes are also shown in Fig. 5.

Observations of spoke activity spanning one rotation cannot be expected to yield results as statistically significant as those obtained from a data set

Fig. 5. The distribution of spoke activity on the morning ansa vs time for one complete Saturn rotation measured on *Voyager 1* inbound movie frames. The unit of time is 48 min; the height of each interval is proportional to spoke activity. Also shown above is the SLS longitude of the morning ansa at the central time of each interval.

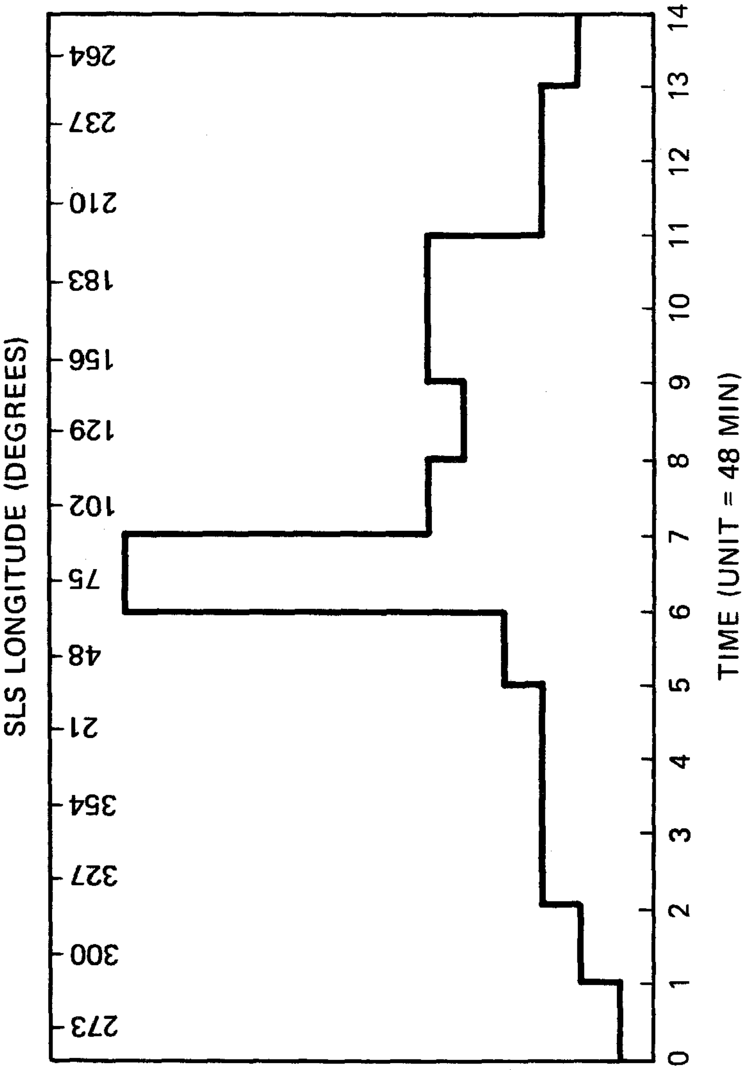
SLS LONGITUDE (DEGREES)
273
300
327
354
21
48
75
102
129
156
183
210
237
264
TIME (UNIT = 48 MIN)
0
1
2
3
4
5
6
7
8
9
10
11
12
13
14

spanning many rotations. Nonetheless, the general features of spoke variation discussed in the previous sections are apparent in Fig. 5. First, the occurrence of spoke activity is not random but exhibits a pronounced peak. In addition, it appears that the distribution of the intermediate activity lying under this peak is approximately centered in a magnetic region extending from ~ 50° to ~ 185°, indicating a tendency for spoke activity to occur within the SKR-active sector. These features will be investigated in greater detail by analyzing the *Voyager 2* inbound movies.

DISCUSSION

The excellent correlation of maximum and minimum spoke activity with specific magnetic longitudes over an interval of 586 rotations suggests that the fundamental period in the variation of spoke activity as defined here is that of Saturn's magnetic field, 639.4 min. The period derived from the power spectrum, 621 ± 22 min, is compatible with this result. Nonetheless, the center of the 14σ feature in the power spectrum, which can be located to a precision of ± 8.5 min (i.e., the 1σ uncertainty expected from the measurement errors alone), does not fall within ± 8.5 min of Saturn's rotation period. This discrepancy may be real and possibly caused by statistical fluctuations in the production of spokes. Alternatively, it might be the result of a process which causes drifts in the longitude of spoke activity but is not coherent over long time intervals. Both interpretations are consistent with the rather short length of the data string (~ 12 rotations) used for computation of the power spectrum and the broad width (~ 120°) of the spoke-active sector inferred from Figs. 4 and 5. Within this sector, time-dependent excursions in the longitude of maximum spoke activity over the short time interval spanned by the *Voyager 1* intermediate data set might account for the discrepancy between the measured and the fundamental period. However, on a time scale that is long compared to the duration of these excursions, the dominating influence on spoke activity would be the modulation due to Saturn's field. This implies that a power spectrum computed from a data string hundreds of rotations in length, therefore, would reveal a substantial peak centered very close to 639.4 min.

Note that the period derived from the power spectrum is also compatible with a number of other physically reasonable periods within the Saturn system. For example, the Keplerian orbits within Saturn's rings, corresponding to the range of periods represented by the ± 22-min uncertainty, extend from ~ 107,500 to ~ 112,700 km, well within the spoke region of the B ring. The period associated with the SED, 611 ± 5 min, also falls within this range. The possibility that spoke activity might on short time scales be related to the periodic phenomenon responsible for the SED, or to some other system orbiting Saturn within the spoke region, cannot be absolutely excluded on the basis of the limited available evidence. The issue of short-term variations in the period of spoke activity will hopefully be resolved by analysis of the long data set available from *Voyager 2*.

The observation that the spoke-active region coincides with the SKR-active region suggests a relationship between the two phenomena. However, the spoke region of Saturn's B ring, when mapped onto Saturn's field falls at magnetic latitudes 39°-45°, well below the 72°-80° auroral region of the SKR emission. In addition, SKR emission is Sun locked, occurring when the SKR-active sector begins to align itself with local noon. The observation that high-contrast spokes appear much more frequently on the morning half of the ring plane suggests that this creation process is also Sun locked but does not occur at the same longitude relative to the Sun as the SKR emission (Fig. 6). It is

Fig. 6. (a) The configuration of the center of the SKR-active sector (relative to the Sun) most likely for the appearance of high-contrast spokes on the morning half of the rings. (b) The configuration at which the most intense SKR emission occurs.

A.

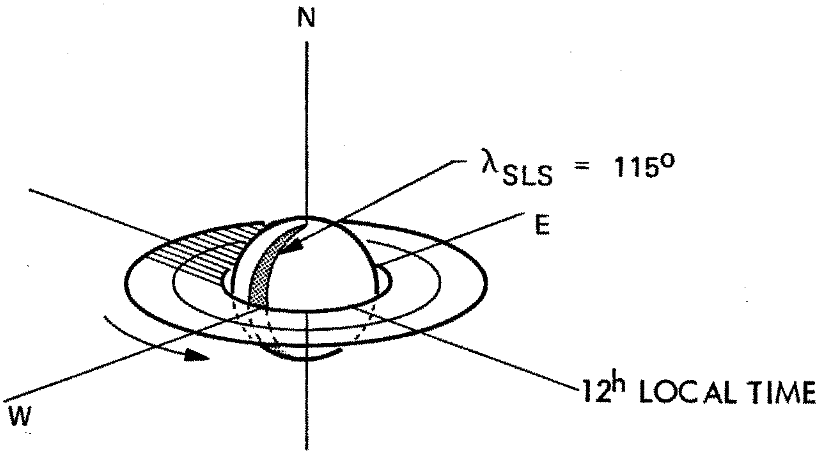
N
λ_{SLS} = 115°
E
W
12h LOCAL TIME

B.

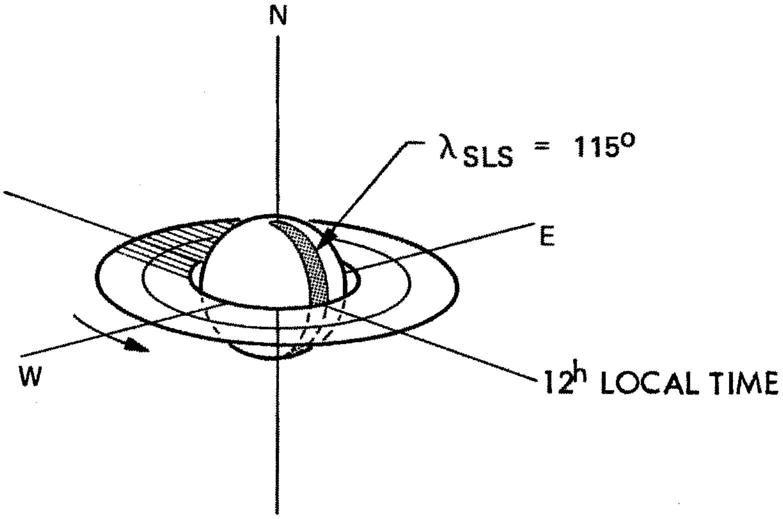
N
λ_{SLS} = 115°
E
W
12h LOCAL TIME

plausible, however, that the same inhomogeneity or feature in Saturn's near-surface field which is responsible for the occurrence of SKR (Kaiser *et al.* 1980) is also responsible at some later time for the initiation or enhancement of spoke activity. Passage of this SKR-active region through Saturn's shadow, for example, may play a significant role in either creating new spokes or straightening and enhancing old ones. It will be interesting to determine magnetic longitudes of the evening ansa for those rare frames on which high-contrast spokes are seen there; and to see if the appearance of spokes on the unilluminated side of Saturn's rings (Smith *et al.* 1982) occurs at a preferred longitude. It should be noted that the SKR southern hemisphere source is located at ~0° ± 60°, approximately 120° in longitude away from its northern-hemisphere counterpart.

A suggestion made by Smith *et al.* (1981) is relevant to this discussion: that the creation of spokes as discrete features is related in some way to the magnetic field, but the short-term motion of the individual particles which comprise a spoke is predominantly Keplerian. Over one rotation, Keplerian motion along the length of a typical spoke (~ 10,000 km) would result in a shear of ~ 50°. Angular velocity measurements on 11 spokes from six pairs of *Voyager 1* images taken only ~ 35 min apart (results are in preparation) show that, on the average, the short-term motions of spokes may depart slightly from pure Keplerian motion; but even these velocities, maintained for an entire rotation, would produce a shear close to 50°. No shear approaching this value has been observed anywhere on the rings in *Voyager 1* images. Therefore either the average motion of spoke particles over several hours or more can significantly depart from Keplerian motion, or the lifetime of a spoke as a discrete feature consisting of a given set of particles is less than one rotation. In observing spoke activity on the morning ansa over many rotations as was done here, one is witnessing in the latter case spoke features just recently formed, or in the former case, rejuvenated (i.e., straightened and enhanced) at the site of old ones by some process related to Saturn's field and possibly Saturn's shadow.

CONCLUSIONS

Analysis of *Voyager 1* images and preliminary analysis of *Voyager 2* images reveal a periodicity in the variation of spoke activity in Saturn's B ring. The evidence from a data set spanning ~586 rotations suggests that the fundamental period of this variation is that of Saturn's magnetic field, 639.4 min. A power spectrum computed using a data set spanning ~12 rotations yields a period of 621 ± 22 min, consistent with the magnetic period. Maximum spoke activity is most likely to occur within a range of magnetic longitudes containing the source region of the SKR. Passage of this region through Saturn's shadow may play a significant role in the creation and/or rejuvenation of spokes.

We gratefully acknowledge the helpful suggestions and advice of Dr. Peter Goldreich. Carol Stanley and John Freeman at JPL are thanked for their help in acquiring the supplementary data for the *Voyager* frames used in this work. David Diner at JPL and Michael Kaiser at Goddard Space Flight Center are thanked for private communications. In addition, we are indebted to Robert Deverill at Caltech for his invaluable computing assistance and Vance Haemmerle for the preparation of Fig. 1. This report presents the results of one phase of research carried out at CIT under contract with the *Voyager* Project at

JPL. This paper is Contribution No. 3725 of the Division of Geological and Planetary Sciences at Caltech.

REFERENCES

Deeming, T.J. (1975). *Astrophys. Space Sci.* **37**, 137.

Desch, M.D., and Kaiser, M.L. (1981). *Geophys. Res. Lett.* **8**, 253.

Evans, D.R. *et al.* (1981). *Nature* **292**, 716.

Kaiser, M.L., Desch, M.D., and Lecacheux, A. (1981). *Nature* **292**, 731.

Kaiser, M.L., and Desch, M.D. (1982). *Geophys. Res. Lett.* (in press).

Sandel, B.R., and Broadfoot, A.L. (1981). *Nature* **292**, 679.

Smith, B.A. *et al.* (1977). *Space Sci. Rev.* **21**, 103.

Smith, B.A. *et al.* (1981). *Science* **212**, 163.

Smith, B.A. *et al.* (1982). *Science* **215**, 504.

Warwick, J.W. *et al.* (1981). *Science* **212**, 239.

Chapter VI. Spoke Variability in Voyager 2 Images

1. Abstract

In this chapter, the analysis described in Chapter V is extended to include a Voyager 2 data set spanning ~ 90 Saturn rotations. The period of spoke activity variability is found from a Fourier analysis to be 640.6 ± 3.5 min, in excellent agreement with Saturn's inferred rotational period. Another feature in the power spectrum occurring at ~ 610 min is intriguingly close to the period of the Saturn Electrostatic Discharges (SED). The significance of these results is discussed. The correlations of maximum and minimum spoke activity with the SKR-active and SKR-inactive regions of the Saturn Longitude System (SLS) are confirmed. It has been determined that the occurrence of maximum evening-ansa spoke activity is also associated with the SKR-active sector.

2. Fourier Analysis

The data set used in this study consists of Voyager 2 narrow angle frames taken through the clear filter between days 174 and 213 of 1981. The resolution of these frames ranges from 551 to 232 km/pixel; the sub-s/c latitude and phase angle are ~ 10° and ~ 7°, respectively. Spokes appear as dark features against the rings. The frames were categorized according to an index referred to as 'spoke activity', a (subjective) measure of the product of the areal coverage and contrast of the spokes. The analysis of the Voyager 2 data string presented here was different from that described in Chapter V in only one regard: the frames were binned into 8 half-categories (0.5, 1.0, ... 3.5, 4.0) instead of 4 full categories (1.0, . ,4.0) for the purposes of decreasing quantization noise. The uncertainty in the assignment of a frame to a spoke activity category was estimated by performing the categorization procedure several times on 200 frames and computing the standard deviation around the mean category for each frame. The value of the deviation determined in this way was 0.68, where 1.0 = one full category.

Table 1 lists the Voyager 2 frames used for this analysis according to spoke activity category (column 1). Column 2 is the FDS (Flight Data Subsystem) number of the frame where 1.0 equals 48 minutes, and 0.01 equals 48 seconds.

In some cases, a frame was placed in a category for spoke activity that was not exactly centered on the ansa of the rings. This is particularly true for the high activity categories in which frames with a highly active spoke region centered exactly on the ansa are relatively rare. For these frames, the approximate angular displacement in degrees of the spoke active region from the ansa is listed in column 3. In the Fourier analysis, the FDS #'s of these frames were altered to the FDS #'s at which the off-centered region would (or did) appear on the ansa. The rotation rate used to make this adjustment was taken to be 850°/day, typical of the Keplerian angular velocities of the spoke region of the rings. The largest angular displacement for the morning-ansa data set was 35°, or 60 minutes of time. From examination of the frames comprising the Voyager 1 inbound movie of the rings, it is apparent that the evolution in contrast and areal coverage of the spokes in frames at this resolution is negligible over this time interval. Therefore, the error introduced in categorizing spoke activity within 60 minutes of the exact ansa-crossing time is insignificant. The typical time interval between these frames was ~ 3 hours; the entire length of the Voyager 2 data string was ~ 90 Saturn rotations. A Fourier power spectrum was computed using a technique appropriate for unequally spaced data. Once the period of the major peak in the spectrum was determined, this value was used as a first-guess input parameter to a non-linear least squares routine that fitted a sinusoid (of fixed amplitude and varying phase and period) to the data string.

Figure 1 is the Fourier power spectrum of the Voyager 2 data set computed over a range of periods corresponding to the approximate length of the data string (40,000 min) and to twice the typical sampling period (360 min). The most outstanding peak occurs at ~640 min. The value of this peak, determined from the non-linear least squares routine, is 640.6 min; the uncertainty we assign to this number is the half-width at half-maximum, ±3.5 min. The value obtained from a Voyager 1 imaging data set spanning ~12 Saturn rotations was 622 ± 21 min (chapter V). The longer Voyager 2 data set has yielded a more precise determination of this period.

3. Correlation of Activity with the Magnetic Field

The correlation of spoke activity with specific sectors of the SLS (reported in Chapter V) was found by computing the SLS longitude of the spoke active region in each frame at the time the frame was acquired and binning those frames of greatest and least activity according to SLS longitude. The same procedure was followed here. The entire morning-ansa sample consists of 408 frames which include the Voyager 2 data set (364 frames) listed in Table 1 and the Voyager 1 data set (44 frames) described in Chapter V. The lowest two half-categories (0.5 and 1.0) of the Voyager 2 data set were grouped together with Voyager 1 category 1 frames into the lowest activity group: the highest two (3.5 and 4.0) were grouped with Voyager 1 category 4 frames into the highest activity group. The total number of frames falling into these groups was 76 and 68,

Fig. 1. Fourier power spectrum of spoke activity observed on the morning ansa of the rings between days 174 and 213 of 1981. The second highest peak occurs at a period of ~ 610 min.

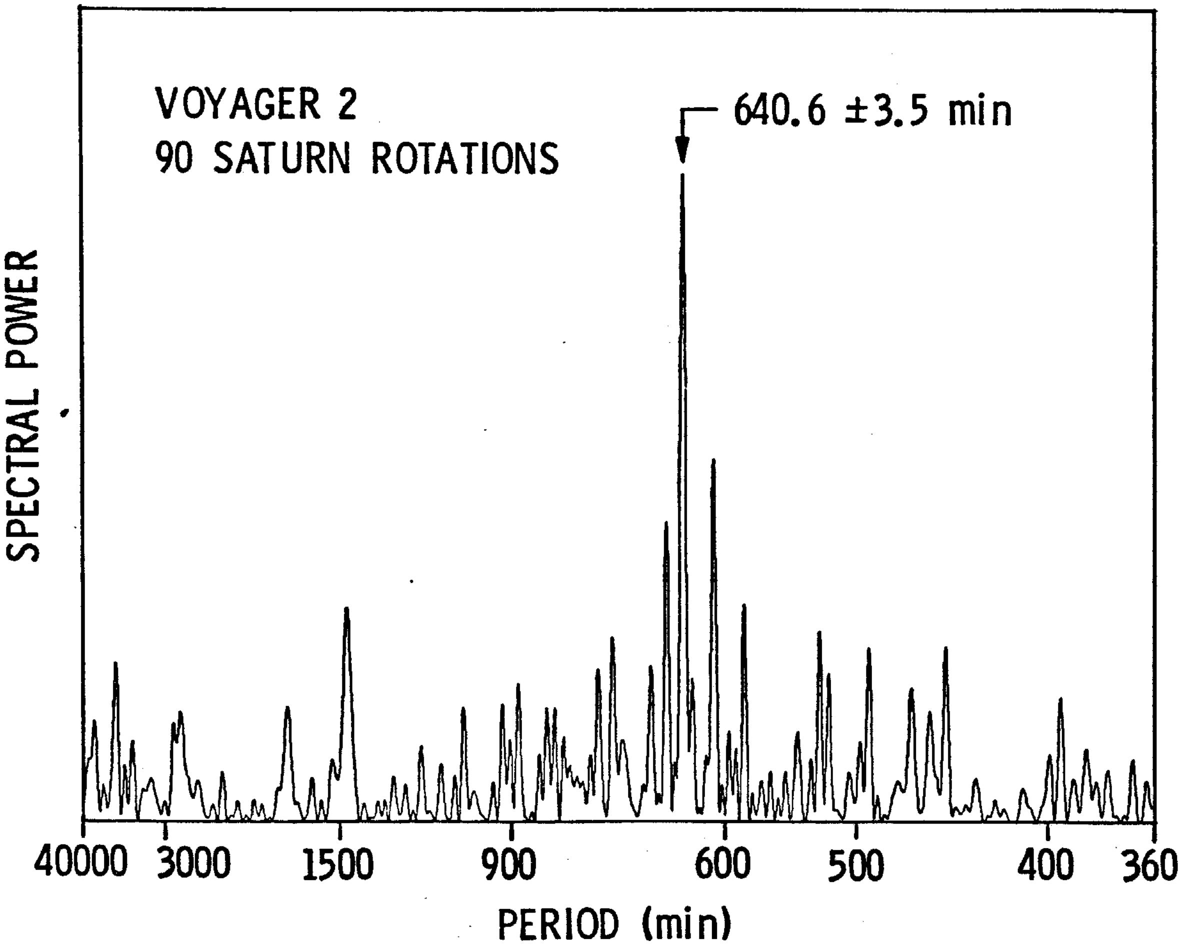
VOYAGER 2
90 SATURN ROTATIONS
640.6 ±3.5 min
SPECTRAL POWER
40000
3000
1500
900
600
500
400
360
PERIOD (min)

respectively. Their sum represents 35% of the entire morning ansa sample of 408.

Figure 2 shows the resulting histograms, equivalent to Fig. 4 of Chapter V. Though the spoke activity distribution in Fig. 2a is somewhat broader than Fig. 4 in Chapter V, the correlations of greatest activity with the SKR-active sector and least activity with the SKR-inactive sector are confirmed. The likelihood of obtaining either distribution from an equivalent-sized random sample in which no correlation exists is < 0.5%.

The same Voyager 2 data set examined for variation in morning-ansa spoke activity was examined for the presence of spokes on the evening side of the rings. In many of the frames taken from a range of 32.1×10^6 km or less, the evening ansa was not imaged. For this reason, those frames with FDS # greater than 43000.00 were rejected: the total evening ansa sample consists of 322 frames and includes no Voyager 1 frames.

In general, evening-ansa activity at its maximum is moderate compared with that on the morning side of the rings: in only a handful of frames does it equal the greatest morning ansa activity. The evening-ansa sample was divided in two groups only: those frames which exhibited high evening-ansa activity and those for which activity was feeble or non-existent. For the former group, the angular displacement of the spoke active region from the exact ansa location was noted and is listed in column 4. Thus, the frames with FDS # < 43000.00 comprise the evening ansa sample: those with entries in column 4 are the frames falling into the maximum evening-ansa activity category.

Figure 3 is the histogram, equivalent to Fig. 2, for evening-ansa activity. It is apparent that maximum evening-ansa activity is also correlated with the

Fig. 2. Frequency distributions showing the number of frames in the categories of A) greatest and B) least morning-ansa spoke activity which fall into the SLS longitude bins given on the abscissa. The center of the SKR source region is indicated along with the 100 kHz SKR occurrence rates.

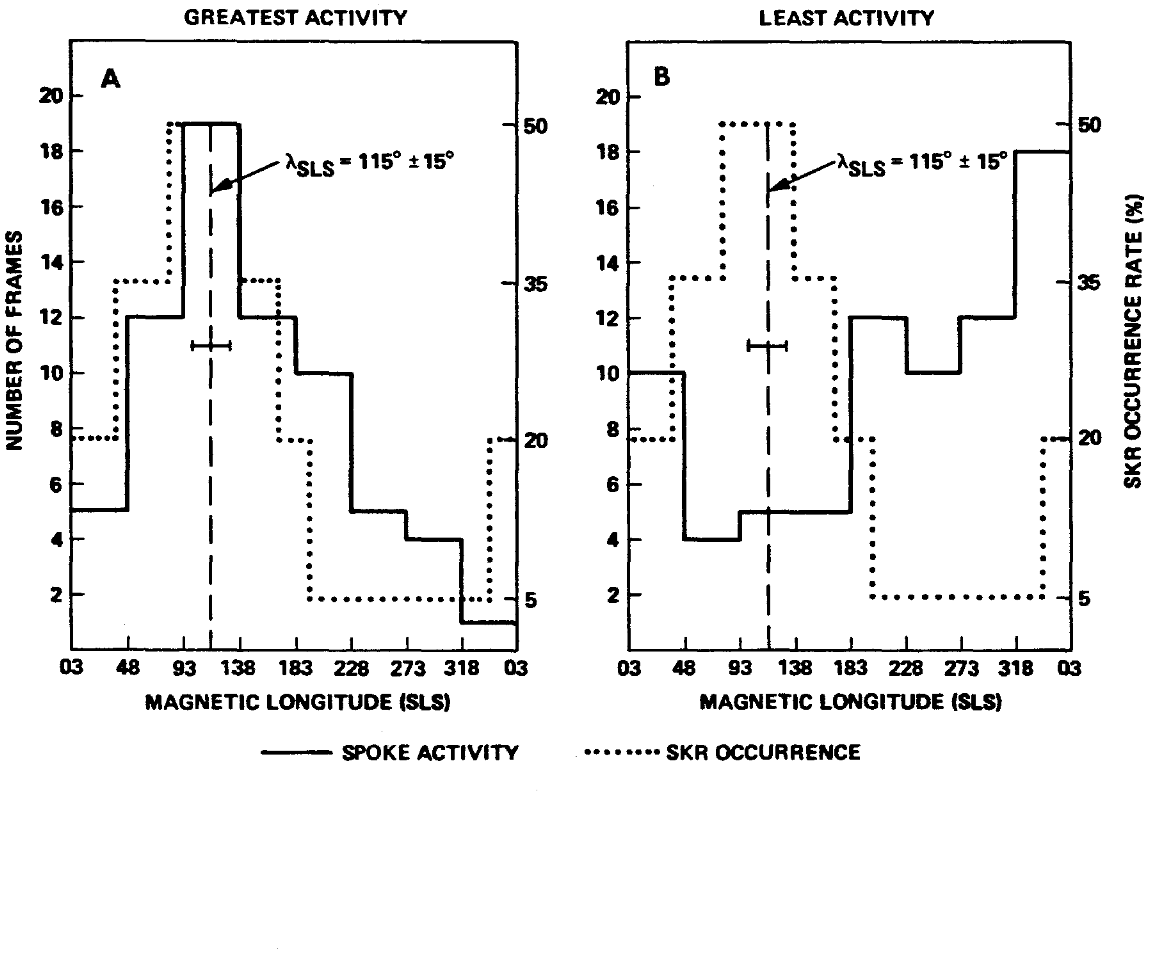
GREATEST ACTIVITY
LEAST ACTIVITY
A
B
λSLS = 115° ± 15°
λSLS = 115° ± 15°
NUMBER OF FRAMES
SKR OCCURRENCE RATE (%)
2
4
6
8
10
12
14
16
18
20
5
20
35
50
03
48
93
138
183
228
273
318
03
MAGNETIC LONGITUDE (SLS)
MAGNETIC LONGITUDE (SLS)
SPOKE ACTIVITY
SKR OCCURRENCE

Fig. 3. Frequency distribution of the number of frames exhibiting high evening-ansa spoke activity versus SLS longitude. Distribution of SKR occurrence rates is indicated.

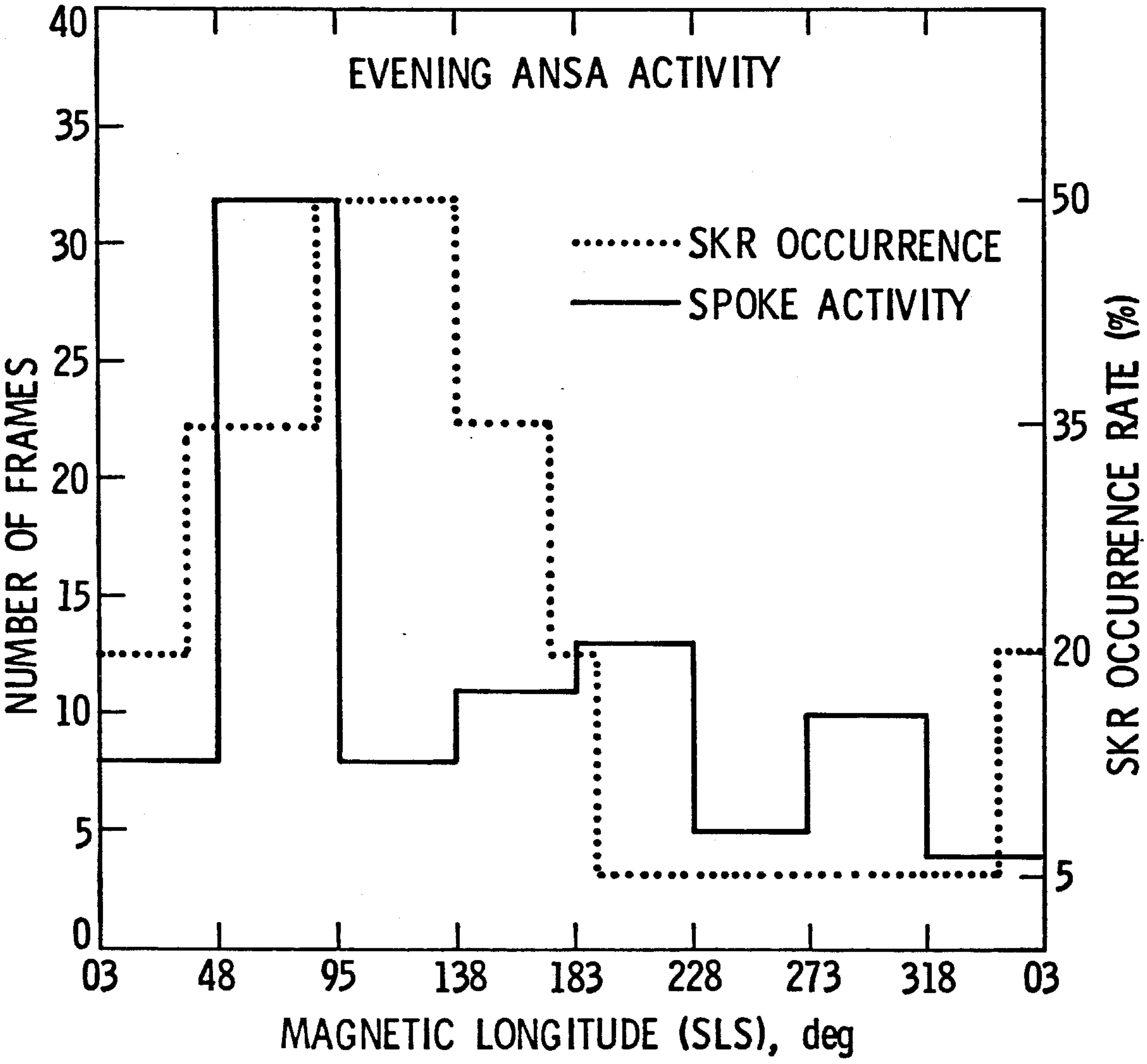
EVENING ANSA ACTIVITY
SKR OCCURRENCE
SPOKE ACTIVITY
NUMBER OF FRAMES
0
5
10
15
20
25
30
35
40
SKR OCCURRENCE RATE (%)
5
20
35
50
03
48
95
138
183
228
273
318
03
MAGNETIC LONGITUDE (SLS), deg

SKR-active sector. The distribution over magnetic longitude of the entire evening ansa data set is flat.

4. Discussion

The magnetic dipole field lines passing through the spoke region in the rings intersect the planet's surface at northern magnetic (planetocentric) latitudes of ~39°-45° and planetographic latitudes of ~45°-51°. [The latter range is computed using a dynamical oblateness for Saturn $\varepsilon = 0.096$ (Stevenson 1982)]. The atmospheric motions at these latitudes are ~7020-7080 m/sec (A. Ingersoll, private communication). Presumably, dynamic friction causes the lower ionosphere to move with these speeds as well. The corresponding range in rotation periods of these motions is ~632-626 min, well outside the period of spoke variability quoted here, 640.6 ± 3.5 min. On the basis of this comparison, we can exclude electrical storms in the lower Saturnian ionosphere as a cause of the periodic variation in spoke appearance.

The modulation period of the SKR, inferred to be the rotation period of Saturn's magnetic field, is 639.4 min (±3 sec) and is identical (within the uncertainties) to the spoke variability period derived here. The primary modulation in the appearance of spokes is undoubtedly due to the magnetic field. Moreover, the greatest spoke activity anywhere on the ring plane is likely to be associated with the SKR-active sector. The latter observation joins a growing body of evidence, including observations of auroral brightenings (Sandel and Broadfoot 1981) and charged particle periodicities (Carbary and Krimigis 1982), which indicates the existence of a large-scale anomaly in Saturn's field. The Voyager 1 and 2 magnetometer data showed no evidence of asymmetry in the low order — dipole, quadrupole, octupole — terms in the spherical harmonic expansion of Saturn's magnetic field (Connerney et al. 1982). These results imply that if an anomaly exists in the SKR-active hemisphere, it must be a near-surface feature extending from the auroral regions at ~ 80°N to the 'spoke' latitudes at ~ 40°N.

It is interesting to note that the apparent relationship of spoke activity to the sun indicates that the periodicity is a synodic rather than a sidereal one. This is also true for the period assigned to the magnetic field rotation since the emission of the SKR is also a Sun-locked phenomenon. However, the magnitude of the difference between the sidereal day and the mean solar day on Saturn is small. Saturn's mean motion around the Sun is 0.033°/day which amounts to a change in a 10 hour period of ~ 0.03 min or 1.6 sec. This difference is not detectable in either the SKR or the spoke variabilities for which the uncertainties are ± 3 sec and ± 4 min, respectively.

Of interest in the power spectrum shown in Fig. 1 is a peak at ~ 610 minutes. The period of the SED, the impulsive broadband (20 kHz-40 MHz) emissions discovered by Voyager, is 611 ± 5 min (Evans et al. 1981). The near coincidence of these numbers is intriguing as a relationship between spokes and SED has long been suspected.

Energy considerations in this regard are illuminating. The power density estimated in the SED bursts is 10 watts/Hz: peak values are an order of magnitude greater (Evans et al. 1983). From Voyager data it is apparent that the bandwidth is at least as wide as the bandwidth of the PRA receivers: 40 MHz. Assuming a 100 MHz bandwidth yields a total power of 10^{16} erg/sec.

The minimum power required to lift spoke particles can be estimated from their physical characteristics. Assuming ice particles of radius $r = 0.5\ \mu$, a spoke area $A = 10^9$ cm × 10^8 cm = 10^{17} cm^2, and an optical depth $\tau = 0.1$, one can compute the mass in a spoke to be $M = A\tau r\rho \approx 10^{12}$ gm. For a particle scale height, h, the kinetic energy $\approx M(\Omega h)^2 \approx 10^4$ h^2 erg. Examination of the Voyager 1 inbound and outbound movies reveals that there are ~50 major spokes produced per 10 hour interval. For h = 80 km, the power in the spokes $P \approx 10^{15}$ ergs/sec. A more realistic scale height, $h = 10^4$ cm, yields $P \approx 10^9$ ergs/sec, much less that that generated by the emission of the SED. It appears that a relationship between SED and spokes is not energetically implausible.

No consensus has been reached on the origin of the SED. The SED are observed at frequencies below the expected dayside ionospheric cut-off frequency of ~1 MHz. Warwick et al. (1981) rejected the possibility of an atmospheric source on the basis of this observation and instead suggested a source orbiting in the ring plane where the Keplerian orbital periods are ~610 min. Burns et al. (1983) have argued that the large ring shadow on the equatorial region of the planet, where the zonal wind periods are 610 min, could reduce the electron density in this region enough to permit the escape of low frequency radio noise. Kaiser et al. (1983) have re-analyzed the SED data, giving particular attention to the spacecraft-Saturn geometry, and find that the frequency-dependence and occurrence pattern of the SED can be explained by an equatorial storm system in the ring shadow extending ~60° in longitude but having a limited latitudinal extent, ~1°. The latter interpretation makes an SED-spoke relationship unlikely since the 'spoke' latitudes fall well above the equatorial region of the planet.

An indication of a periodicity in spoke activity equal to that of the SED could provide an important clue to the origin of both SED and spokes. Further analysis is required to determine whether the peak in the spoke activity power spectrum at 610 min is significant and whether it, indeed, represents a relationship between the two phenomena.

The result that evening-ansa activity is also associated with the SKR-active sector has important implications for the origin and evolution of spokes. It is true that the relative magnitude of the activity is diminished on the evening ansa: i.e., areal coverage and (most notably) contrast are decreased. It is reasonable to conclude, therefore, that the spoke activity observed on the evening side is that which formed as maximum morning-ansa activity and evolved through one-half an orbit to appear visible but less contrasty on the evening side. There appear to be no processes operating between the morning and evening sides (e.g., passage of the SKR-active sector through the Sun-Saturn plane and the most intense emission of SKR) which intensify the evening activity as the passage of this sector through the shadow intensifies the morning activity. The fact that the variation in spoke activity includes variability in areal coverage as well as contrast allows one to argue for enhanced probability of spoke creation in the SKR-active sector: i.e., the creation of new features as well as the contrast enhancement of old ones. Grun et al. (1983) have found results consistent with this hypothesis. These arguments lead to the suggestion that the origin of the spokes is intimately connected to the magnetic field and cannot be attributed to external processes such as meteorite impact as proposed by Goertz and Morfill (1983).

5. Conclusions

1. The period of the variability in spoke activity, derived from an analysis of Voyager 2 images spanning ~ 90 Saturn rotations, is 640.6 ± 3.5 min. This strongly suggests modulation of

spoke activity by the rotation of Saturn's magnetic field.

2. The correlation of maximum spoke activity with the SKR-active sector of the SLS is confirmed. This observation strengthens the likelihood of a near-field anomaly in the northern hemisphere of Saturn's field.
3. The greatest spoke activity observed on the evening ansa is also correlated with the SKR-active field sector.

TABLE 1

SPOKE CATEGORY	FDS #	ANGLE	EVENING ANSA ACTIVITY
0.5	42087.34		-45
0.5	42100.53		
0.5	42114.04		
0.5	42132.41		
0.5	42182.58		
0.5	42275.43		
0.5	42281.05		
0.5	42315.32		
0.5	42437.22		-45
0.5	42466.35		-30
0.5	42479.46		
0.5	42493.05		
0.5	42511.34		
0.5	42522.14		
0.5	42530.07		
0.5	42554.02		
0.5	42612.20	-10	
0.5	42702.26		0
0.5	42707.40		0
0.5	42750.04		
0.5	42840.10		
0.5	42858.43		
0.5	42948.49		
0.5	42975.08		
0.5	43025.29	-35	
0.5	43115.35		
0.5	43155.20		
0.5	43213.38		
0.5	43263.51	+15	
0.5	43269.46		
1.0	42108.46		
1.0	42122.01		
1.0	42159.11		-55
1.0	42198.52		
1.0	42251.56		
1.0	42254.35		-50
1.0	42265.07		
1.0	42307.35		
1.0	42318.07		-50
1.0	42331.22		
1.0	42365.49		
1.0	42506.16		+05
1.0	42516.56		-40
1.0	42559.16		
1.0	42580.32		
1.0	42583.11		-45
1.0	42599.01		

SPOKE CATEGORY	FDS #	ANGLE	EVENING ANSA ACTIVITY
1.0	42604.19	+20	
1.0	42607.02		
1.0	42670.38		
1.0	42673.17	+15	
1.0	42731.35		0 TO -55
1.0	42734.14		-50
1.0	42887.52		
1.0	42898.28		
1.0	42906.14		
1.0	42927.37		
1.0	42938.17		
1.0	43060.11		
1.0	43091.59		
1.0	43126.22	+35	
1.0	43266.13		
1.0	43277.43		
1.5	42084.55		0
1.5	42092.52		
1.5	42111.25		
1.5	42127.19		
1.5	42161.50		-30
1.5	42167.08		
1.5	42212.07	+10	
1.5	42225.26		
1.5	42238.37		-55
1.5	42259.49		-45
1.5	42299.34		
1.5	42326.04		-20
1.5	42339.23		0
1.5	42347.20		
1.5	42373.50		+20
1.5	42394.58	+10	
1.5	42397.41		
1.5	42424.07		+40
1.5	42426.50		
1.5	42429.29	-10	-35 TO -55
1.5	42447.58		
1.5	42450.37		-50
1.5	42487.47		0
1.5	42490.26		0 TO -50
1.5	42500.58		
1.5	42508.55		
1.5	42514.13		
1.5	42524.53		
1.5	42567.13		
1.5	42569.52	-10	0 TO -50
1.5	42572.31		
1.5	42585.50		
1.5	42593.43		
1.5	42596.22		-55

SPOKE CATEGORY	FDS #	ANGLE	EVENING ANSA ACTIVITY
1.5	42622.52		
1.5	42625.31		
1.5	42636.11		
1.5	42641.29		
1.5	42644.08		
1.5	42652.01		
1.5	42675.56		-50
1.5	42694.25		-45
1.5	42705.05		
1.5	42715.37		+10
1.5	42718.16		0 TO -45
1.5	42720.55		
1.5	42728.56		0
1.5	42766.02		
1.5	42771.16		
1.5	42792.32	+20	
1.5	42819.02		
1.5	42821.41		
1.5	42824.20		-15
1.5	42829.34		
1.5	42917.01		
1.5	42972.44		-55
1.5	42980.37		
1.5	43094.23		
1.5	43187.19		
1.5	43263.07		
1.5	43279.54		-58
2.0	42103.32	+10	
2.0	42130.08		
2.0	42135.20		
2.0	42145.52		
2.0	42164.29		-58
2.0	42172.22		
2.0	42185.37		
2.0	42196.17		
2.0	42220.08		
2.0	42243.55		
2.0	42249.17		+30 TO -25
2.0	42262.28		0
2.0	42267.46		-45
2.0	42286.23		-45
2.0	42294.16		
2.0	42344.41		-50
2.0	42352.34		-30
2.0	42357.52		-40
2.0	42379.04		
2.0	42400.20		
2.0	42402.59		
2.0	42405.38		
2.0	42410.52		-30 TO -55

SPOKE CATEGORY	FDS #	ANGLE	EVENING ANSA ACTIVITY
2.0	42418.49		
2.0	42432.08		
2.0	42440.01		
2.0	42442.40		
2.0	42445.19		
2.0	42461.17		
2.0	42482.25		
2.0	42519.35		
2.0	42527.28		0
2.0	42540.43		+35
2.0	42543.22		+10
2.0	42548.44		
2.0	42577.53		
2.0	42633.28	+25	
2.0	42646.43		
2.0	42657.19		
2.0	42736.49		
2.0	42747.25		
2.0	42758.05		
2.0	42800.25		
2.0	42803.04		
2.0	42811.01		
2.0	42813.40		
2.0	42832.13		
2.0	42850.50		-10 TO -58
2.0	42853.29		
2.0	42864.01		
2.0	42866.40		
2.0	42909.08		
2.0	42932.55		
2.0	42940.56		
2.0	42956.46		
2.0	42959.25		-35
2.0	42967.11		
2.0	42985.55		
2.0	42988.34		-35 TO -45
2.0	42993.52		
2.0	43004.17		
2.0	43007.07		
2.0	43038.55		
2.0	43176.32	-20	
2.0	43267.07		
2.5	42090.13	+30	
2.5	42095.31		
2.5	42151.10	+20	
2.5	42153.49		-30
2.5	42169.43		
2.5	42193.38		
2.5	42206.49		
2.5	42235.58		-20

SPOKE CATEGORY	FDS #	ANGLE	EVENING ANSA ACTIVITY
2.5	42273.04		-40
2.5	42278.26		
2.5	42283.44		
2.5	42288.58		0
2.5	42291.37		
2.5	42296.55		
2.5	42302.13		
2.5	42320.46		
2.5	42334.01		
2.5	42360.31		+25
2.5	42363.10		
2.5	42368.32		
2.5	42371.11		-55
2.5	42381.43		+30 TO +40
2.5	42389.40		-45
2.5	42392.19	+20	
2.5	42453.16		
2.5	42456.00		
2.5	42495.44		
2.5	42503.37	+20	-55
2.5	42532.46		
2.5	42551.23		-30
2.5	42614.59		
2.5	42638.50		
2.5	42659.58		
2.5	42662.37		0
2.5	42665.21		
2.5	42667.59		
2.5	42681.10		
2.5	42689.07		
2.5	42742.07		
2.5	42744.46		-45
2.5	42760.44		
2.5	42763.23		
2.5	42784.31		
2.5	42787.14		
2.5	42795.11	-25	
2.5	42816.23		-45
2.5	42842.49		
2.5	42845.28		
2.5	42871.58		-40
2.5	42895.49		
2.5	42930.16		
2.5	42935.23		
2.5	42946.10		
2.5	42970.05		+10
2.5	42996.20	+20	
2.5	43001.53		
2.5	43028.23		
2.5	43057.17		
2.5	43062.50		0

SPOKE CATEGORY	FDS #	ANGLE	EVENING ANSA ACTIVITY
2.5	43189.58		
2.5	43261.23		
2.5	43274.36		
2.5	43276.49		
3.0	42106.11		
3.0	42116.43		
3.0	42119.22		
3.0	42124.40		
3.0	42143.13		
3.0	42175.01		0
3.0	42201.31		-50
3.0	42209.28		0 TO -30
3.0	42233.19		
3.0	42241.16	+25	
3.0	42304.52		
3.0	42336.45		
3.0	42355.13		
3.0	42384.22		-40
3.0	42387.01		+25
3.0	42413.31		0
3.0	42421.28		
3.0	42434.47	+20	
3.0	42463.56	-20	
3.0	42474.28		
3.0	42477.07		-35 TO -50
3.0	42498.19		
3.0	42538.04		
3.0	42564.34		0
3.0	42575.10		
3.0	42588.25		
3.0	42591.04		
3.0	42609.41	+20	-10
3.0	42617.34	+15	-40
3.0	42649.22		0
3.0	42699.47		
3.0	42712.58		
3.0	42723.34		-45
3.0	42726.17		
3.0	42755.27		0
3.0	42776.34		0
3.0	42779.13		
3.0	42781.52		-45
3.0	42789.53	+30	
3.0	42797.46	+20	-30
3.0	42834.52		
3.0	42847.56		
3.0	42869.19	+20	
3.0	42901.07		
3.0	42911.47		
3.0	42914.11		

SPOKE CATEGORY	FDS #	ANGLE	EVENING ANSA ACTIVITY
3.0	42991.13		
3.0	43020.22	-30	
3.0	43033.26		
3.0	43068.04		
3.0	43123.32		
3.0	43136.58	+25	
3.0	43184.29		
3.5	42137.59		
3.5	42177.40		
3.5	42188.20	+30	-25
3.5	42214.46		
3.5	42228.05		
3.5	42246.34	+20	
3.5	42257.14		
3.5	42312.53		-45
3.5	42323.25		
3.5	42328.43		+30
3.5	42342.02		
3.5	42376.29		
3.5	42408.13		
3.5	42416.10	+20	0 TO -40
3.5	42458.38		
3.5	42469.10	+30	
3.5	42471.49		
3.5	42485.04	+20	
3.5	42556.41	+30	-20
3.5	42601.40		-15
3.5	42620.13		
3.5	42628.10		
3.5	42630.49		
3.5	42654.40		-40
3.5	42683.49	+25	
3.5	42686.28		
3.5	42697.08	+20	
3.5	42710.19	+20	
3.5	42768.37	-20	
3.5	42773.55		
3.5	42805.43	-30	
3.5	42808.22	-25	
3.5	42837.31		-45
3.5	42855.53		
3.5	42943.20	+25	
3.5	43017.43		
3.5	43036.16		
3.5	43065.14	+15	
3.5	43086.26		
3.5	43147.23	+20	
3.5	43260.39		
3.5	43271.23		
3.5	43272.25	-20	

SPOKE CATEGORY	FDS #	ANGLE	EVENING ANSA ACTIVITY
4.0	42140.34	+30	
4.0	42156.28		
4.0	42180.19	+35	
4.0	42190.59		
4.0	42204.10		
4.0	42217.25		
4.0	42230.40		
4.0	42270.25		
4.0	42310.14		
4.0	42349.55		
4.0	42535.25		
4.0	42561.55		0
4.0	42739.28		
4.0	42977.58		
4.0	43152.44	-25	
4.0	43205.41		

TOTALS

Morning Activity:
0.5 - 30
1.0 - 33
1.5 - 61
2.0 - 65
2.5 - 63
3.0 - 53
3.5 - 43
4.0 - 16

Evening Activity:
Active - 91
Inactive - 231

REFERENCES

Burns, J.A., Showalter, M.R., Cuzzi, J.N., and Durisen, R.H. (1983). *Icarus* **54**.

Carbary, J.F. and Krimigis, S.M. (1982). *Geophys. Res. Lett.* **9**, 1073.

Connerney, J.E.P., Ness, N.F., and Acuna, M.H. (1982). *Nature* **298**, 5869.

Evans, D.R., Warwick, J.W., Pearce, J.B., Carr, T.D., and Schauble, J.J. (1981). *Nature* **292**, 716.

Evans, D.R., Romig, J.H., and Warwick, J.W. (1983). *Icarus*. In press.

Goertz, C.K. and Morfill, G. (1983). *Icarus* **53**, 219.

Grun, E., Morfill, G.E., Terrile, R.J., Johnson, T.V., and Schwehm, G. (1983). *Icarus*, submitted.

Kaiser, M.L., Connerney, J.E.P., and Desch, M.D. (1983). *Nature*, submitted.

Sandel, B.R. and Broadfoot, A.L. (1981). *Nature* **292**, 679.

Stevenson, D.J. (1982). *Ann. Rev. Earth Planet. Sci.* **10**, 257.

Warwick, J.W., et al. (1981). *Science* **212**, 239.

Plate 1. Four images of the Cassini division taken within 7 hours of each other. The middle two panels are taken from two images of the east ansa; the outer panels from the west ansa 180° away. Resolution is ~ 8 km/pixel. The Maxwell ringlet at 1.95 R_s is clearly visible in a gap whose width varies due to variations in the B ring edge. Note that the B ring edge has a spatial frequency of variation equal to twice that of the ringlet.

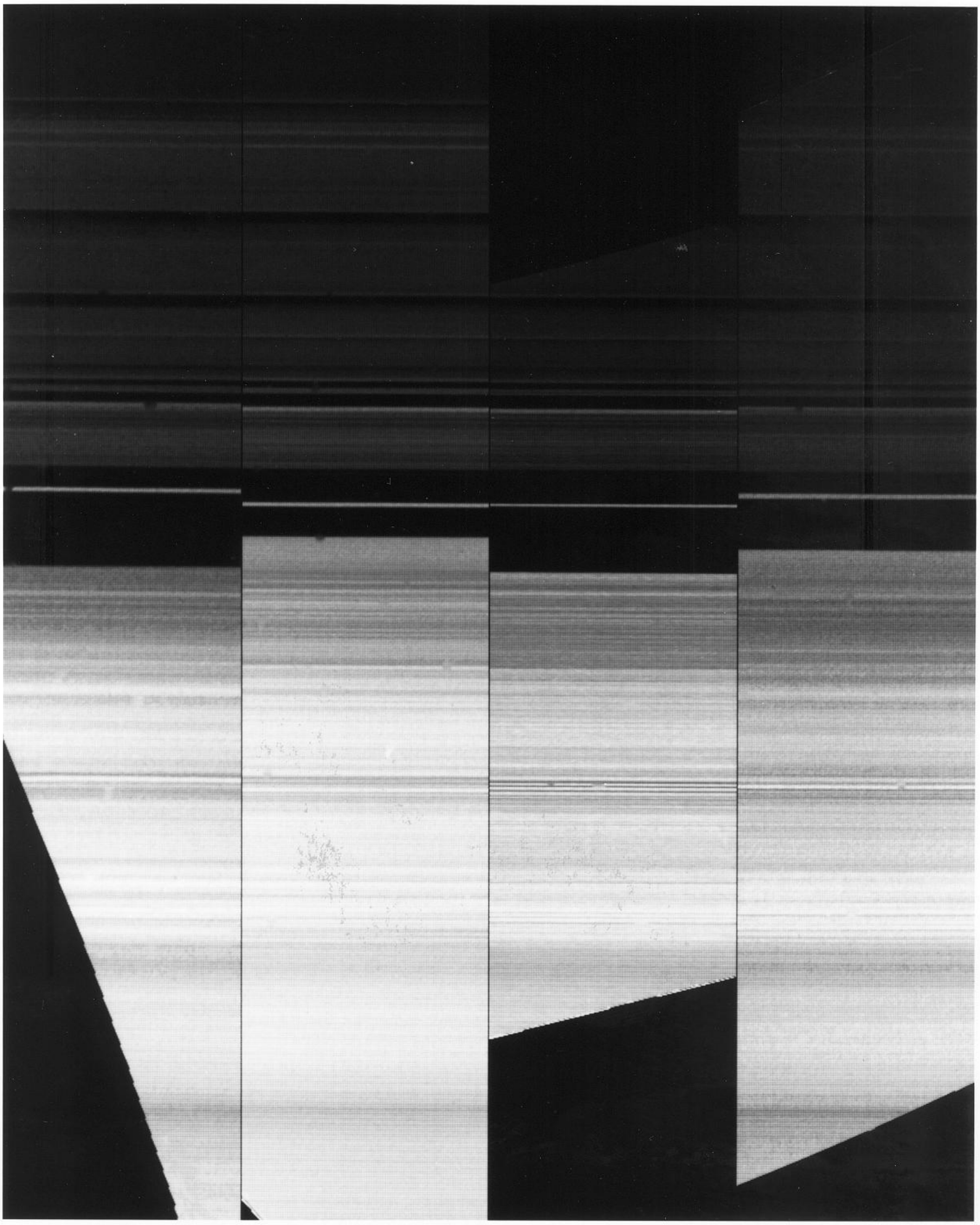

Plate 2. Two Voyager 1 images (~ 25 km/pixel) of opposite ansae of the rings joined to illustrate the eccentric Huygens ringlet at 1.45 R_s. The gap in which the ringlet sits, the Huygens gap, is ~ 268 km wide. Note that the ringlet's width increases with radial distance from the planet.

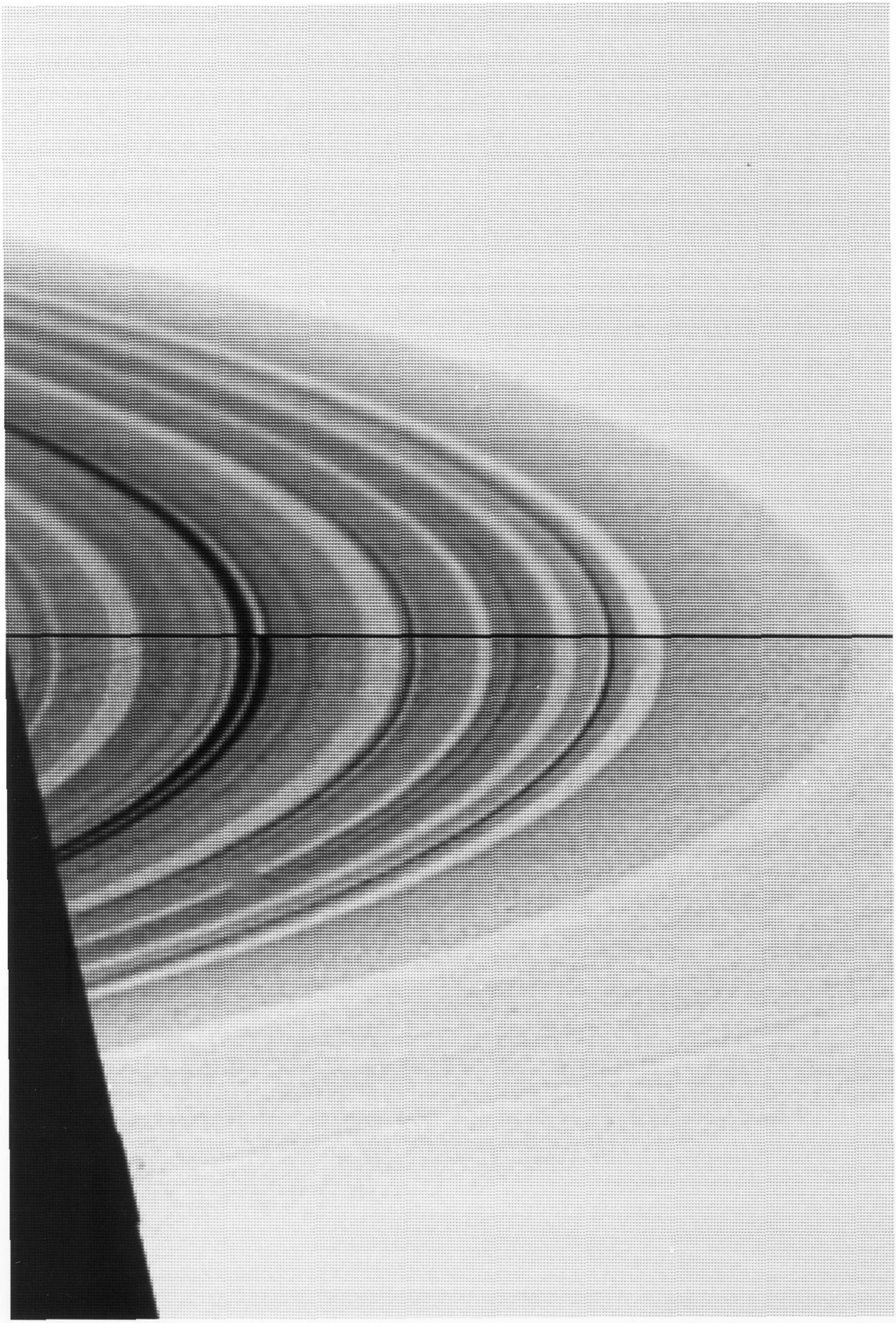

Plate 3. High resolution (~ 5 km/pixel) Voyager 2 image of the C ring in the vicinity of 1.29 R_s. The Titan ringlet is the bright narrow ringlet sitting in a dark gap in the upper right quarter of the photo. Note the Titan gap's sharp bright outer edge and faint inner edge. The ringlet here is ~ 21 km wide; the gap width is ~ 184 km.

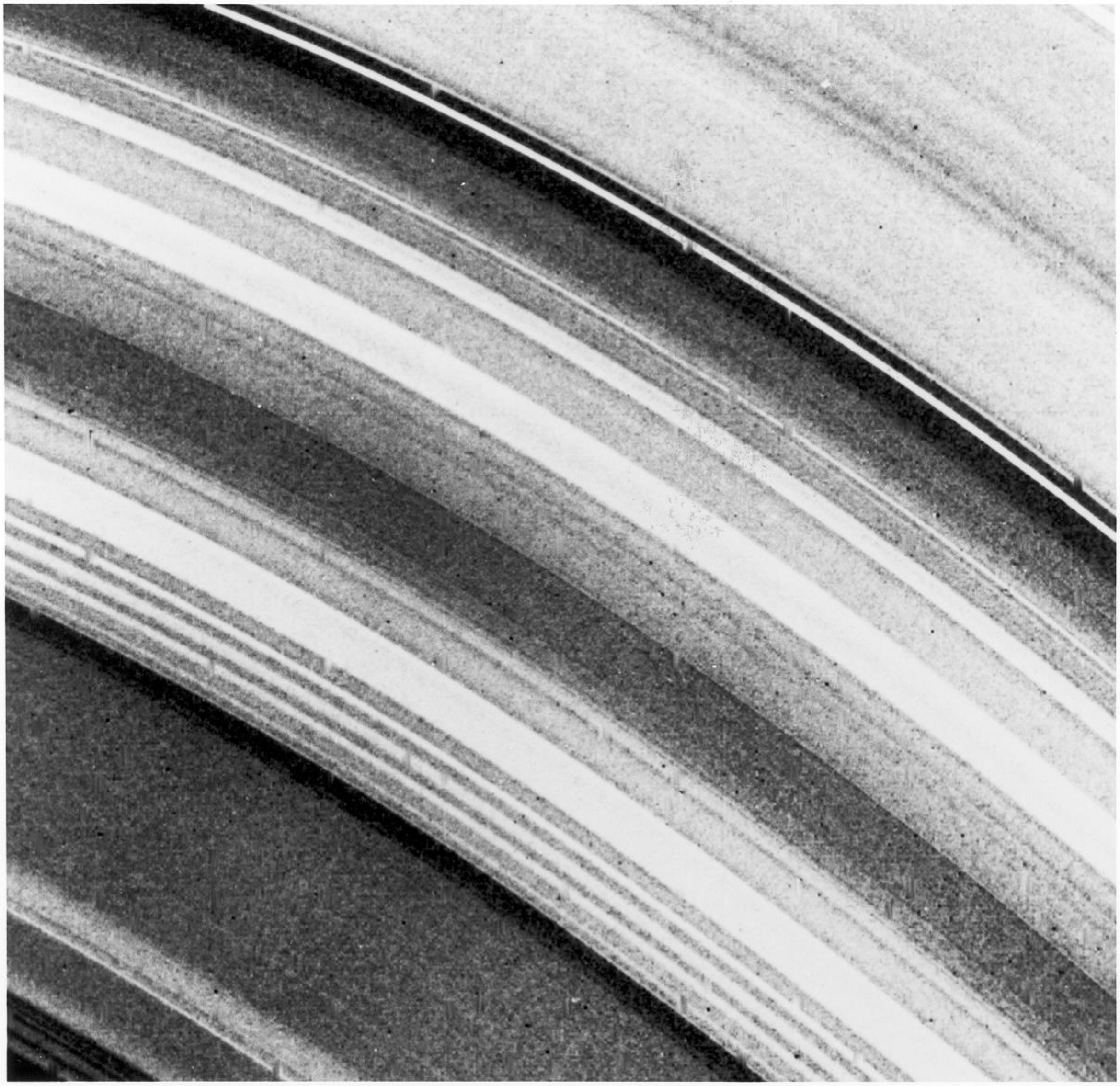

Plate 4. High resolution (60 km/pixel) Voyager image taken in forward-scattered light showing wispy sheared spokes in the outer-most B ring, typical wedge-shaped structure, and the random array of bright and dark narrow ringlets across which these features lie.

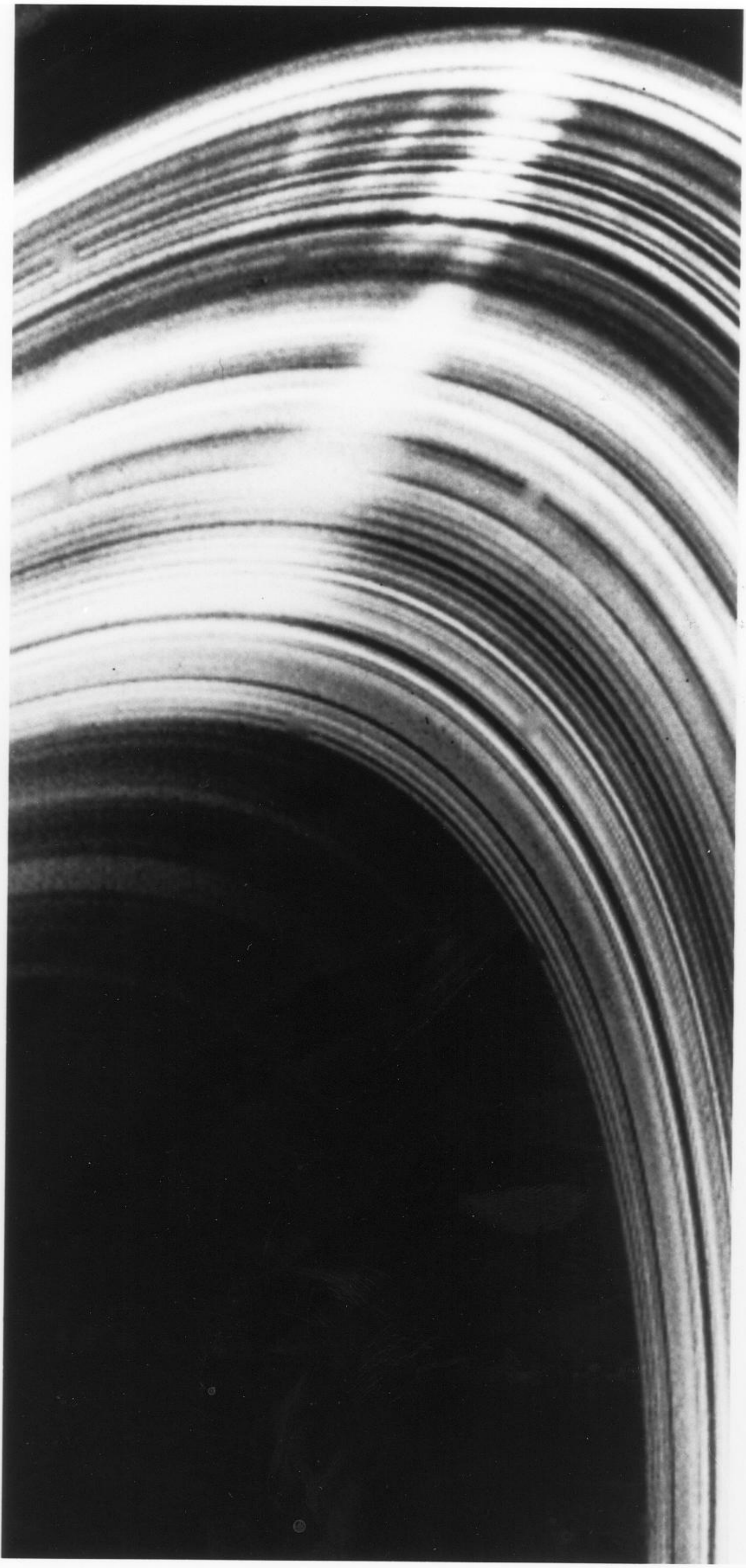

Not too bad for a girl from the Bronx, huh?